Institut für Flugzeugbau
der Universität Stuttgart

Masterarbeit

Experimental investigation of a PEMFC system operated under low pressure conditions

Bearbeiter

Jonas Settele

EXPERIMENTAL INVESTIGATION OF A PEMFC SYSTEM OPERATED UNDER LOW PRESSURE CONDITIONS

Master´s Thesis

by

Mr. Jonas Settele

carried out at

INSTITUTE OF AIRCRAFT DESIGN,

UNIVERSITY OF STUTTGART

and

INSTITUTE OF ENGINEERING THERMODYNAMICS,

GERMAN AEROSPACE CENTER, STUTTGART

Stuttgart, May 2023

University of Stuttgart
Germany

Institute of Aircraft Design

Head of Institute
Prof. Dr. Peter Middendorf
Prof. Dr. Po Wen Cheng
Prof. Dr. Andreas Strohmayer

University of Stuttgart
Institute of Aircraft Design • Pfaffenwaldring 31 • D-70569 Stuttgart

Contact
Pfaffenwaldring 31
D-70569 Stuttgart
T +49 (0)711 685-62402
F +49 (0)711 685-62449

Jonas Settele
Adlerstraße 56
70199 Stuttgart
Student No.: 3224113

Master´s Thesis

Title:

Experimental investigation of a PEMFC system operated under low pressure conditions

Brief description:

The behavior of a fuel cell system under high-altitude conditions is to be investigated in a low-pressure chamber. In the first step of a measurement campaign, polarization curves at different pressure levels are to be recorded using a standardized load profile. In this process, the polymer electrolyte membrane (PEM) fuel cell will be operated with control parameters optimized for ambient conditions at ground level.

Subsequently, individual parameters such as fuel cell operating temperature or cathode stoichiometry will be varied to investigate the effects on stack behavior. The aim is to interpret the influence of the parameters on e.g. the cell voltage, efficiency and humidification of the fuel cell based on thermodynamic relationships. The experimental results shall build the basis for a map of optimal operating conditions for the fuel cell system at various low-pressures levels. In the future the resulting map will be used to derive an optimized control strategy to reduce power losses at high-altitude.

Work items:

- Familiarization with the subject
- Identification of relevant experimental parameters and conceptual design of a parameter study
- Experimental investigation
- Evaluation and interpretation of the measurement results
- Preparation of a final thesis

Thesis issued on: **15/11/2022**

Thesis submitted on: 31.05.2023

Tutor: Jonas Lay (IFB)
Dr. techn. Dominik Murschenhofer (DLR)

Stuttgart, 25/10/2022

Prof. Dr.-Ing. Andreas Strohmayer

Abstract

The development of powertrains for regional aircraft based on proton-exchange membrane fuel cells represents a promising approach to decarbonize the aviation sector. Nevertheless, fuel cell systems suffer from significant performance and efficiency losses due to the decreased ambient pressure prevailing at high altitudes. To minimize these losses, a Hydrogenics HyPM® HD 10-120 PEMFC system was experimentally investigated in a low-pressure chamber at the Institute of Engineering Thermodynamics of the German Aerospace Center, Stuttgart.

During the first experimental phase, polarization curves were obtained at different ambient pressures ranging from 1000 to 500 hPa using the standard control parameters recommended by the manufacturer, such as stack temperature and cathode stoichiometry. Based on the results, a parameter study was conducted in the second phase to identify the optimal operating parameters under altitude conditions through the application of a regression model. Within the framework of the parameter study, the pressure, stack current, stack temperature, and cathode stoichiometry were systematically varied to improve water management under low-pressure conditions. The D-optimal experimental design methodology was employed for this purpose. Finally, polarization curves were recorded using the determined optimal control parameters for comparison.

In the first phase, net power losses of 59.3 % were observed at 500 hPa compared to 1000 hPa when employing the standard control parameters. These losses were attributed to the reduced pressure at high altitudes and, amongst others, to the consequent membrane dehydration. Additionally, a higher overall parasitic power demand was determined, resulting from the reduced density combined with a constant air mass flow requirement.

The parameter study revealed that the stack temperature has a more significant influence on water management and, consequently, net power output than cathode stoichiometry. Furthermore, these effects are current-dependent, with deviations from optimal operating parameters at higher current densities resulting in greater power losses. The regression model derived from the parameter study enabled the identification of optimal operating parameters. A comparison of the polarization curves using the standard and optimized parameters for temperature and stoichiometry control exhibited a significant net power increase of 13.5 % at 500 hPa. Preliminary results obtained with manually optimized parameters at higher current densities indicated an even greater performance improvement of 28.8 %. This suggests further potential for optimization. Moreover, the comparison revealed that the relative humidity at the cathode outlet can be used as a pressure-independent control variable for maximizing the net power output.

Overall, the experimental investigation demonstrates considerable potential for optimizing the operation of PEM fuel cell systems in the aviation environment by stack temperature and cathode stoichiometry adaptation.

Kurzfassung

Die Entwicklung von Antrieben auf Basis von Polymer-Elektrolyt-Membran Brennstoffzellen für Regionalflugzeuge ist ein vielversprechender Ansatz zur Dekarbonisierung des Luftfahrtsektors. Durch den in der Höhe vorherrschenden verringerten Umgebungsdruck, leiden Brennstoffzellensysteme jedoch unter starken Leistungsverlusten. Um diese zu verringern, wurden am Institut für Technische Thermodynamik des Deutschen Zentrums für Luft- und Raumfahrt ein Hydrogenics HyPM® HD 10-120 PEM-Brennstoffzellen System experimentell in einer Unterdruckkammer untersucht.

In einer ersten experimentellen Phase wurden Polarisationskurven bei verschiedenen Umgebungsdrücken zwischen 1000 und 500 hPa mithilfe der vom Hersteller empfohlenen Standardregelparametern für z.B. Stacktemperatur und Kathodenstöchiometrie erfasst. Basierend auf den Ergebnissen wurde in einer zweiten Phase eine Parameterstudie durchgeführt, um die optimalen Betriebsparameter mit Hilfe eines Regressionsmodells unter Höhenbedingungen zu identifizieren. Im Rahmen der Parameterstudie wurden neben dem Druck, der Stackstrom sowie die Parameter Stacktemperatur und Kathodenstöchiometrie systematisch variiert, um insbesondere das Wassermanagement unter verringerten Umgebungsdrücken zu verbessern. Dafür wurde die D-optimale Versuchsplanung als Versuchsplanungsmethodik angewendet. Abschließen wurden Polarisationskurven mit den ermittelten optimalen Parameterkombinationen zum Vergleich aufgenommen.

In der ersten Phase, unter Verwendung der Standardparameter wurden Nettoleistungsverluste von 59.3 % bei 500 hPa im Vergleich zu 1000 hPa festgestellt. Diese Verluste waren unter anderem auf den verringerten Druck in großen Höhen und der daraus resultierenden Austrocknung der Membran zurückzuführen. Ebenfalls wurden insgesamt höhere parasitäre Leistungsverluste ermittelt, die aufgrund der geringeren Dichte in Verbindung mit einem konstanten Luftmassenstrombedarf auftreten.

Die Parameterstudie zeigte, dass die Stacktemperatur einen größeren Einfluss auf das Wassermanagement und somit auf die Nettoleistung hat als die Kathodenstöchiometrie. Zudem sind diese Einflüsse stromabhängig, wobei Abweichungen von den optimalen Betriebsparametern bei höherem Strom mit größeren Leistungsverlusten einhergehen. Mit resultierenden Regressionsmodell konnten optimale Betriebsparameter identifiziert werden. Ein Vergleich der Polarisationskurven mit den standardmäßigen und optimierten Parametern für die Temperatur- und Stöchiometrieregelung zeigte eine signifikante Nettoleistungssteigerung von 13.5 % bei 500 hPa. Vorläufige Ergebnisse, die mit manuell optimierten Parametern bei höheren Stromdichten erzielt wurden, zeigten sogar eine Leistungssteigerung von 28.8 %. Dies gibt Hinweis auf weiteres Optimierungspotenzial. Zudem ergab der Vergleich, dass die relative Feuchte am Kathodenauslass als vom Druck unabhängig Regelgröße zur Maximierung der Nettoleistung verwendet werden kann.

Insgesamt zeigt die experimentelle Untersuchung ein beträchtliches Optimierungspotenzial für den Betrieb von PEM Brennstoffzellensystemen im Luftfahrtumfeld durch Anpassung der Stacktemperatur und der Kathodenstöchiometrie auf.

Danksagung

Die vorliegende Arbeit entstand während meiner Tätigkeit als Masterand beim Deutschen Zentrum für Luft- und Raumfahrt (DLR) am Standort Stuttgart in Kooperation mit dem Institut für Flugzeugbau (IFB) der Universität Stuttgart.

An dieser Stelle möchte ich mich bei all denjenigen bedanken, die mich während der Anfertigung dieser Masterarbeit unterstützt und motiviert haben.

Allem voran gebührt ein besonderer Dank meinem Betreuer am DLR, Dr. techn. Dominik Murschenhofer. Für deine fachliche Expertise, deine Unterstützung während des gesamten Prozesses und für deine konstruktive Kritik bin ich dir sehr dankbar. Du hast mir viel beigebracht, sodass ich besonders beim wissenschaftlichen Arbeiten große Fortschritte erzielen konnte.

Ebenfalls möchte ich mich bei Andreas Bender für den wertvollen Austausch und die Betreuung seitens des IFBs bedanken.

Mein weiterer Dank gilt Herrn Prof. Dr.-Ing. Andreas Strohmayer als Prüfer und geschätzter Dozent im Bereich Flugzeugentwurf an der Universität Stuttgart.

Auch meinen Kolleginnen und Kollegen beim DLR gebührt ein großer Dank für die tolle Zusammenarbeit. Durch eure Unterstützung im Labor und eure Anregungen, sowie Ideen bzgl. meiner Arbeit habt ihr mir sehr geholfen. Es war eine inspirierende Umgebung, in der ich mich auch fortan gerne weiterentwickeln werde.

Weiterhin möchte ich mich bei meiner Freundin Vera Gauggel und meinem ehemaligen Kommilitonen Christopher Homm für das Korrekturlesen bedanken.

Zu guter Letzt möchte ich meinen Eltern von Herzen danken. Ihr habt mir das Studium ermöglicht und mich stets gefördert. Eure bedingungslose Unterstützung hat mich motiviert, mein Bestes zu geben und diese Masterarbeit erfolgreich abzuschließen.

Stuttgart, im Mai 2023

Table of Contents

Nomenclature

List of Acronyms

ANOVA	Analysis of variance
ATLAS	Altitude test chamber for low-pressure analysis of FC systems
BoP	Balance-of-plant
BPP	Bipolar plate
CAN	Controller area network
CCD	Central composite design
CL	Catalyst layer
CSV	Comma-separated values
CORSIA	Carbon offsetting and reduction scheme for international aviation
DLR	Deutsches Zentrum für Luft- und Raumfahrt (German Aerospace Center)
DoE	Design of experiments
EU	European Union
FC	Fuel cell
FCTES^{QA}	Fuel cell testing, safety and quality assurance
GDL	Gas diffusion layer
HHV	Higher heating value
IAPWS	International Association for the Properties of Water and Steam
IATA	International Air Transport Association
ICAO	International Civil Aviation Organization
ISA	International standard atmosphere
LHV	Lower heating value
MEA	Membrane electrode assembly
MFC	Mass flow controller
MFM	Mass flow meter
MPL	Microporous layer
OCV	Open-circuit voltage
PDC	Power distribution controller
PEM	Proton-exchange membrane, polymer electrolyte membrane
PEMFC	Proton-exchange membrane fuel cell
P&ID	Piping and instrumentation diagram
RSM	Response surface methodology
SAF	Sustainable aviation fuel
SOFC	Solid oxide fuel cell

List of Symbols

Greek symbols

Symbol	Description	Unit
α	Charge-transfer coefficient	-
β	Regression model coefficient	-
Δ	Difference	-
ΔU_{act}	Activation loss	V
ΔU_{conc}	Concentration (mass-transport) loss	V
ΔU_{ohm}	Ohmic loss	V
η	Efficiency	-
η_{fuel}	Fuel utilization coefficient	-
η_{LHV}	Fuel cell efficiency related to the lower heating value	-
$\eta_{FC,LHV}$	Fuel cell gross efficiency related to the lower heating value	-
$\eta_{Net,LHV}$	System efficiency related to the lower heating value	-

λ_a	Anode stoichiometry	-
λ_c	Cathode stoichiometry	-
ρ_{air}	Density of air	kg/m^3
ρ_{O_2}	Density of oxygen	kg/m^3

Latin symbols

Symbol	Description	Unit
B	Empirical coefficient	V
B_{fit}	Fitting parameter for mass-transfere loss	V
E	Potential	V
E_0	Reversible cell voltage (or Nernst potential)	V
E_{fit}	Fitting parameter for the y-intercept	V
E_{OCV}	Open-circuit voltage	V
$E_{T,p}$	Equilibrium potential	V
G	Gibbs free energy	kJ/mol
H	Enthalpy	kJ/mol
i	Current density	A/cm^2
i_0	Exchange-current density	A/cm^2
i_L	Limiting current density	A/cm^2
$i_{L,fit}$	Fitting parameter for the limiting current density	A/cm^2
I	Current	A
I_{max}	Maximum stack current	A
k	Interval	-
$\dot{n}$	Consumption rate	mol/s
n_{cells}	Number of cells of the stack	-
n_f	Numbers of factors	-
n_l	Respective levels of factors	-
n_{total}	Total number of experiments	-
$\dot{m}_{act}$	Actual mass flow rate of a reactant at the cell inlet	kg/s
$\dot{m}_{cons}$	Consumption mass flow rate	kg/s
$\dot{m}_{H_2}$	Mass flow rate of hydrogen	kg/s
$\dot{m}_{H_2O}$	Mass flow rate of water	kg/s
$\dot{m}_{O_2}$	Mass flow rate of oxygen	kg/s
M_i	Molar mass of the corresponding substance i	kg/mol
p	Pressure	hPa
p_{avg}	Averaged pressure	hPa
p_{H_2}	Partial pressures for hydrogen	hPa
p_{H_2O}	Partial pressures for water	hPa
p_{O_2}	Partial pressures for oxygen	hPa
p_{out}	Pressure at the cathode outlet	hPa
P_{net}	Net power	W
p_{sat}	Saturation pressure	hPa
$r_{O_2,in}$	Oxygen concentration at the cathode inlet	Vol%
R^2	Coefficient of determination	-
rH_{out}	Calculated relative humidity values	-
R_i	Internal resistance	Ωcm^2
R_{fit}	Fitting parameter for the ohmic resistance	Ωcm^2
t_{acq}	Period of data acquisition	min
t_{dwell}	Dwell time	min
t_{stab}	Period of stabilization	min
t_{offs}	Offset time	s

T	Temperature	K
T_{out}	Temperature at the cathode outlet	K
S	Entropy	kJ/molK
U_{cell}	Cell voltage	V
$\dot{V}_{air}$	Volume flow rate of the air	slpm
W_{el}	Electrical work	J/mol
W_{H_2}	Chemical energy of hydrogen	J/mol
y	Response variable (net power)	W
z	Number of electrons per molecule	-

Constants

Symbol	Description	Value
ΔG_0	Gibbs free energy change (standard conditions)	-237.13 kJ/mol
ΔH_{LHV}	Lower heating value of hydrogen	241 kJ/mol
F	Faraday´s constant	96.485 As/mol
p_0	Standard pressure	1013.25 hPa
r_{O_2}	Oxygen concentration	0.2096
R	Molar gas constant	8.314 J/molK
T_0	standard temperature	298.15 K

Chemical symbols

Symbol	Description
e^-	Free electron
H^+	Positively charged hydrogen ion (or protons)
H_2	Molecular hydrogen
H_2O	Water
O_2	Molecular oxygen

List of Figures

List of Tables

1. Introduction

1.1. Motivation

The aviation industry is currently in an unprecedented race against time to reduce its impact on the climate while meeting the growing demand for air travel. In response to this urgent need, a majority of global civil aviation operations, including the International Air Transport Association (IATA), as well as aircraft manufacturers and suppliers such as Airbus, Boeing, and Rolls Royce, have committed to achieving carbon neutrality by 2050 through the declaration of 'Fly Net Zero 2050' [1]. The European Union (EU) has also legally committed to this goal as part of the Green Deal, including the intermediate target of at least a 55 % net reduction in greenhouse gas emissions compared to 1990 levels by 2030, known as 'Fit for 55' [2].

To achieve these goals, aviation industry players are not only relying on voluntary programs such as the Carbon Offsetting and Reduction Scheme for International Aviation (CORSIA) introduced by the International Civil Aviation Organization (ICAO) [3], but are also taking initial regulatory action. The Council of the EU and the European Parliament recently reached a provisional political agreement on the ReFuelEU Aviation initiative, which mandates a minimum share of sustainable aviation fuels (SAFs) to be used in flights starting from 2025 [4].

Meeting the demands of sustainable development presents a monumental challenge to the aviation industry. To accomplish this transformation successfully, it is not only necessary to improve existing technologies, but the industry must also focus on adopting radically new technologies in the long run. One of the most promising technologies is the use of green hydrogen, particularly in liquid form, as an in-flight energy source [5]. While it has a gravimetric density nearly three times higher than kerosene (33 kWh/kg vs. 12 kWh/kg), its lower energy density presents a challenge for aircraft design [6].

In general, there are two ways hydrogen can be used as a power source for aircraft propulsion. The first is via hydrogen combustion in a gas turbine, and the second involves the use of fuel cells to convert hydrogen to electricity via an electrochemical reaction with oxygen. This electricity can either directly power an electric propeller engine or charge a battery as a buffer in a hybrid system. Compared to hydrogen combustion, fuel cells offer higher overall efficiency as losses related to combustion and conversion in mechanical energy systems are not observable. Additionally, fuel cells have a significantly lower environmental impact, as they only emit water vapor as a reaction product [7].

Proton-exchange membrane fuel cells (PEMFCs) and solid oxide fuel cells (SOFCs) are the most commonly considered types of fuel cells for aviation applications [8]. Among these, PEMFC technologies have been more extensively developed due to their use in mobile and automotive applications. In addition, they exhibit high specific power and require only short start-up times [9]. This study solely focuses on PEMFCs, which are introduced in more detail in 2.1.

Both established and new aerospace companies, including Airbus, ZeroAvia, Universal Hydrogen, Deutsche Aircraft, and H2Fly, have recognized the promising potential of fuel cells as energy converters for aircraft. They are currently developing megawatt-class hydrogen-based powertrains [9 p. 87, 10]. In contrast to the well-established gas turbine propulsion, the aviation industry has not yet acquired the same level of experience in handling fuel cells. Thus, a major challenge remains the thermal management (cooling) of the fuel cells, which dissipate approximately an equivalent amount of their electrical power output as heat [7]. Despite their high efficiency at ground level, fuel cells suffer from severe power losses under low-pressure conditions at high altitudes [11–14], which is the biggest challenge for their utilization in the aviation sector. The electrochemical cell potential, according to the Nernst equation, is directly

proportional to the natural logarithm of the ratios between the concentrations of the reaction´s products and reactants [15 p. 55]. Hence, the fuel cell power output would benefit from increasing the operating pressure. Pressurization, however, requires more energy for auxiliary equipment, such as an external compressor that can lower the net power [16, 17, 18 pp. 117–120]. Furthermore, pressurization involves additional stress for fuel cell components, as well as adding on system weight, volume, cost and complexity [12]. Another challenge in operating fuel cells at high altitudes is the influence of changing membrane hydration on the power output when the fuel cell is operated under the same thermal and stoichiometric conditions as at ground level [13, 19].

Therefore, extensive research and development efforts are necessary to enable the implementation of fuel cell systems in future aircraft generations. A promising approach is the optimization of operating conditions for aviation applications, which is being pursued by the Institute of Engineering Thermodynamics at the German Aerospace Center (DLR). Of particular interest is the optimization of cathode stoichiometry and stack temperature, as these parameters are associated with little additional power consumption compared to pressurization.

1.2. State of the Art

Chang and Gallman [11] conducted an investigation on a 1.2 kW Nexa® fuel cell power module, manufactured by Ballard (Burnaby, Canada), within an altitude chamber. They observed a net power decrease of approximately 25 % at the maximum tested pressure altitude of 5000 ft (1524 m).

Hordé et al. [13] investigated the behavior of PEMFC at three different altitudes (200 m, 1200 m, and 2200 m). The tested system, manufactured by Helion (Aix-en-Provence, France), consisted of 24 cells, with each cell having an active area of 100 cm^2. During the experiments, the researchers varied the air stoichiometric factors within a range of 1.5 to 2.5. At an altitude of 2200, the results revealed a significant reduction in power output of 50 % or more when the air stoichiometric factor dropped below two. This decrease in performance was attributed to a major decline of the maximum operable current, which was primarily caused by water management issues. By increasing the stoichiometric factor to 2.5, the power losses could be reduced to 8 %. However, this led to a tendency for the membrane to dry out. In addition, the compressor power became excessive, leading them to conclude that the system has an intrinsic maximum operable altitude.

Pratt et al. [12] investigated the effects of oxygen concentration and ambient pressure on the fuel cell performance. They analyzed the behavior of a PEM stack composed of 23 cells, each having an active area of 13 cm^2, from sea level up to 35000 ft (10668 m). The researchers found that the influence of airflow, and hence the stoichiometry, increases significantly at higher altitudes. Additionally, the losses attributed to variations in oxygen concentration were found to be less significant compared to the losses associated with changes in overall pressure. However, when both influences are combined equally, as observed during the increase in altitude, the measured voltage loss exceeds the sum of the observed losses from the separate cases. This observation suggests a possible compounding effect that could not be explained.

Werner et al. [14, 17, 19–21] performed measurements under low-pressure conditions (600 – 950 hPa), using a Hydrogenics HyPM® XR12 system consisting of 60 cells, each with an active surface area of 496 cm^2. The experiments involved varying the stack temperatures (45 – 65 °C) and cathode stoichiometric ratios (1.7 – 2.5). The key factors contributing to the decrease of the gross stack performance during low-pressure operation are the oxygen partial pressure and fuel cell humidification. Both are influenced by parameters such as cooling temperature, operating pressure, and cathode stoichiometric ratio [14]. Contrary to previous findings, the study revealed that the influence of stoichiometry variations on the gross stack performance within the

investigated operating range was relatively insignificant, regardless of the operating pressure [20]. Moreover, they demonstrated that when using an external compressor, the energy required for pressurizing the PEMFC exceeded the energy loss resulting from low-pressure operation [17, 21]. Consequently, they collectively postulated the need for a more comprehensive understanding of the interrelationships between pressure, cooling temperature, and stoichiometry under varying current demands to derive optimal control strategies.

Overall, all previous investigations consistently demonstrate that operating a fuel cell system at high altitudes results in lower efficiency and reduced power output. However, the magnitudes of these effects, as well as the influence of stoichiometry, exhibit a strong dependence on the specific fuel cell type and system design.

Further literature on the topic of fuel cells under low-pressure conditions, as well as an overview of the history of fuel cell-based aircraft, can be found in [9, 22].

1.3. Research Objectives and Scope

Within the scope of this thesis, a proton-exchange membrane fuel cell system, manufactured by Hydrogenics Corporation (Mississauga, Canada) is tested under the high-altitude conditions prevalent in the aviation environment. The experimental investigation is conducted using a test facility at the German Aerospace Center – the Altitude Test Chamber for Low Pressure Analysis of FC Systems (ATLAS). The PEMFC device under test is a self-humidifying fuel cell of type HyPM® HD 10-120 with 12 kW nominal power output.

The objective of this research is to develop a map of optimal operating conditions for the fuel cell system under altitude conditions, with the aim of increasing the net power output.

In a first phase, the behavior of the PEMFC system under low ambient pressure conditions will be characterized. This will be achieved by recording polarization curves at different pressure levels while utilizing the manufacturer's recommended parameters for stack temperature and cathode stoichiometry. The performance losses during operation under altitude conditions, as mentioned in the literature, will be quantified, and their origin will be analyzed and identified. Furthermore, the influence of low pressure on the auxiliary components will be examined in detail.

In order to meet the research objective and address the demands for optimizing operational parameters under altitude conditions as stated in [14, 17, 19, 20], a parameter study will be conducted in the subsequent phase. This will be done according to the principles of Design of Experiments (DoE). Within the framework of the parameter study, control parameters such as fuel cell operating temperature and cathode stoichiometry will be systematically varied at different pressure levels while considering various current requirements. The effects of the individual parameters on e.g., the cell voltage, the net power output or the water management will be analyzed.

Finally, the thesis will be concluded by comparing polarization curves recorded using both the standard parameters and the optimized parameters determined in this research.

2. Fundamentals

This chapter covers the necessary foundations for the following sections. First, the operating behavior, functionality and structure, as well as the thermodynamic and electrochemical principles of a fuel cell (FC) are discussed. Since the water management of a PEMFC has a decisive influence on its performance and reliability [18 p. 92], the impact of the components and operating conditions on the humidification are explained. Effects resulting from the lower pressure due to the altitude are concomitantly highlighted.

Finally, an overview is given of a special method of Design of Experiments, which was used for the experimental investigation.

An excellent and more comprehensive review of PEMFCs can be found in the references [15, 18, 23–25] and for DoE in [26–29].

2.1. Proton-Exchange Membrane Fuel Cells

Proton-exchange membrane (PEM) fuel cells, also known as polymer electrolyte membrane FCs, are devices that electrochemically transform the chemical energy of hydrogen and oxygen directly into electrical energy in the form of direct current. The by-products of the conversion only include heat energy and water.

2.1.1. Principles of Operation and Structure

Figure 2.1 illustrates the different components and the operation of a PEM fuel cell. The reaction gases are fed into the fuel cell via the flow fields of the bipolar plate (BPP) in an evenly distributed manner. Subsequently, the reactants diffuse through the so-called gas diffusion layers (GDL) and the microporous layers (MPL) to the catalyst layers (CL). These porous and electrically conductive layers are usually made of carbon cloth or carbon fiber paper, with platinum particles added to the carbon support as a catalyst in the CL [15 p. 8].

The anode and cathode compartments are separated by a proton-exchange membrane such as Nafion® [24 p. 26]. The PEM serves as an electrolyte and has some unique properties: it conducts only protons, is impermeable to gases, and prevents electrical short-circuiting of the electrolyte. This divides the cell reaction into two separate sub-reactions: oxidation (loss of electrons) at the anode and reduction (gain of electrons) at the cathode [23 p. 3].

The multilayer assembly formed by the gas diffusion layers, microporous layers, the catalyst layers, and the polymer membrane, is called the membrane electrode assembly (MEA).

During fuel cell operation, hydrogen as fuel is electrochemically oxidized in the anode CL and thereby releases electrons (e^-) and creates H^+ ions (or protons), as expressed by Equation (2.1). While the electrons move through an external circuit and can be used to do work (such as powering an electric motor), the protons get transported across the polymer electrolyte membrane. Within the cathode CL, these protons and electrons react with oxygen from the feed air and produce water [Equation (2.2)].

Both electrochemical reactions happen only at the three-phase boundary, at the surface of the catalyst at the interface between the electrolyte and the membrane [23 p. 3]. The overall redox reaction is shown in Equation (2.3).

⊕ Anode	$2\,H_2 \rightarrow 4\,H^+ + 4e^-$	(2.1)
⊖ Cathode	$4\,H^+ + 4e^- + O_2 \rightarrow 2\,H_2O$	(2.2)
Redox reaction	$2\,H_2 + O_2 \rightarrow 2\,H_2O\ (+\,heat)$	(2.3)

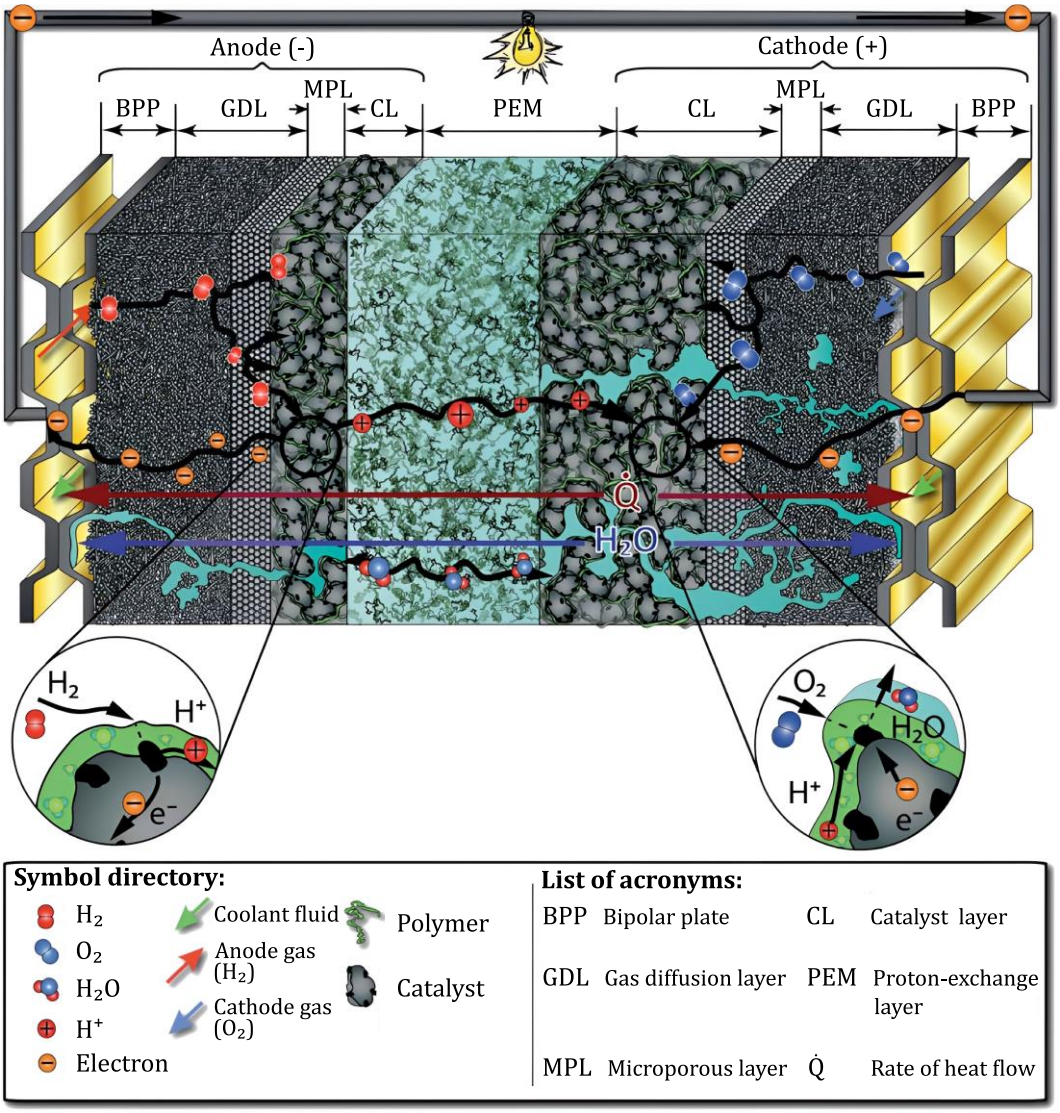

Figure 2.1: PEM fuel cell structure and operation scheme based on [30 p. 11].

The product water arises in vaporous and/or liquid phase, depending on whether the operating temperature and pressure allow condensation. It is removed from the system together with an excess flow of oxygen via the GDL and BPP.

A fuel cell delivers a current-dependent voltage of less than one volt, due to irreversible mechanisms faced during the electrochemical reactions [25 p. 128]. To achieve a technically applicable voltage level, the cells are electrically connected in series to form a 'stack'. Thereby the bipolar plates, which are stamped or milled on both sides, are located between the MEAs. They are usually made of graphite or stainless steel and provide electrically conductive contact [18 pp. 11–14]. In this way, the electrons released during the hydrogen oxidation reaction can be transported to the cathode of the neighboring cell to enable the reduction of oxygen there. In addition, the bipolar plates provide the cell structural rigidity. The energy in the form of heat resulting from the reduction (exothermic process) is removed via a circulating coolant in channels of the BPP.

The stack is held together by clamping the end plates. The contact pressure reduces the interfacial resistivity and thus minimizes losses. It also allows the stack to be sealed, preventing the reaction media from leaking.

The operation of fuel cells necessitates the use of auxiliary components, which are known as the balance-of-plant (BoP). The specific configuration of the BoP components depends on the type of fuel cell, the fuel, as well as the desired outputs of electricity and heat [18 p. 23].

In general, as illustrated in Figure 2.2, fuel cell systems can be categorized into four subsystems: the anode and cathode system, responsible for the fuel and oxygen (or air) supply, the electrical system, and the facilities for thermal management. The combination of the FC or stack with the balance-of-plant results in a fuel cell system. As the description of the test bench (Section 3) will cover the individual auxiliary components in detail, a comprehensive overview will be omitted at this juncture.

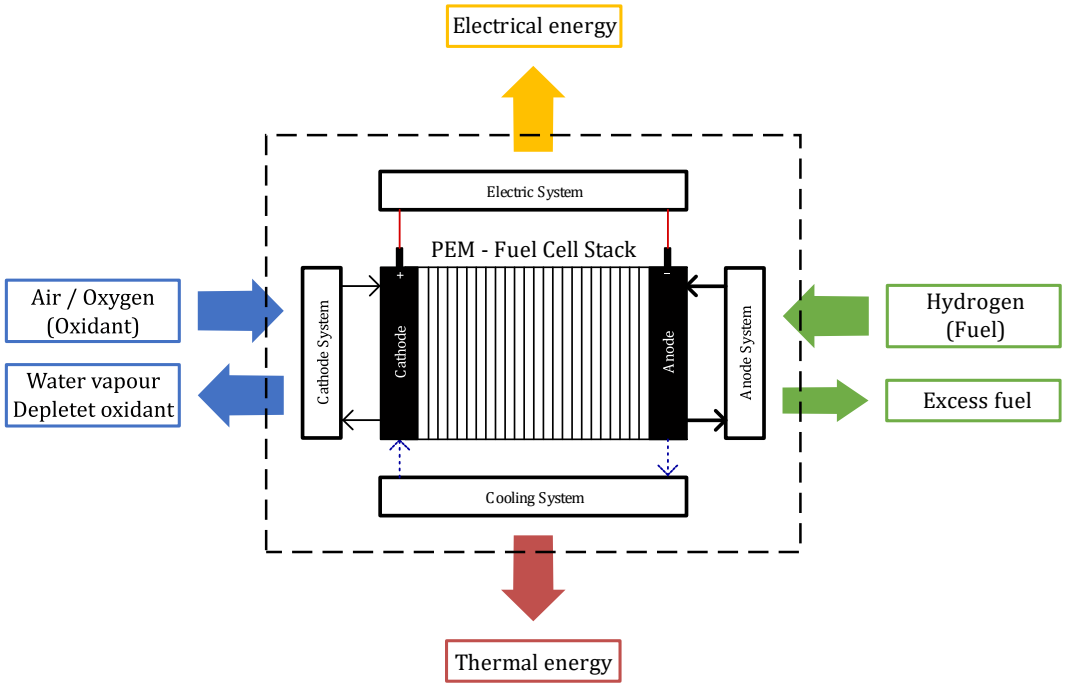

Figure 2.2: Schematic representation of the individual subsystems of a FC system based on [31 p. 18].

2.1.2. Basic Chemistry and Thermodynamics

Reviewing the overall reaction of a PEM fuel cell [Equation (2.3)], it is noticeable that it is the same as the reaction of hydrogen combustion. Therefore, by calculating the enthalpy of a hydrogen combustion reaction, the amount of usable (thermal) energy can be determined. This value is also known as the hydrogen´s heating value and indicates the amount of heat that may be generated by the complete combustion of one mole of hydrogen [15 p. 18]. If product water is present in liquid or vapor form after the reaction, a differentiation is made between the higher or lower heating value (HHV or LHV). When considering fuel cells, it is common to refer to the LHV because the heat of evaporation of water is not used [18 p. 33]. This corresponds to the difference between the higher and lower heating value.

However, due to the entropy produced in every chemical reaction (second law of thermodynamics), a portion of hydrogen's heating value cannot be converted into useful work. The Gibbs free energy change ΔG corresponds to this theoretically useful energy and is defined by [15 p. 20],

$$\Delta G = \Delta H - T\Delta S. \tag{2.4}$$

The product of temperature T in Kelvin (K) and change in entropy ΔS is the irreversible loss of the chemical reaction, which is converted into heat.

The enthalpies and entropies of formation for substances can only be determined experimentally and depend on temperature and pressure p. Values for reaction reactants and products can be obtained from databases such as [32, 33].

In the thermodynamic ideal case, the Gibbs free energy can be completely converted into electrical work [18 p. 30], i.e.

$$W_{el} = -\Delta G = zFE_0. \tag{2.5}$$

For each mole of mass transfer, a charge corresponding to the product of the Faraday´s constant, $F = 96.485\ \mathrm{As/mol}$, and the number of electrons z participating in the reaction is converted. For hydrogen-powered fuel cells, the number of electrons per molecule of H_2 is $z = 2$. The reversible cell voltage E_0 is the theoretical potential of a fuel cell when there is no net current flow. Under standard conditions ($p_0 = 1013.25\ \mathrm{hPa}$, $T_0 = 298.15\ \mathrm{K}$) and assuming liquid reaction products, the Gibbs free energy change is $\Delta G_0 = -237.13\ \mathrm{kJ/mol}$ [23 p. 19]. This results in a reversible cell voltage according to Equation (2.5) of

$$E_0 = \frac{-\Delta G_0}{zF} = \frac{-237.13\ \mathrm{kJ/mol}}{2 \cdot 96.485\ \mathrm{As/mol}} = 1.229\ \mathrm{V}. \tag{2.6}$$

The Nernst equation [15 p. 29] describes the dependence of the reversible cell voltage, or Nernst potential, on the temperature T, the partial pressures for hydrogen p_{H_2}, oxygen p_{O_2}, as well as water p_{H_2O}, i.e.

$$E_{T,p} = -\frac{\Delta H - T\Delta S}{zF} + \frac{RT}{zF} \ln\left(\frac{p_{H_2}\sqrt{p_{O_2}}}{p_{H_2O}}\right), \tag{2.7}$$

where $R = 8.314\ \mathrm{J/molK}$ is the molar gas constant. When liquid water is the product of the reaction, $p_{H_2O} = 1$. Since Nafion® fails at temperatures above 80 °C [23 p. 82], the operating temperature of PEM fuel cells is lower. At temperatures below 100 °C, the changes of ΔH and ΔS are very small. Therefore the enthalpy and entropy at standard conditions can be used as a reasonable approximation [15 p. 23]. Equation (2.7) can thus be simplified to

$$E_{T,p} = 1.4812 - 8.4645 \times 10^{-4}\, T + 4.3087 \times 10^{-5}\, T \ln\left(p_{H_2}\sqrt{p_{O_2}}\right). \tag{2.8}$$

Note that when air is used as cathode gas, the oxygen concentration (by volume) is 20.96 % [32 p. 172], so the oxygen partial pressure is only that fraction of the atmospheric pressure.

Consequently, the reversible cell voltage decreases with increasing operating temperature and increases with increasing pressure. However, when the cell voltage is increased by operating at a higher pressure, it must be considered that the energy required for compression can reduce the overall system efficiency.

2.1.3. Operational Voltage Losses

When the electrical circuit of a fuel cell is open and it is supplied with reactant gases, the actual voltage of the cell decreases from its Nernst potential. This reduction in voltage, typically less than 1 V [15 p. 39], is referred to as the open-circuit voltage (OCV). The underlying cause for this phenomenon is the permeation of elemental hydrogen and oxygen, in addition to the intended diffusion of hydrogen protons across the membrane to the cathode, causing the formation of a mixed potential [18 p. 52].

Nevertheless, a fuel cell provides useful work only if sufficient current is drawn. In such instances, the potential is expected to diminish further due to irreversible losses as a function of the current generated. These losses result from three key irreversibilities: activation losses, ohmic losses, and concentration losses.

Activation losses:

This type of loss is due to the inertia of electrochemical reaction kinetics. The overpotential arises from the finite rate of electron transfer through the phase boundary between the electrode and electrolyte. The oxygen reduction reaction is predominantly responsible for this loss as it is a slower reaction compared to hydrogen oxidation. Neglecting the activation losses of the hydrogen electrode is therefore possible. One straightforward approach to expressing this non-linear relationship of activation losses ΔU_{act} is through the Tafel equation [18 p. 48]:

$$\Delta U_{act} = \frac{RT}{2\alpha F} \ln\left(\frac{i}{i_0}\right), \tag{2.9}$$

where α is the charge-transfer coefficient, which is the fraction of the supplied electrical energy used to change the rate of an electrochemical reaction. The range of values extends from $0 \leq \alpha \leq 1$, with values typically below 0.5 for most cathode materials [18 p. 48]. The exchange-current density i_0 itself is a function of temperature, the catalyst used, the surface morphology of the electrodes and the reactant concentration [18 p. 51]. The Tafel equation is only valid if the current density $i > i_0$.

The inclusion of T in Equation (2.9) may suggest that an increase in temperature leads to a corresponding rise in overpotential. This notion is typically erroneous, as the effect of increases in i_0 with temperature is far greater [18 p. 48].

Ohmic losses:

Ohmic losses ΔU_{ohm} arise from resistance to ion flow in the electrolyte, as well as resistance to electron flow through the electrically conductive fuel cell components. These losses can be expressed by Ohm's law [18 p. 55]:

$$\Delta U_{ohm} = iR_i, \tag{2.10}$$

where i is the current density in A/cm^2. The total cell internal resistance R_i includes ionic, electronic, and contact resistance. The proton conductivity of the electrolyte membrane constitutes the most substantial portion in magnitude, whereby its thickness and hydration content play a significant role [25 p. 7]. Typical values for R_i are between 0.1 and 0.2 Ωcm^2 [15 p. 45].

Concentration losses:

The concentration (mass-transport) loss ΔU_{conc} arises due to the restricted diffusion rate of the reaction gases to the three-phase boundary, where the electrochemical reaction transpires. The insufficient availability of reactants at the electrode causes a concentration gradient, which leads to a decrease in the cell voltage. The limiting current density i_L refers to the condition in which reactants are consumed at a rate equivalent to their arrival at the electrode surface [15 p. 47]. The fuel cell is unable to generate a current beyond this threshold. Based on the Nernst equation (2.7), the following description can be used to characterize the mass transport losses:

$$\Delta U_{conc} = B \ln\left(\frac{i_L}{i_L - i}\right), \tag{2.11}$$

where B is a parameter that depends on the fuel cell and its operating state [18 p. 56].

Due to the nonuniform conditions across the porous electrode area, the limiting current in practical fuel cells is only locally attained [15 p. 47]. The diffusion properties of the GDL, or more generally of the electrode, can further be altered by water condensation as well as by local variations in temperature, gas composition, and partial pressures. As a result of the complex

interplay of these factors, a more suitable analytical solution for modeling the system is not readily available. However, several empirical approaches are available, such as those presented in [18 p. 56].

2.1.4. Polarization Curve

Figure 2.3 depicts a typical profile of the actual cell voltage versus current density, the polarization curve. The various mechanisms responsible for deviations from the reversible cell voltage can be summarized using the polarization curve. Moreover, the three regions where the losses described in Section 2.1.3 dominate are indicated.

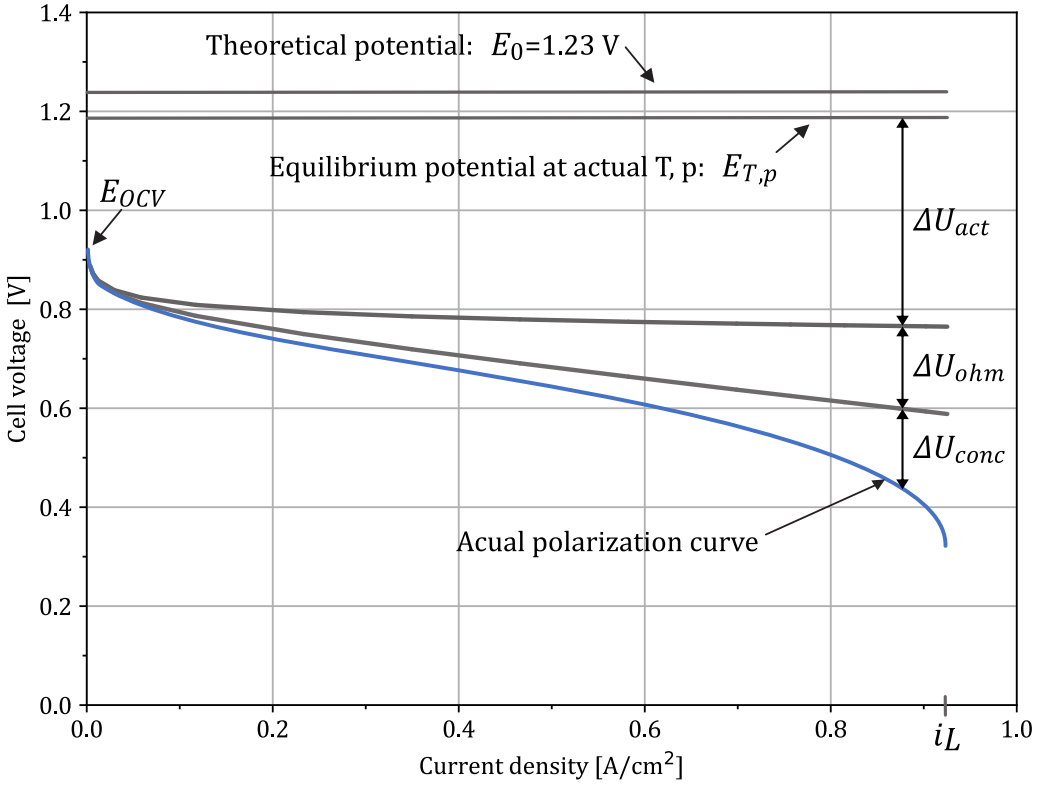

Figure 2.3: Typical polarization curve of a PEM fuel cell.

A reasonably accurate approximation of the fuel cell polarization curve can be obtained from

$$U_{cell} = E_{T,p} - \Delta U_{act} - \Delta U_{ohm} - \Delta U_{conc}, \tag{2.12}$$

cf. [15 p. 52]. It is important to note that fuel cells - similar to other galvanic cells - deliver maximum power at half-open-circuit voltage, just before the cell voltage drops abruptly [23 p. 26]. Operating the fuel cell above this maximum provides no additional benefits and reduces efficiency and lifetime. Therefore, it is avoided in practical applications.

2.1.5. Efficiency of Fuel Cells

The efficiency η of a fuel cell is defined as a ratio between the electrical energy generated W_{el} and the chemical energy of hydrogen W_{H_2} which is consumed. Specifically, as illustrated by:

$$\eta = \frac{W_{el}}{W_{H_2}} = \frac{U_{cell} \cdot I}{W_{H_2}}, \tag{2.13}$$

the electrical energy produced is equal to the product of cell voltage U_{cell} and cell current I [15 pp. 59–60].

Assuming the complete conversion of the energy content of hydrogen (heating value) into electrical energy, the energy value of hydrogen consumed can be determined using Faraday's law [15 p. 60],

$$W_{H_2} = \Delta H \frac{I}{zF}. \tag{2.14}$$

The combination of Equations (2.13) and (2.14) reveals that fuel cell efficiency is directly proportional to cell potential. When considering the lower heating value of hydrogen ($\Delta H_{LHV} = 241$ kJ/mol [15]), the fuel cell efficiency η_{LHV} can be determined by [15 p. 60]:

$$\eta_{LHV} = \frac{U_{Cell}}{1.254\,V}. \tag{2.15}$$

In practice, fuel cells are supplied with an excess of hydrogen beyond that required for the stoichiometric reaction, resulting in an unused excess of hydrogen [18 p. 36]. The fuel utilization coefficient η_{fuel} is the ratio between the utilized and supplied hydrogen and is therefore the reciprocal of the anode stoichiometry (λ_a). To obtain the fuel cell (gross) efficiency $\eta_{FC,LHV}$, this coefficient must be multiplied by the lower heating value efficiency η_{LHV} [15 p. 61].

When calculating the system efficiency $\eta_{Net,LHV}$, the power losses of the BoP components must also be included. It can be calculated using:

$$\eta_{Net,LHV} = \frac{P_{Net} \cdot \eta_{fuel}}{I \cdot n_{cells} \cdot 1.254\,V}. \tag{2.16}$$

2.1.6. Reactant Flow Rates and Stoichiometric Ratio

The gas flow rates and amount of product water can be directly determined from the generated electrical current I. Faraday's law can be applied to calculate the consumption rates $\dot{n}$ of a single cell based on the valence z of the participating ions [15 p. 124], i.e.

$$\dot{n} = \frac{I}{zF}. \tag{2.17}$$

To determine the reactant consumption of the entire fuel cell stack, the number of cells n_{cells} must also be considered. With the molar masses M_i of the corresponding substance, with $i = H_2, O_2, H_2O$ (see e.g. [32, 33]), the following two equations are obtained for the mass flow rates $\dot{m}$ of reactants' consumption [15 p. 124]:

$$\dot{m}_{H_2} = \frac{I}{2 \cdot F} \cdot M_{H_2} \cdot n_{cells}, \tag{2.18}$$

$$\dot{m}_{O_2} = \frac{I}{4 \cdot F} \cdot M_{O_2} \cdot n_{cells}. \tag{2.19}$$

The rate of the generated product water can be determined with [15 p. 124]:

$$\dot{m}_{H_2O} = \frac{I}{2 \cdot F} \cdot M_{H_2O} \cdot n_{cells}. \tag{2.20}$$

The reactants need to be supplied beyond their consumption, particularly on the cathode side, to remove, for example, the generated product water with an excess flow rate from the cell. The ratio between the actual mass flow rate $\dot{m}_{act}$ of a reactant at the cell inlet and the consumption mass flow rate $\dot{m}_{cons}$ of that reactant is called the stoichiometric ratio [15 p. 126]. The cathode stoichiometry can be calculated using the ideal gas equation:

$$\lambda_c = \frac{\dot{m}_{act}}{\dot{m}_{cons}} = \frac{\dot{V}_{O_2} \cdot \rho_{O_2} \cdot 4 \cdot F}{M_{O_2} \cdot I \cdot n_{Cells}}. \tag{2.21}$$

If the actual volume flow rate of the air $\dot{V}_{air}$ is to be considered, it is important to note that the oxygen fraction is determined by multiplying with the corresponding density of air ρ_{air} and the mass fraction. For dry air, the mass fraction for oxygen is 0.23161 [31 p. 172].

2.1.7. Water Management

The key challenge in PEMFC operation is the adjustment of the optimal membrane humidity, called water management.

A shortage in membrane humidity not only decreases the proton conductivity, resulting in lower cell performance but can also cause permanent membrane damage. As a consequence of dehydration, the membrane becomes more susceptible to the formation of pinholes, which accelerates the degradation process, ultimately leading to membrane failure [34]. On the other hand, a surplus of water at the cathode or anode may result in condensation of water, known as flooding, which blocks the pores of the active catalyst surface or GDL and consequently reduces the performance of the fuel cell.

Increasing the temperature and water content leads to an improvement in membrane conductivity [23 p. 80]. The trade-off between maximum membrane conductivity and risk of flooding remains difficult to achieve. However, this is necessary for a high-performing and steady operation.

The relative humidity of the cathode outlet gas is one of the simplest and most reliable methods for monitoring membrane hydration [18 pp. 94–98]. Relative humidity (rH) is defined as the ratio between the vapor pressure of water (p_{H_2O}) and the saturated vapor pressure (p_{sat}), which is the maximum amount of water vapor the air can hold at a given temperature [15 p. 131]. The saturation pressure values can be obtained from thermodynamic tables, such as in [32 pp. 154–157]. The saturation pressure value is only a function of the temperature [15 p. 131]. In this study, p_{sat} was calculated using an equation according to the International Association for the Properties of Water and Steam (IAPWS) [35], as it is valid over a wide temperature range (0 – 374 °C).

If the water content of the inlet is negligible, Equation (2.22) proposed in [18 p. 98] can be used to determine the relative humidity at the cathode outlet:

$$rH_{out} = \frac{2r_{O_2,in}}{\lambda_c + r_{O_2,in}} \frac{p_{out}}{p_{sat}(T_{out})}. \tag{2.22}$$

Where $r_{O_2,in}$: oxygen concentration at the cathode inlet,
λ_c: cathode stoichiometry,
p_{out}: pressure at the cathode outlet,
$p_{sat}(T_{out})$: saturation pressure as a function of the temperature at the outlet.

If the oxygen concentration is at standard conditions ($r_{O_2,in} = 0.2096$), it is evident that the water management is only dependent on the operational parameters, including cathode stoichiometry λ_c, stack temperature T, and operating pressure p. Similarly, the water balance can also be influenced by system parameters, such as flow field design, membrane type, and membrane thickness [34]. However, as the present system will not undergo any structural modifications, this is not part of the investigation.

2.2. Design of Experiments

Design of Experiments (DoE) is a statistical method for efficiently planning and evaluating experimental series [27 p. 1]. The objective of DoE is to methodically investigate and optimize processes or systems by systematically varying input parameters and observing the effects on output parameters (response variables). DoE is therefore a crucial tool in research and development for establishing empirical models and analyzing experimental results to make informed decisions and gain scientific insights.

Related to this study, the primary objective is to optimize a system by quantifying and understanding the effects of various input variables, such as temperature and pressure, on a specific output response, such as the performance of a fuel cell. The input variables are divided into controllable variables, the so-called (treatment) factors, and the uncontrollable variables, referred to as disturbances. The set of all changeable input variables is called parameters [27 p. 5].

When systematically varying all possible factors, the number of potential combinations to be tested grows exponentially, i.e.

$$n_{total} = {n_l}^{n_f}. \tag{2.23}$$

However, various design of experiments methodologies allow to achieve a good trade-off between effort and benefit. Through the strategic arrangement of different experiments, DoE approaches reduce the number of necessary experimental runs without losing sufficient knowledge about scientific relationships.

In cases with only a few numbers of factors ($n_f \leq 3$) affecting the system under investigation, a full factorial experimental design can be applied. The total number of experiments n_{total} required is then determined by the number of factors and their respective levels n_l, as shown in the following equation.

Fortunately, if there are four to five or more factors, it is usually unnecessary to run all possible combinations of factor levels [28 p. 7]. The best possible characterization of the system then faces an unaffordable experimental effort.

Assuming that the system is linear, it is possible to apply a fractional factorial design. Information on low-order interactions can still be obtained. Subsequent detection of nonlinearities is no longer possible.

However, fuel cells exhibit complex nonlinear behavior [36, 37]. If nonlinearities are taken into account, the response surface methodology (RSM) can be employed. RSM offers the possibility to perform modeling and analysis of complex problems in which a response of interest is influenced by several variables and the objective is to optimize this response [28 p. 478]. In general, nonlinearities can only be detected if more than two levels are selected for each factor.

The central composite design (CCD) is the most commonly used second-order design [26 p. 578], which means that it provides the ability to detect quadratic effects. A CCD is composed of a standard first-order design with orthogonal factorial points ('cube') that are augmented by axial points - the star. Additionally, a center point is included in the design. Thus, the CCD offers a good compromise between effort and the possibility to detect interactions.

All of the experimental design approaches presented so far are subject to the limitation that they can only be applied in unrestricted, i.e., orthogonal experimental spaces. However, it has been observed that in the case of PEMFC systems, there are various restrictions of the experimental space, such as flooding and reduced maximum current under low-pressure conditions [20, 37].

One approach to statistical experimental design in constrained experimental spaces is the Box-Behnken design [28 pp. 503–504]. This method involves placing experimental points not at the corners, thereby avoiding the need to test combinations of variable limits that may be impossible to realize. This results in a sphere as the experimental space.

For the FC system, standard response surface designs are not suitable. Firstly, because the experimental space has various restrictions that lead to an irregular experimental space. In case certain factor combinations cannot be realized during the experiments, a new experimental design based on a reduced candidate matrix should be possible to create. For this purpose, the data obtained from the experiments that have already been conducted should be included in the creation of the new design.

Since the advent of affordable high-performance computing, more complex and powerful design criteria have been developed, such as optimal designs that are utilized in such cases [37]. These designs offer the experimenter complete flexibility in determining the experimental plan, including the ability to set arbitrary levels of factors with non-equidistant steps. The candidate list resulting from the combinations of these factor levels (fully factorial) can be subsequently sorted out by restrictions. The plans are determined iteratively by selecting those individual experiments that are optimal for fitting the intended regression model. There are various optimality criteria, with the D-optimal plan being the most widely used [29 p. 229]. D-optimal designs minimize the volume of the joint confidence region for the regression coefficients, with 'D' standing for the determinant of the information matrix [27 p. 56]. In particular, the objective of covering all interactions with a small number of experiments prevents these experimental designs from being completely orthogonal. This means that certain correlations cannot be fully eliminated. Nonetheless, this is a minor disadvantage in the evaluation via multiple regression [38]. Computational algorithms, typically relying on an exchange algorithm procedure, are necessary to create these designs.

A more detailed description of the methodology and a mathematical description of the various criteria would exceed the scope of this thesis and is therefore omitted. Further details can be found in the literature, see e.g. [26–29].

3. Experimental Setup

This chapter provides a detailed overview of the test facility – the Altitude Test Chamber for Low-Pressure Analysis of FC Systems. ATLAS was developed and assembled at the Institute of Engineering Thermodynamics located at the DLR site in Stuttgart. The test facility includes an adequate gas supply, cooling system, electric sink, measurement instrumentation as well as a LabView-based control and data collection system.

As part of the PEMFC research conducted at the DLR department of Energy System Integration, and also within the scope of this thesis, the test bench has been constantly upgraded, for example, by integrating new sensors, as well as safety-relevant components and an improved air supply system.

In the following sections, the four characteristic subsystems and the stack, which were briefly introduced in Section 2.1.1, will be described in detail. However, prior to delving into these elements, particular attention is given to the low-pressure chamber, which is crucial for aviation-related testing. It is one approach to investigate the FC system under altitude conditions.

The piping and instrumentation diagram (P&ID) of the entire test setup is provided in Appendix A.1. Additionally, Appendix A.2 includes a complete list of all installed sensors, including their measurement range and errors.

3.1. Altitude Chamber

The centerpiece of ATLAS is the low-pressure chamber, shown in Figure 3.1a, which has a capacity of approximately 1500 liters and is capable of simulating altitude conditions for FC systems. A powerful 8 kW vacuum pump, located in a separate room, is used to generate low pressure. Based on the air mass flow rate, the absolute operating pressure can be adjusted using a vacuum regulator. The air used for operation is drawn from the laboratory environment, which is blown via a mass flow controller in the test chamber. To counteract oxygen depletion, the supplied fresh air mass flow must be significantly (at least 1.75 times) higher than the cathode mass flow required for FC operation. At a flow rate of 1000 slpm, the pressure can be lowered to 200 hPa, which corresponds to an altitude exceeding 11 km according to the International Civil Aviation Organization (ICAO) standard atmosphere ISA [39]. This enables the simulation of the entire troposphere (and beyond), where the majority of commercial air traffic takes place.

Furthermore, the inlet air temperature can be regulated using a heat exchanger that is coupled to an integral process thermostat. This allows the air to be pre-conditioned after it has passed through the mass flow controller (MFC). However, due to the fact that the chamber itself represents a very large thermal mass, it is currently not possible to decrease the temperature to - 56.5 °C prevailing at an altitude of 11 km [39]. Consequently, in the present experiment the blower inlet air temperature was consistently maintained at 20 °C.

The suction system mainly focuses on the cathode exhaust, as can be seen from the gray tube in Figure 3.1b. However, for safety reasons, a small volume fraction is also directly suctioned from underneath the ceiling of the chamber to prevent the accumulation of an explosive hydrogen-air mixture in the event of, e.g., a leak in the anode circuit.

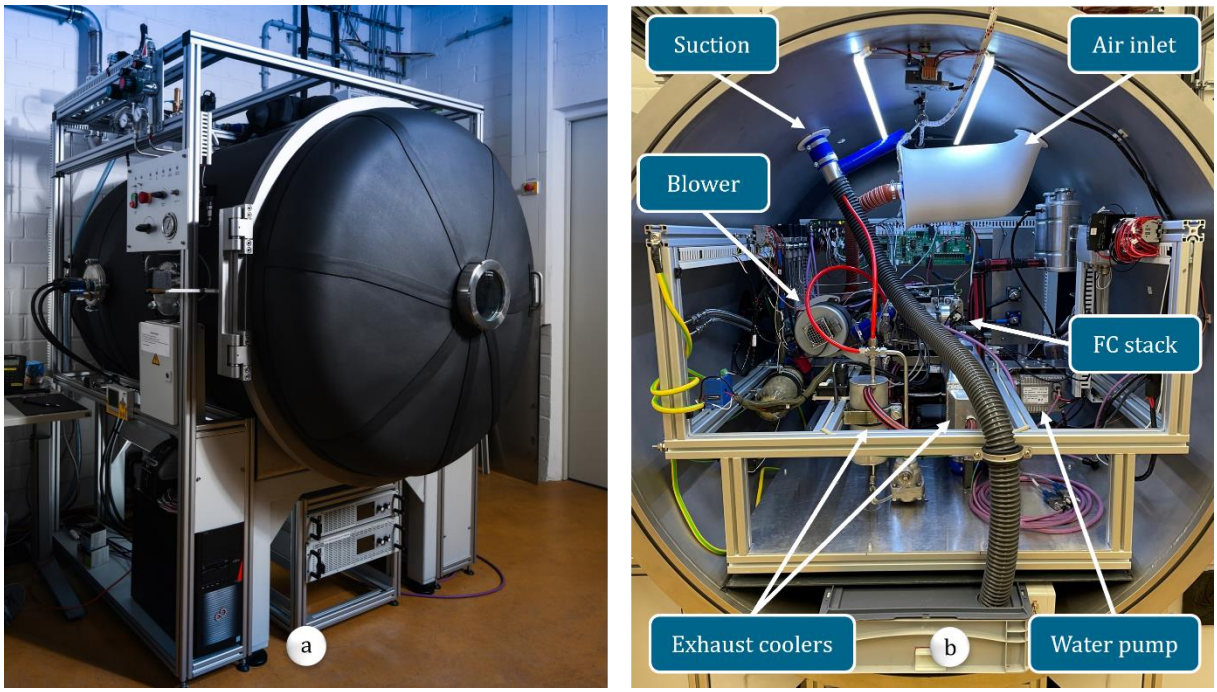

Figure 3.1: Exterior (a) and interior (b) overview of the altitude chamber.

Inside the chamber, sensors monitor various atmospheric parameters such as pressure, temperature, humidity, oxygen content, inlet mass flow, and the corresponding inlet temperature. For safety reasons, a hydrogen sensor is also located beneath the ceiling, which initiates an emergency shutdown in the case of H_2 accumulation.

3.2. Fuel Cell Stack

The PEMFC device under test is a self-humidifying fuel cell of HyPM® HD 10-120 type manufactured by Hydrogenics Corporation. The rated electrical power is 12 kW (at 200 m altitude) and the stack is composed of 120 cells, each with an active area of 195 cm^2. Hydrogenics' HyPM® HD series is characterized by rapid response to commanded current changes, high fuel efficiency as well as unlimited startup cycles with no adverse effect on stack durability [40]. Table 3.1 provides an overview of the key parameters of Hydrogenics' fuel cell.

Property	Specification
Rated electrical power	12 kW
Operating current	$0 - 190\ A_{dc}$
Operating voltage	$60 - 120\ V_{dc}$
Efficiency (μ_{LHV})	$\leq 52\ \%$
Operating pressure	≤ 120 kPa
Maximum fuel flow rate	≤ 160 l/min
Process air flow rate	≤ 950 l/min
Coolant temperature at coolant outlet	$50 - 65$ °C
Heat rejection	≤ 16 kW
Coolant flow rate	≥ 48 l/min

Table 3.1: Specification of the fuel cell system [40].

The system features an electronic control board, called Power Distribution Controller (PDC), which controls all FC balance-of-plant actuators - the process air blower, the hydrogen recirculation pump, and the hydrogen supply and purge valves. It is additionally the communication interface (via a controller area network (CAN) communication) with all external systems.

The current density-dependent default control parameters for purge-off times and cathode stoichiometry are presented in Table 3.2, wherein linear interpolation is employed by the PDC to estimate values between the listed ones.

Current density [A/cm^2]	Purge-off time [s]	Cathode stoichiometry [-]
0.0	50	3.0
0.1	40	2.8
0.2	35	
0.3	30	
0.4	25	2.6
0.5	20	
0.6	15	
0.7	10	
0.8	8	
0.9	5	

Table 3.2: Standard control parameters for anode purge-off times and cathode stoichiometry.

The cell voltages are measured via the embedded cell voltage monitoring board. Even though only two cells are measured together, monitoring the 60 cell pairs provides valuable information about the state of health of the stack.

According to the manual [40], even operation at altitudes of up to 1600 m (835 hPa) is permitted for the non-pressurized FC system. However, in this study, such operational limits, among others, are exceeded to address the research question.

3.3. Cathode System

The cathode subsystem is responsible for the supply of the oxidant (air for this system) and the removal of the excess product water and cathode exhaust gas. The filter through which the cathode air is drawn is located within an inlet duct of the altitude chamber, see the white bell in Figure 3.1b. This arrangement prevents the suction of oxygen-depleted gas to the cathode inlet.

As depicted schematically in Figure 3.2, the air is supplied by a process air blower, which is controlled to ensure the correct stoichiometry throughout the full operating regime of the system. There is no external humidification or actual compression of the cathode air, resulting in a simpler system design. However, a certain amount of overpressure must be generated by the blower ($\Delta p_{max} \approx 70$ hPa) to offset the stoichiometry-dependent pressure loss across the stack.

The cathode exhaust consists of warm, oxygen-depleted air and water, and cannot be directly released into the environment during operation within the chamber. Otherwise, the chamber's atmosphere would be drastically altered. Consequently, the cathode exhaust is cooled and dried using a commercial intercooler.

The sensors depicted in Figure 3.2 facilitate a distinct identification of the phenomena taking place within the cathode system.

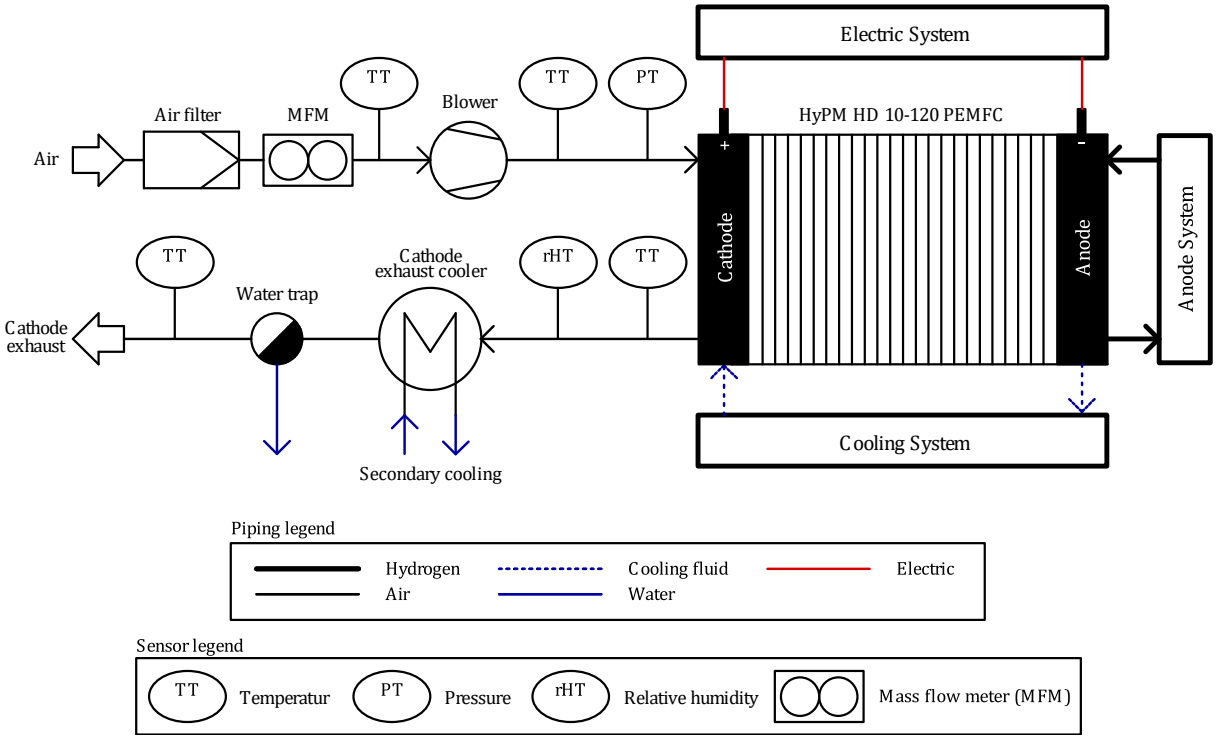

Figure 3.2: Simplified schematic process flow diagram of cathode system.

3.4. Anode System

The anode subsystem is responsible for providing the fuel (hydrogen) and disposing of the anode exhaust gas. The schematic process flow diagram of the anode subsystem is shown in Figure 3.3. Hydrogen is fed into the system by the central laboratory supply at a pressure of approximately 6 bar. The anode pressure closely follows that on the cathode with a slight overpressure (~ 40 hPa) as this hydraulically pushed water through the PEM and thus improves proton transport [15 p. 86]. This is realized by a mechanical pressure regulator that references the cathode pressure using a pilot line. The installed sensors can also be observed in Figure 3.3.

In order to enhance the hydrogen supply to the stack, it is common to supply the anode with an excess of hydrogen beyond what is consumed in the reaction. The release of unreacted hydrogen is inefficient and decreases the overall efficiency of the system. To mitigate this issue, the system is operated in recirculation mode, which allows the unused hydrogen to be transported back to the anode inlet for reuse. This approach also helps to maintain a uniform level of humidity on the anode side [18 p. 124]. Nonetheless, periodic purging is still necessary to remove the accumulated inert gases and water from the anode side. For this purpose, a solenoid valve at the outlet of the anode subsystem is opened in current-dependent intervals, refer to Table 3.2 (usually open for 700 ms). The gaseous mixture must be cooled and dried, like the cathode exhaust. Since it contains unreacted hydrogen, it is fed directly into the suction hose to prevent hydrogen accumulation in the chamber.

The test rig also offers the possibility of feeding nitrogen into the anode system instead of hydrogen. The process of flushing with nitrogen is particularly aimed at inerting during shutdown and limiting degradation, thereby prolong the life of the stack.

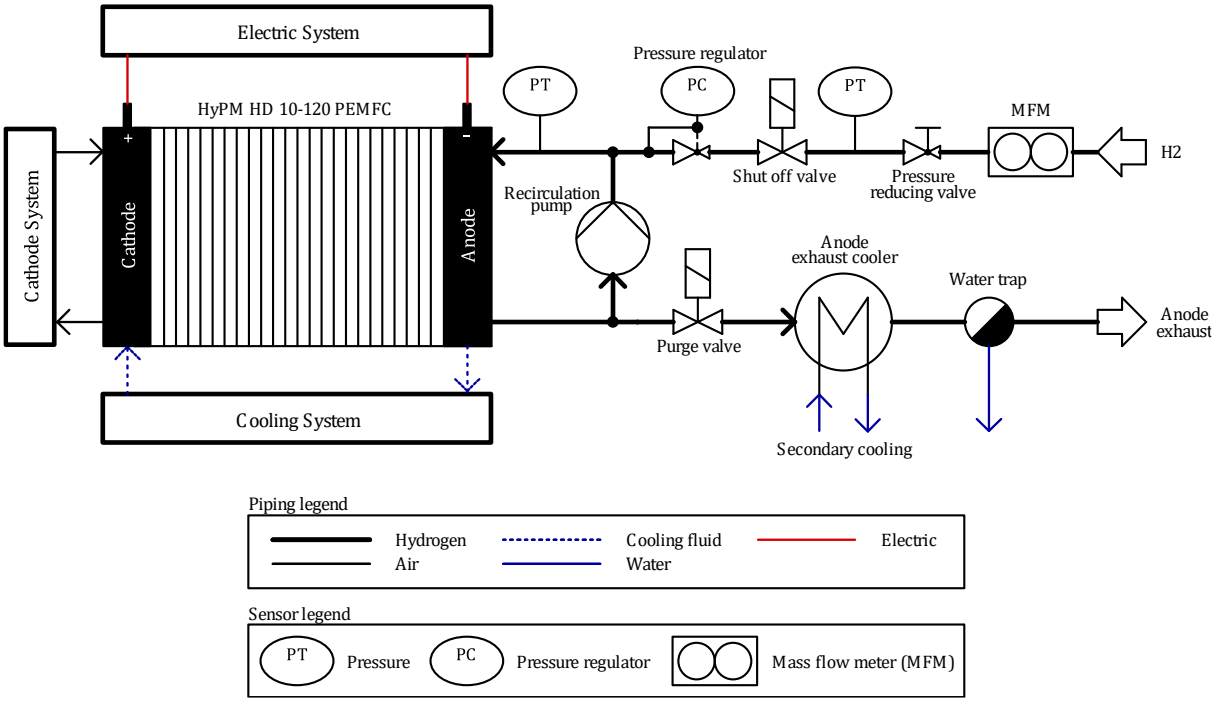

Figure 3.3: Simplified schematic process flow diagram of anode system.

3.5. Cooling System

As mentioned previously, cooling of both the exhaust gases and the FC stack is necessary, resulting in the system having two cooling circuits. Both cooling circuits are connected to the laboratory cooling system via plate heat exchangers located outside the chamber.

The FC is connected to the primary cooling circuit to ensure a proper fuel cell temperature. Glysantin is used as coolant due to its superior heat dissipation properties compared to water, as well as its higher boiling point and ability to provide corrosion and frost protection. To avoid electrical conductivity, the coolant is deionized via a filter. The temperature regulation is not achieved by the pump rate but rather through a mixing valve that varies the volume flow through the plate heat exchangers depending on the desired stack (outlet) temperature. In this process, the coolant pump maintains a constant rotational speed. The standard current density-dependent temperature control parameters are outlined in Table 3.3, with linear interpolation applied to values between the specified parameters.

Current density [A/cm²]	Stack temperature [°C]
0.0	50
0.09	
0.24	55
0.5	
0.7	60
0.9	

Table 3.3: Standard control parameters for the stack temperature.

An additional cold-water circuit is utilized to draw heat from the thermic condensers located on both the anode and cathode sides.

Figure 3.4 shows the schematic process flow diagram of the cooling system is presented below. Sensors are solely located in the primary cooling circuit, which measures the stack's inlet and outlet temperatures, mass flow rate, and pump power.

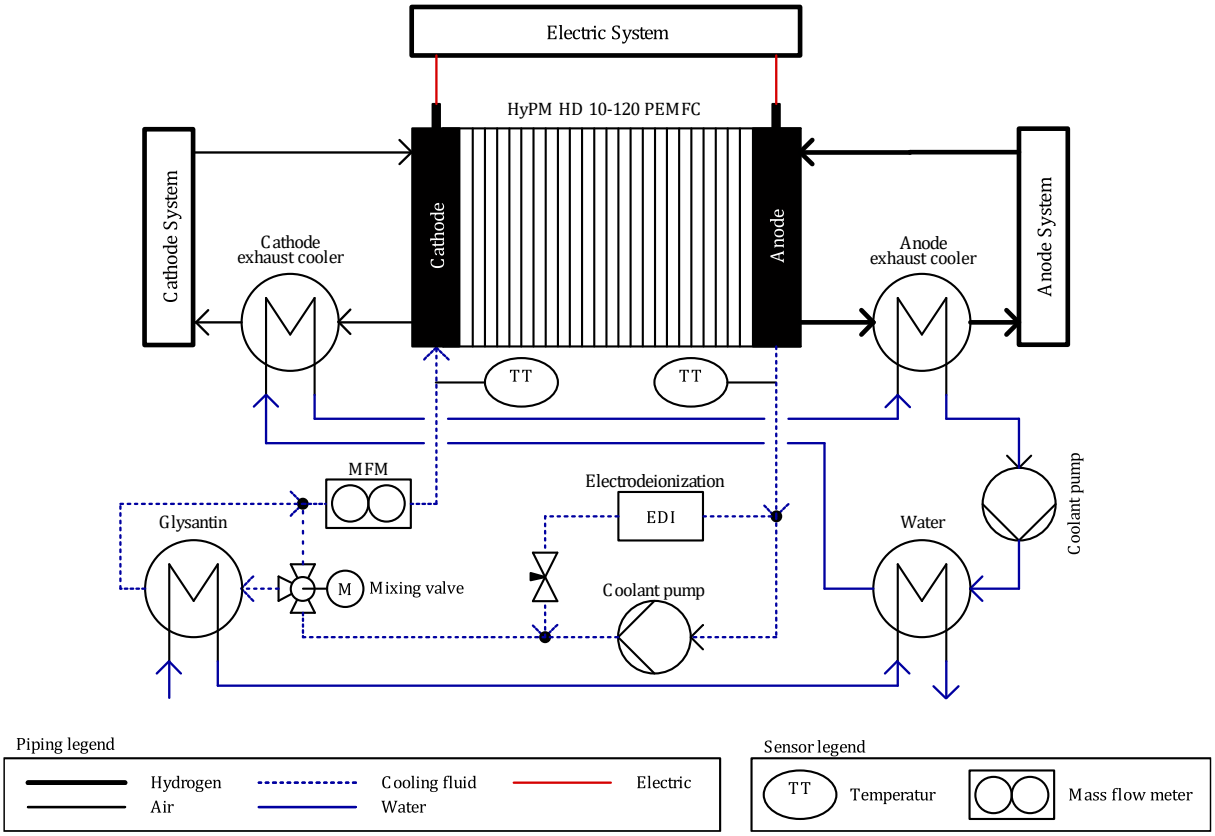

Figure 3.4: Simplified schematic process flow diagram of the cooling system.

3.6. Electrical System

An electric sink regulates the electrical power generated by the stack which is then fed into the grid. The electronic load also enables accurate measurement of the stack's total power output via current and voltage sensing. In the event of system failures, the load can be immediately disconnected from the system by opening high-current contactors. This ensures rapid shutdown to prevent any damage to the fuel cell. If the connection to the electronic load is disconnected, it is necessary to ensure that the reactants can be discharged. For this purpose, a 150 Ω wirewound resistor is included in the circuit, which converts any remaining output power into heat. To ensure reliable operation of the stack under non-standard conditions, the BoP components and almost all sensors are supplied from an external power supply rather than from the stack. The current drawn by the recirculation pump and blower is measured using current transducers. Measuring the power consumption of to these two components, the resulting net power output of the FC system can be determined.

3.7. Data Acquisition and Control

The sensor signals are either transmitted directly via the CAN-Bus protocol to the test stand computer or, alternatively, they are converted by a WAGO analog-to-digital system before being transmitted. Real-time system control and data logging are realized via LabVIEW software. The LabVIEW software incorporates a human-machine interface that allows for the control of the fuel cell system as well as other instruments, such as the process thermostat or the vacuum pump. Furthermore, the operational parameters of the PEMFC system and the entire measurement setup can be monitored in real-time. Some data are also plotted in real-time graphs to provide a better visual representation of the temporal dynamics.

An automated profile execution feature is available, allowing the import of a CSV (comma-separated values) file format. By providing parameters including chamber pressure, temperature, and current, it is possible to simulate aviation-specific mission profiles.

4. Methodology

This chapter presents the methodology used to achieve the objective of developing a map of optimal operating conditions at different low-pressure levels. First, the general approach is summarized in Section 4.1 which is then discussed in more detail in the following sections of this chapter.

4.1. General Approach

In general, the approach can be divided into two phases:

- Phase 1: Polarization curves with default control parameters.
- Phase 2: Design and execution of a parameter study.

The first phase involves the collection of baseline data by recording polarization curves at different pressure levels using the default control parameters for stack temperature and cathode stoichiometry provided by the manufacturer. This phase allows to identify the challenges associated with the operation of fuel cells under high altitude conditions (see Section 5.1).

Subsequently, to mitigate the pressure-dependent issues identified in phase 1, a parameter study is performed in the second phase to determine the optimal operating conditions for various pressure levels. Therefore, the second phase encompasses the design and execution of the parameter study. Hereby, the second phase can be subdivided into smaller stages based on the common guidelines for DoE (e.g. in [28 p. 14] or [26 p. 7]):

a. Recognition and statement of the problem.
b. Specify factors, levels, as well as response variables.
c. Run pilot experiments.
d. Choice of experimental design.
e. Conduct the experiment.
f. Statistical analysis of the data.

} Pre-experimental planning.

It is important to acknowledge that experiments, or the design of experiments, are usually iterative. As such, decisions must be constantly reviewed and revised if necessary. The methodology outlined in the following Sections should be viewed as a final iteration of the experimental design.

4.2. Phase 1: Polarization Curves with Default Control Parameters

4.2.1. Test Procedure for Recording Polarization Curves

For characterizing the performance of a PEMFC system, a standard procedure is to record a polarization curve by measuring the voltage versus current response.

To ensure comparability of experimental findings across institutions and companies, standardized methods have been developed worldwide to unify testing procedures. One such method is the uniform test protocol developed through the 'Fuel Cell Testing, Safety and Quality Assurance' (FCTES^{QA}) project of the European Union (EU) which was verified through a round-robin test carried out in both the EU and the USA [41]. The performance characterization presented in this thesis is based on the test module PEFC ST 5-3 developed in the FCTES^{QA}. Further international test procedures differ only slightly from one another and are outlined in [42].

An exemplary current profile, used for recording the polarization curve at an ambient pressure of 1000 hPa, is presented in Figure 4.1. As indicated in green, prior to each test procedure, the fuel

cell is preconditioned to set the fuel cell stack in a well-defined and reproducible initial state. This is done by a dynamic current profile developed within the DLR department of Energy System Integration, specifically for the HD-10 stack, which mitigates reversible degradation using larger current steps as well as a sinusoidal profile. This measure is intended to ensure the reproducibility of experimental results.

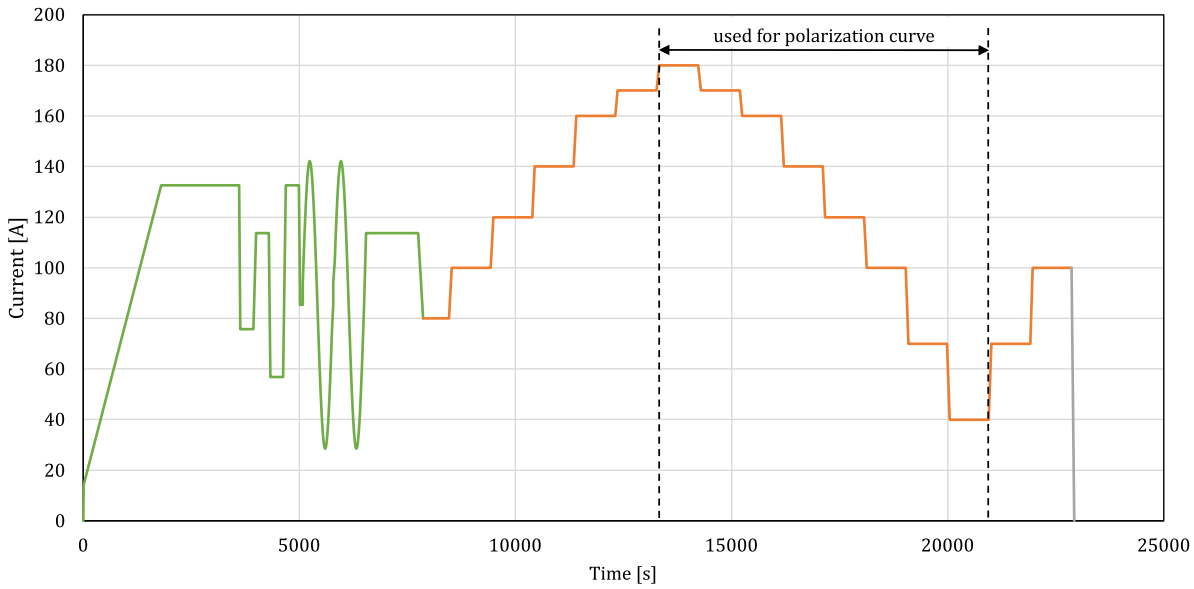

Figure 4.1: Current profile of test procedure for recording the polarization curve at ambient pressure of 1000 hPa.

After the preconditioning procedure, the stack voltage is measured at varying current densities to derive the polarization curve. The measurement starts at 13300 s with around 50 % of the maximum stack current to be investigated and then increases in steps up to 180 A in the present example. Subsequently, the current is gradually reduced to a minimum value, which is still substantially above 0 A (OCV). By avoiding setpoints close to or at OCV, the operating time in regions with more rapid degradation can be reduced. As shown in Figure 4.1, typically only points are used for the polarization curve that are recorded with decreasing current steps, i.e., where a hysteresis effect can be detected. This effect, noticeable when comparing the voltage response between the ascending and descending portions of the current profile, is attributed to an improved humidity content [15 pp. 267–268]. Finally, at 20950 s, the current is increased in steps up to the same level (100 A) as at the beginning of the polarization curve at 23000 s. Then the current is reduced to 0 A for safe system shutdown, see the gray line.

A total of six polarization curves are generated with different ambient pressure levels, i.e., p $\approx$ 1000 hPa to 500 hPa. The FC system is invariably started under a pressure of 1000 hPa. Only after reaching the default operating temperature, the pressure is reduced to the desired test level, and the current profile is initiated.

To prevent irreversible damage caused by excessive membrane dryness (refer to Section 5.1), the test environment pressure is not reduced below 500 hPa. Since the maximum attainable stack current decreases with decreasing pressure, the current profile presented in Figure 4.1 is scaled accordingly. The number of current steps at a lower maximum stack current is also reduced to shorten the test duration. To determine the maximum stack currents, limits are established for the average cell voltage ($U_{cell,avg} \geq 0.5\,V$), as well as the minimum single cell voltage ($U_{cell,min} \geq 0.4\,V$). The pressure-dependent maximum currents are determined through preliminary tests while ensuring compliance with these limits. Table 4.1 lists these maximum

currents along with the respective pressures on the day of polarization curve testing and their corresponding flight level according to the international standard atmosphere [39]. For the sake of simplicity, subsequent references will solely pertain to the pressures listed in column one of Table 4.1.

Test classification	Averaged pressure p_{avg} [hPa]	Altitude [m] according to [39]	Max. stack current I_{max} [A]
1000 hPa	980.35	277.6	180
900 hPa	887.75	1101.4	170
800 hPa	788.73	2063.3	150
700 hPa	690.15	3123.4	125
600 hPa	589.42	4342.1	100
500 hPa	490.69	5712.9	76

Table 4.1: Overview of pressures and maximum stack currents for polarization curves.

4.2.2. Assurance of Steady-State Operating Behavior for Polarization Curves

When creating the polarization curve, it is important that only steady-state operating points are included. Therefore, it is useful to examine a schematic timeline of two consecutive current levels, k, and $k+1$, and their corresponding voltage response. As shown in Figure 4.2, the dwell time t_{dwell} for each current level can be divided into periods of stabilization t_{stab}, data acquisition t_{acq}, and it ends with an offset time t_{offs}.

The stabilization time considers the duration required to achieve a steady-state condition after a current ramp from interval k to interval $k+1$. The data points later used for the polarization curves are determined by averaging all sensor data during the period of data acquisition. Since the boundaries of each interval are identified by an automated change point detection during post-processing (see Section 4.2.3), the boundaries do not coincide with the beginning and end of each current setpoint. Thus, a certain offset time must be taken into account.

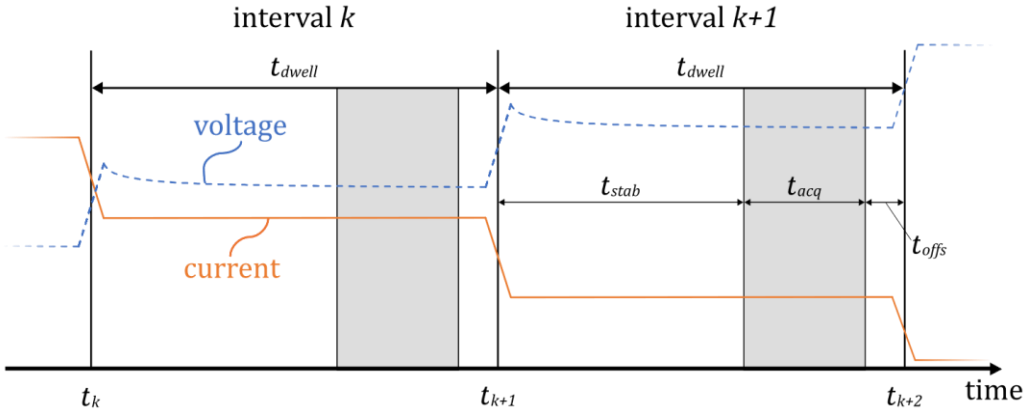

Figure 4.2: Schematic voltage response of two consecutive current levels.

FCTES^{QA} provides recommended minimum parameters for each time step. For the period of data acquisition, a minimum duration of one minute is specified ($t_{acq} > 1$ min). The duration of t_{stab} should be at least twice the time of the period of data acquisition ($t_{stab} \geq 2t_{acq}$) [41].

To record the polarization curve, a data acquisition period of two minutes and a dwell time of 15 minutes are applied. All parameters to ensure steady-state operating conditions are summarized in Table 4.2.

Symbol	Description	Value
t_{dwell}	dwell time for each current setpoint	15 min
t_{acq}	period of data acquisition	2 min
t_{offs}	offset time	35 s
t_{stab}	period of stabilization	12 min 25 s

Table 4.2: Parameters used to ensure steady operating conditions during the polarization curves measurements, cf. Figure 4.2.

4.2.3. Data Post-Processing

Data post-processing is a crucial step in the analysis of large data sets. During the testing process, all sensor data was logged every 0.2 seconds. The resulting measurement data was processed and evaluated using Python, a programming language renowned for its efficiency in handling large data sets. By using Python, data can be rapidly imported, processed, and analyzed. In addition, the Python community provides a wide range of open-source libraries and packages specifically designed for data analysis. These libraries enable the execution of complex analyses while optimizing computational time. For example, for the automatic offline detection of two consecutive current levels, the Python library 'ruptures' was used [43]. Furthermore, the 'Matplotlib' library was utilized for data visualization. This allowed for the inclusion of error bars in the polarization curves, representing the standard deviation of the values averaged throughout the period of data acquisition.

To quantify the impact of the low-pressure environment, a curve fitting analysis was performed using a simplified empirical fuel cell polarization curve model. The 'optimize.curve_fit' function, included in the 'Scipy' package, was utilized for this purpose. This function uses a nonlinear least squares method to fit a function to the data.

4.3. Phase 2: Design and Execution of Parameter Study

The following section will focus on the individual phases of the design and execution of the parameter study introduced in Section 4.1. The pre-experimental planning includes phases a-c, during which pilot experiments are conducted to determine the selection of factors, their corresponding levels and ranges, as well as the response variables. The specific design and the creation of the parameter study (phase d) will be covered in Section 4.3.2. The testing procedure (phase e) and how steady-state operating behavior is ensured during the parameter study, will be discussed in Sections 4.3.3 and 4.3.4. Finally, the post-processing model creation (phase f) will be presented in Section 4.3.5.

4.3.1. Pre-Experimental Planning

a. Recognition and statement of the problem:

The PEMFC system is well-known to deliver significantly less power and has lower efficiency under high-altitude conditions, as also demonstrated in Section 5.1. Besides the lower oxygen partial pressure at high altitudes, the key reason is a too dry membrane resulting from operating the stack with standard control parameters. Thus, the objective of this experimental investigation is to improve the water management of the stack to enhance the net power output of the FC system compared to the net power output recorded with standard control parameters.

b. Specify factors, levels, as well as response variables:

The controllable operational parameters for managing membrane hydration are derived from Equation (2.22), which is presented in the fundamentals section on water management

(cf. Section 2.1.7). If the ambient pressure decreases, the cathode stoichiometry λ_c and/or the stack temperature T must be reduced to maintain constant membrane humidity. To capture the entire operating range of the fuel cell, different current levels must also be taken into account. Additionally, altitude conditions are required to be simulated which leads to the inclusion of the pressure treatment factor.

Apart from the factors mentioned earlier, other parameters like the anode stoichiometry and purging rate play a crucial role in determining the system's performance and especially efficiency. Furthermore, the prevailing environmental conditions affect the cathode inlet temperature and humidity, and the oxygen content should be considered as well in the test setup. To keep the complexity of the parameter study manageable, not all potential design factors will be varied. Therefore, some input variables will be classified as held-constant factors. For the purposes of the present experiment, these factors are not of interest and will either be maintained at specific levels or remain at their default settings. Since the humidity and oxygen content in the chamber can only be indirectly controlled (by high air mass flow rate into the chamber), they are listed as disturbance variables. Compliance with the defined limits will be examined as part of the post-processing. The setpoints or ranges of the held-constant factors are shown in Figure 4.3.

An essential aspect of experimental design is to ensure that the effects of disturbance factors can be differentiated from those of the treatment factors [26 p. 9]. Disturbance factors in the present system are, besides the environmental conditions, variability, hysteresis effects, and potential degradation. Section 4.3.2 will delve into these disturbance factors in more detail, along with principles for minimizing their influence.

Once the treatment factors have been selected, it is necessary to define the ranges within which these factors will be varied, as well as their specific levels. For the pressure factor, the six levels already introduced for the polarization curves are adopted (500 – 1000 hPa). Since the range of attainable currents decreases at lower pressures (see Section 4.2.1), current levels were introduced at intervals of 25 A, except for levels at 65 A and 165 A to improve resolution at 500 hPa and 900 hPa, respectively. This results in a total of nine non-equidistant steps ranging from 25 A to 175 A. However, due to a minimum blower speed, there is also a stoichiometry restriction, so the number of possible parameter combinations per pressure level is significantly lower than without these restrictions (see Appendix B.1).

Since in practice, the cathode stoichiometry is at least two, to avoid concentration losses [18 p. 94], λ_c is varied between 2.0 and 2.8 in a total of five steps.

The temperature range can be approximately determined by analyzing the polarization curve data recorded under ambient conditions with 1000 hPa, but further validation through pilot experiments is necessary.

c. Run pilot experiments:

Besides providing a more precise delineation of the temperature parameter space, pilot experiments can be used to verify the feasibility of the planned factorial level combinations and test the experimental procedure.

Within the pilot experiments, the stack temperature is varied at the already chosen limit levels of pressure, cathode stoichiometry, and stack current. An additional central setting is also introduced for the stack current, resulting in the experimental design outlined in Table 4.3. The temperature ranges derived from the presumed optimal (calculated) humidity range of 60 – 90 %, determined under standard conditions (see Section 5.1.1), are obtained using Equation (2.22). However, these ranges only served as orientation for the pretests.

Test number	Pressure p [hPa]	Stack current I [A]	Stoichiometry λ_c [-]	Assumed stack temperature range [°C]
1	1000	50, 100, 175	2.8	54.6 → 63.3
2			2.0	61.2 → 70.3
3	500	25, 50, 75	2.8	40.9 → 48.8
4			2.0	46.8 → 55.1

Table 4.3: Pilot experiments plan.

As a result of the pilot experiments, the temperature range was defined. Within the parameter study, the target theoretical relative humidities at the cathode outlet are expected to range from 48 % to 95 % (see Section 5.2). For maximum stack currents (cf. Table B.3), the limitation is set to 80 % relative outlet humidity. Considering the potential damage to the Nafion® membrane at temperatures exceeding 80 °C [23 p. 82], the maximum temperature is prudently limited to 70 °C. This yields an overall temperature range of 40 °C to 70 °C, with intervals of 2 °C. Tables specifying the temperature constraints resulting from the calculated relative outlet humidities according to Equation (2.22) can be found in Appendix B.2.

The block diagram illustrated in Figure 4.3 was created for organizing some of the information generated during pre-experimental planning and represents a useful technique in DoE [27 p. 3]. It can be regarded as a summary of this chapter. Subsequently, the D-optimal experimental design can be developed based on this.

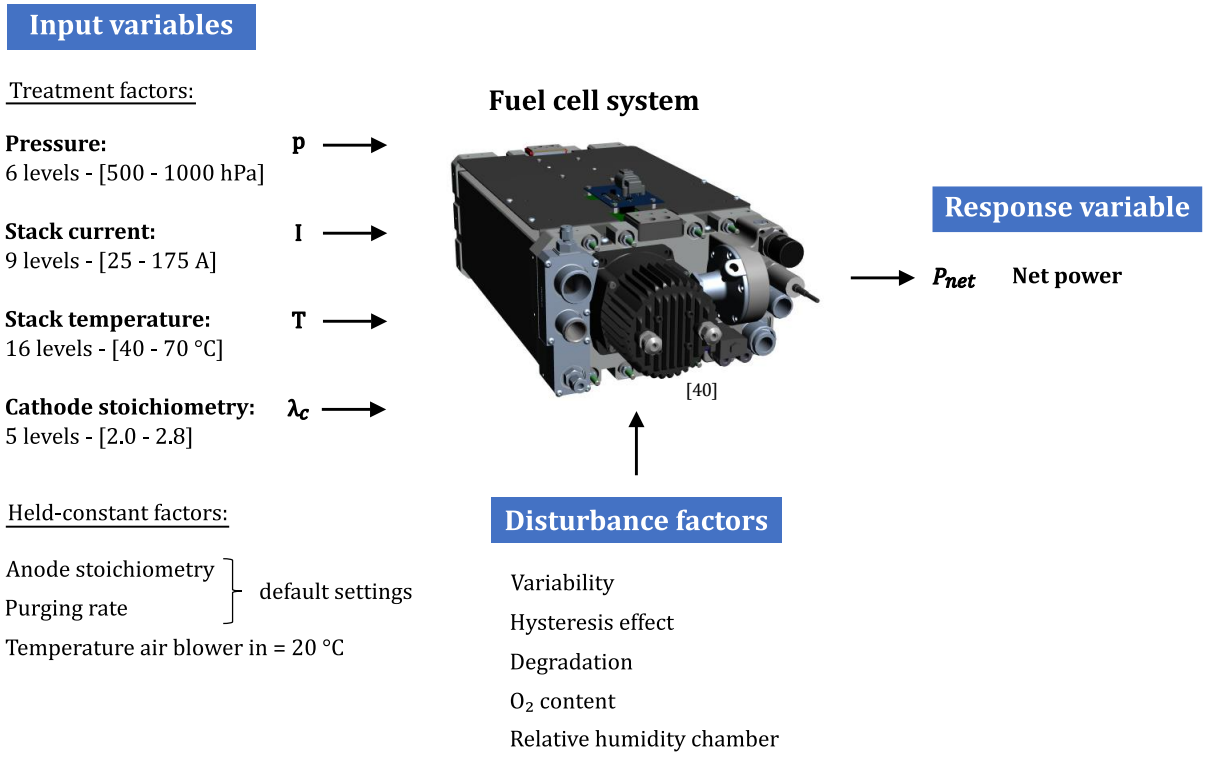

Figure 4.3: Block diagram with input and output variables of the investigated FC system.

4.3.2. Design of the D-Optimal Plan

d. Choice of experimental design:

A full factorial experiment with the chosen treatment factors and their levels, according to Equation (2.23), would result in a total number of experiments of $n_{total} = 4320$ runs. Even with all the introduced constraints of the experimental space, 1213 runs would remain. Considering an average working time of 8 hours, after the approximately two-hour preconditioning procedure, it would be possible to conduct 24 runs with a 15-minute dwell time each per day. This would imply that the parameter study, without any incidents or replication of some points, would take more than 10 working weeks. Additionally, factors such as the potential degradation of the PEMFC device under test, which could affect the accuracy of the results, argue against conducting a full factorial experiment.

As outlined in Section 2.2, given the nature of the system at hand, only an optimal experimental design is feasible. The 'candexch' algorithm implemented in MATLAB is utilized to construct the D-optimal experimental matrix [44]. By specifying an initial design, the results from the experiments already performed in phase 1 are incorporated into the creation of the experimental design. To minimize disturbance factors, only historical measurement data points of phase 1, which meet the following three criteria are considered:

- The slope of the regression line of the averaged cell voltage $\frac{dU_{cell}}{dt} < 10\ \frac{\mu V}{s}$,
- O_2 content > 20 Vol%,
- avoid hysteresis effect, by using values measured with rising current.

Altogether 31 measuring data points are available for the initial design from the measurement series of the polarization curves. To reach a total of approximately 200 data points for the empirical model, Equation (4.1), the desired number of runs in the algorithm is set to 170.

To minimize the disturbances, there are basic principles in DoE, such as replication and randomization. Variability in the data can occur due to measurement errors or natural fluctuations. By replication, i.e. repetition of experimental conditions, the variability can be estimated [26 p. 2]. Therefore, a reference point is introduced, which is always approached after the preconditioning procedure. The reference point represents the center of the normalized parameter space and is therefore referred to as the 0-point ($p = 750$ hPa, $I = 100$ A, $T = 55$ °C, $\lambda_c = 2.4$). In addition to capturing the variability of the experiment, the reference point can also detect degradation, if there is a negative drift.

Adequate randomization of the experiment can compensate for the effects of potential confounding factors [29 p. 31]. However, in the present case, randomization faces the hysteresis effect. Since the hysteresis effect needs to be avoided, the current is strictly increased.

A disadvantage of the D-optimal design is the requirement to specify the model equation prior to the experimental series. The selection algorithm only considers the effects of the chosen model [27 p. 55]. However, using the principle of stepwise regression, it is possible to subsequently simplify the chosen model and retain only the significant effects (see Section 4.3.5). Therefore, initially, a comprehensive approach is chosen for the regression model.

The model Equation (4.1) can be derived using the quadruples presented in Table 4.4, which represent the exponents of the treatment parameters p, I, T, λ_c. The response variable is denoted by y, where k represents the number of model coefficients β_i involved in the experiment. The coefficient β_0 represents the intercept of the empirical model.

$$y = \beta_0 + \sum_{j=1}^{k} \beta_j p^{i_1} I^{i_2} T^{i_3} \lambda_c{}^{i_4} \tag{4.1}$$

As indicated in Table 4.4, main effects up to the fourth order (quartic), interactions up to the third order, and nonlinear interactions are included. This yields a total of 39 model coefficients $\beta_0, \ldots, \beta_{38}$.

Main effects				Interactions			
Linear	Square	Cubic	Quartic	1st order	2nd order	3rd order	Nonlinear
$i_1 i_2 i_3 i_4$	$i_1 i_2 i_3 i_4$	$i_1 i_2 i_3 i_4$	$i_1 i_2 i_3 i_4$	$i_1 i_2 i_3 i_4$	$i_1 i_2 i_3 i_4$	$i_1 i_2 i_3 i_4$	$i_1 i_2 i_3 i_4$
1000	2000	3000	4000	1100	1110	1111	1200
0100	0200	0300	0400	1010	1101		1020
0010	0020	0030	0040	1001	1011		1002
0001	0002	0003	0004	0110	0111		0120
				0101			0102
				0011			0012
							2001
							2010
							2100
							0210
							0021

Table 4.4: Exponents of the design factors β_j in Equation (4.1).

The resulting experimental plan, comprising 178 unique experimental runs, is given in Appendix C. For process-related reasons, the test matrix is divided into seven blocks, with each block containing an increasing current. The seven blocks are each assigned to a test day, whereby one was required for each pressure level except for the pressure of 1000 hPa. Since some data points for 500 hPa and 1000 hPa were already measured during the pilot experiments, they were not tested again. These data points are highlighted in gray in the experimental plan (cf. Table C.1 – Table C.7).

4.3.3. Parameter Study Test Procedures

e. Conduct of the experiment:

Before each test, the stack is pre-conditioned using the startup procedure indicated in green in Figure 4.1 at an ambient pressure of 1000 hPa. Subsequently, the pressure is reduced to 750 hPa to first approach the reference point. Thereafter, the parameter study is carried out.

If certain combinations of factors cannot be realized during the experiments, a new experimental design is created based on a reduced candidate matrix. The restrictions that arose during the testing process are documented in Table B.5 provided in Appendix B.3. As a result, an additional 66 runs were excluded, leading to a finally possible number of runs of $n_{total,final} = 1147$.

4.3.4. Assurance of Steady-State Operation during the Parameter Study

Phase 1 revealed that a dwell time of 15 minutes does not guarantee steady-state behavior (see Figure 5.8). Therefore, for the parameter study, a steady-state detection was implemented in LabView. This steady-state detection calculates the slope of the regression line through the sampling points of the last two minutes, which corresponds to the period of data acquisition. If the slope value of the average cell voltage, i.e., the rate of cell voltage change drops below the predefined steady-state criterion of 10 µV/s, the data point is considered to be steady. Moreover, a minimum stabilization period of 8 minutes must be maintained. Hence, 10 minutes after the

previous parameter change, the steady-state criterion is continuously checked until a steady state is reached and the next parameter change will be performed.

With the implementation of the steady-state detection, the dwell time per measurement point has become variable. This enables time savings in measurement points that exhibit quick attainment of steady-state behavior. For measurement points that do not show steady-state behavior within the previous dwell time of 15 minutes, waiting is now extended until steady-state conditions are achieved. In the event that no indications of a steady-state are observed after 30 minutes, the data point will be invalidated, and a new experimental design will be devised (see Section 4.3.3).

In summary, all the parameters used to ensure steady-state operating points in the parameter study are presented in Table 4.5.

Symbol	Description	Value
t_{dwell}	dwell time for each current setpoint	10 min $\leq t_{dwell} \leq$ 30 min
t_{acq}	period of data acquisition	2 min
t_{offs}	offset time	20 s
t_{stab}	period of stabilization	$\geq$ 8 min
$\frac{dU_{cell}}{dt}$	slope of the regression line of the averaged cell voltage	$\leq 10 \frac{\mu V}{s}$

Table 4.5: Parameters for ensuring steady operating characteristics in the parameter study regarding Figure 4.2.

4.3.5. Response Surface Modeling

f. Statistical analysis of the data:

To perform the statistical analysis of the measurement data, namely the response surface modeling, data from the polarization curves recorded in phase 1, as well as data resulting from the pretests, and data obtained from the parameter study were incorporated. The data were strictly assessed for compliance with the three criteria presented in Section 4.3.2 and, if necessary, discarded. This approach aims to minimize the influence of disturbances. Furthermore, only measurement values within the defined experimental space of the experimental design were included. A normalization procedure was applied to all input variables of the model to ensure that the different coefficients and their corresponding effects in the model are in a comparable range of values. Scaling was performed to range between -1 and 1 based on the respective maximum and minimum levels of the factors.

The Python package 'statsmodels' was used to determine the model parameters [45]. This module allows the estimation of the coefficients by the method of ordinary least squares. Moreover, it conducts a (multiple) analysis of variance (ANOVA), providing a comprehensive summary of the model's statistics, including the estimated coefficients, their standard errors, and other diagnostic information.

The utilization of the D-optimal design necessitated the initial specification of an extensive descriptive model, which was subsequently simplified during the statistical analysis of the measurement data. This simplification was achieved by employing the principle of stepwise regression, particularly sequential backward selection. In this method, the analysis starts with the complete model incorporating all predictors and gradually eliminates those variables that have the least significant impact on the output variable [29 p. 207]. After each predictor is removed, the model is re-estimated. This iterative process continues until only significant effects and interactions remain in the model. The significance of the predictors was evaluated using the 'p-value', which represents the statistical probability of erroneously classifying the effect as true [27 p. 75]. The smaller the probability, the more significant the factor's effect. As threshold for the

significance, a p-value of 20 % was chosen. This value is relatively high compared to common thresholds of 10 %, 5 %, or 1 % [27 p. 127]. However, if there is no overfitting of the model, this only leads to more accurate predictions within the experimental space.

For the evaluation of the regression, in addition to visual inspection (see Section 5.3.2), quantitative validation measures such as the coefficient of determination 'R-squared' (or R^2). were employed. The quantity R^2 is loosely interpreted as the proportion of the variability in the data [28 p. 102]. Clearly, it should fall within the range $0 \leq R^2 \leq 1$, with larger values being more desirable. However, since quite a large number of effects are considered, the adjusted R^2 was specifically used, as it provides a statistical adjustment for the number of factors [28 p. 251].

For a more comprehensive explanation of ANOVA and the associated quality criteria, is referred to [26–29].

5. Results and Discussion

This chapter focuses on the experimental findings and their interpretation. Section 5.1 commences with a discussion on the measurements conducted at sea level, i.e., 1000 hPa. Subsequently, the results of the polarization curves recorded at six different pressure levels ranging from 1000 hPa to 500 hPa during the first phase are presented. Section 5.2 proceeds with the pilot experiments conducted to constrain the temperature parameter range. In Section 5.3, the regression model resulting from the parameter study is introduced, along with a discussion on the different effects of operating parameters on PEMFC performance. The determined optimized control parameters are then showcased. Finally, Section 5.4 provides a comparison of the polarization curves using both standard and optimized parameters for temperature and stoichiometry control.

5.1. Analysis of Polarization Curves with Default Control Parameters

5.1.1. Polarization Curve at 1000 hPa

To get a first impression of the performance of the Hydrogenics HD 10-120 FC system under sea level conditions, the polarization curves recorded at 1000 hPa are presented. Additionally, Figure 5.1 depicts the gross and net power plotted against current density. The net power of the PEMFC system is determined by subtracting the parasitic power demand of the BoP components from the gross power of the fuel cell.

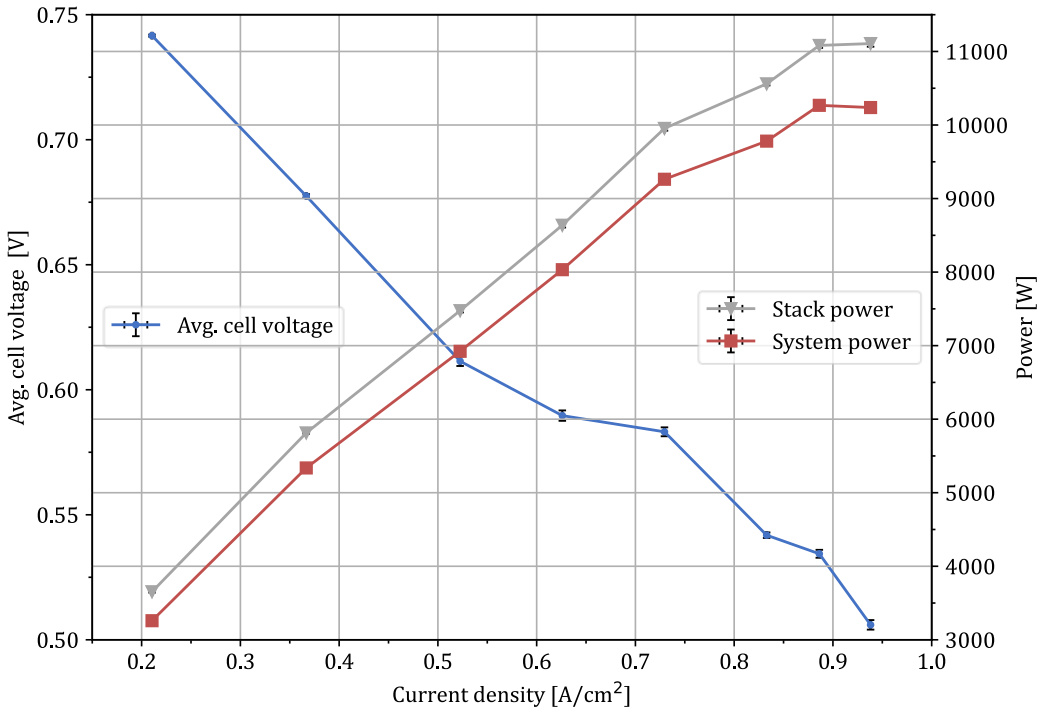

Figure 5.1: Polarization curve with gross and net power output at 1000 hPa.

The stack delivers a maximum gross power of 11107.4 W at a current density of 0.938 A/cm² (182.9 A). The maximum net power of 10267.6 W is achieved at a current density of 0.886 A/cm² (172.8 A). This is due to the disproportionately increasing power demand of the air blowers at higher current densities, as illustrated in Figure 5.2a. There, the power consumption of the BoP components, consisting of the air blower, recirculation pump, and cooling pump, is plotted as a function of current density.

The polarization curve in Figure 5.1 shows an atypical deviation of the measurement points from the expected linear behavior in the region of predominantly ohmic losses. Notably, the measurement points between 0.5 – 0.7 A/cm^2 exhibit a relatively large standard deviation, as evident from the error bars. These findings suggest suboptimal operating parameters.

According to Faraday's law, the reactant flow rate is proportional to the current [see Equation (2.19)]. Therefore, Figure 5.2a shows a typical power curve for a blower, where the power demand increases disproportionately with increasing airflow. The power of the recirculation pump remains nearly constant, as it operates at a fixed rotational speed. As already mentioned in Section 3.5, the stack temperature is controlled by a bypass valve and the cooling pump, running at a constant speed, has a current density-independent power consumption of 101.5 W.

Figure 5.2b displays the relative humidity of the oxygen-depleted air at the cathode outlet (left axis) and the stack temperature (right axis) as a function of the current density. It is evident that within the range of the unusual curvature in the polarization curve, there is a significant jump of 15 % in the cathode outlet humidity, which likewise applies to the membrane humidity. This behavior can be attributed to the default stack temperature setpoints (yellow diamonds), which are linearly increased by 5 °C from 0.5 – 0.7 A/cm^2 (cf. Table 3.3).

In Figure 5.2b, the relative humidity of the cathode outlet ranges from 65 – 85 % under sea level conditions. Consequently, for the pretests for the following parameter study in Section 5.2, the temperature range to be investigated was defined using a cathode outlet humidity between 60 % and 90 % (cf. Section 4.3.1).

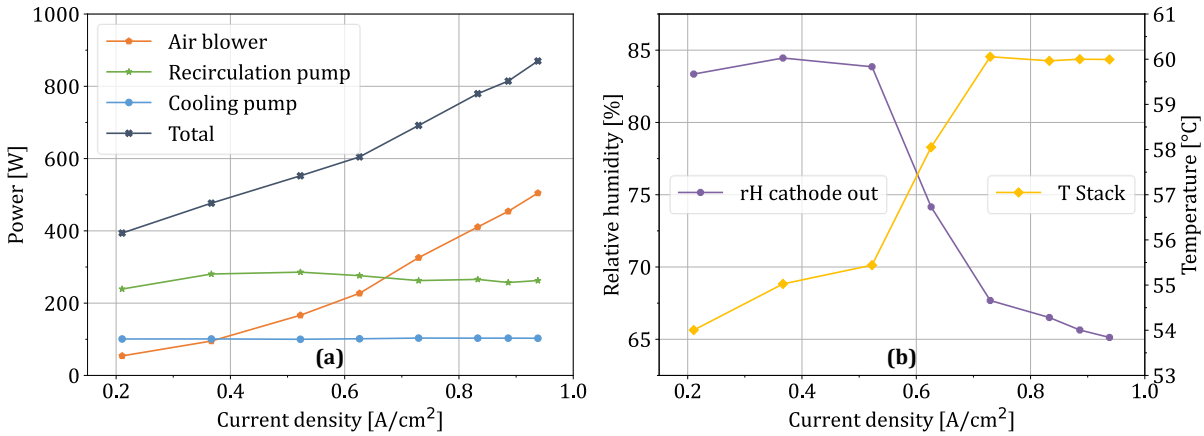

Figure 5.2: Power consumption of the BoP components (a), and the relative humidity of the cathode outlet, stack temperature (b) versus the current density at 1000 hPa.

In Figure 5.3 shows the required stoichiometry output from the PDC (orange pentagons), as well as three other stoichiometries calculated from the sensor values. Significant deviations from the required values were observed during the calculation of the cathode stoichiometry (green stars) according to Equation (2.21). The analysis revealed that the deviations could be attributed to the externally powered BOP components, namely the air blower and the recirculation pump. In the internal calculation of the required cathode stoichiometry, the controller of the PEMFC system takes into account the parasitic current of the BoP components. However, in the case of the present test setup where these components are externally powered, this consideration of the parasitic current in the cathode stoichiometry calculation becomes irrelevant. To verify this, the stoichiometry was calculated using a corrected current value, obtained by subtracting the measured BoP current from the stack current. As can be seen in Figure 5.3, these values, shown as blue points, now exhibit significantly lower deviations from the required stoichiometry.

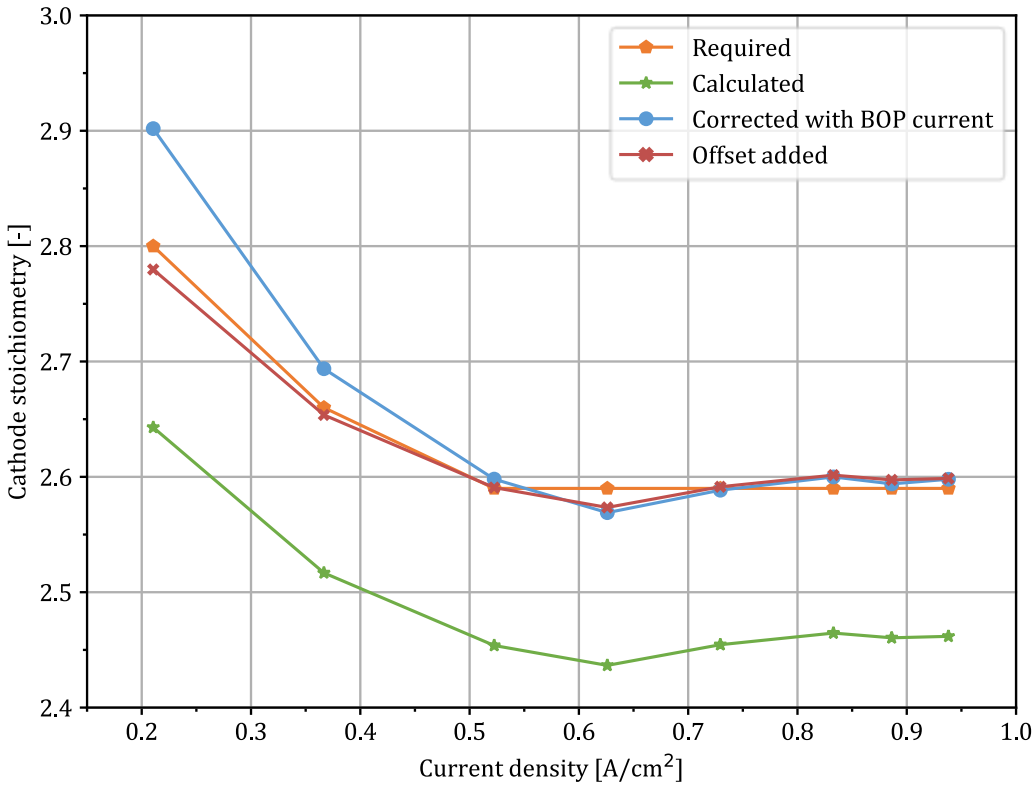

Figure 5.3: Required and calculated cathode stoichiometry according to Equation (2.21) versus current density at 1000 hPa.

To avoid the deviation of the cathode stoichiometry with externally powered BoP components, an offset of 0.163 was determined across all test campaigns, which needs to be added to the desired value of the cathode stoichiometry setpoint. As depicted in Figure 5.3, the corrected stoichiometry values (red crosses) closely align with the required values. Since the PDC can only process stoichiometry values with one decimal place, an offset of 0.036 remains. Therefore, the subsequent parameter study will focus solely on the calculated cathode stoichiometry values.

Additionally, it was observed that the air blower has a minimum rotational speed, leading to a minimum air mass flow rate. As a result, the required stoichiometry cannot be attained at low current densities. Since the mass flow rate is dependent on density, and consequently pressure-dependent, the pressure-current constraints presented in Appendix B.1.

5.1.2. Polarization Curves under Low-Pressure Conditions

In Figure 5.4a, the polarization curves recorded during the first phase at six different pressure levels are presented. The FC system was operated using the standard control parameters for stack temperature and cathode stoichiometry recommended by the manufacturer. The resulting polarization curves demonstrate a pronounced sensitivity to environmental pressure. While only moderate pressure dependency is observed at low current densities, the cell voltage values decrease significantly with higher current densities. A comparison between the polarization curves recorded at 500 hPa and 1000 hPa reveals a reduction in cell voltage of only 10.5 % at 0.2 A/cm², whereas a decrease of 25.7 % is observed at 0.4 A/cm². Clearly, lower total pressure leads to a downward shift in the polarization curve toward lower voltage performance and an increase in the slope of the curve. Additionally, Figure 5.4a reveals a substantial reduction in achievable absolute current densities, while maintaining a minimum average cell voltage of 0.5 V, as the pressure decreases. When comparing the percentage differences in current density for constant average cell voltages, it is evident that they are in similar magnitudes. For instance, at

around 0.75 V, a current density decreases of 58 % can be observed, while at around 0.5 V, a decrease of 53 % can be measured when comparing the polarization curves for 500 hPa and 1000 hPa ambient pressure.

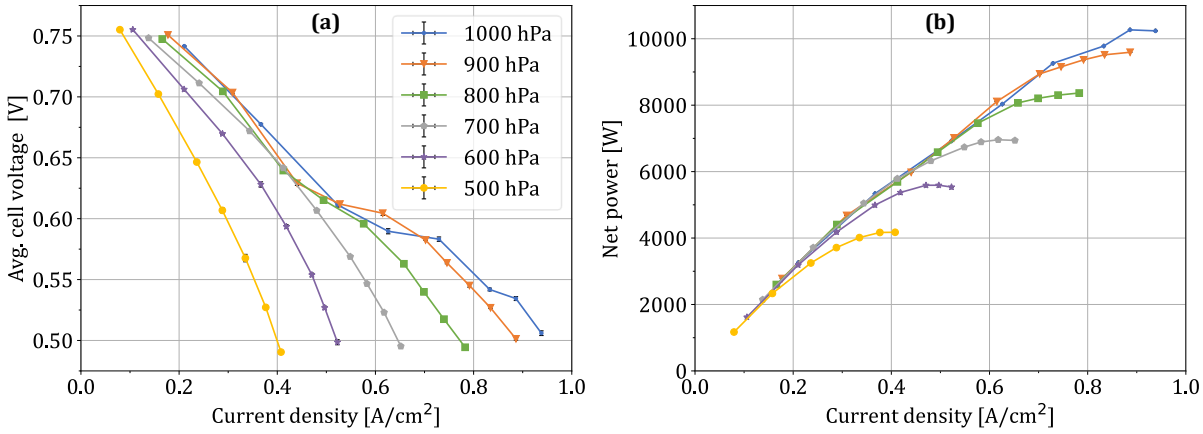

Figure 5.4: Polarization curves (a) and net power characteristics (b) under different low-pressure conditions.

The resulting net power of the PEMFC system is shown in Figure 5.4b. At a pressure of 500 hPa, equivalent to an altitude of approximately 5700 m [39], the maximum power output reaches only 40.7 % of the maximum power at 1000 hPa. Table 5.1 provides the maximum possible gross and net power for different pressure levels. Additionally, it presents the percentage deviations from the gross and net power at 1000 hPa. It is noteworthy that the power losses increase disproportionately towards lower pressures.

Test classification	Avg. pressure	Max. gross power			Max. net power		
	p_{avg} [hPa]	$P_{gross,max}$ [W]	at i [A/cm²]	$\Delta P_{gross,max}$ [%]	$P_{net,max}$ [W]	at i [A/cm²]	$\Delta P_{net,max}$ [%]
1000 hPa	980.35	11107.4	0.938	0	10237.5	0.886	0
900 hPa	887.75	10397.5	0.886	6.4	9592.9	0.886	6.6
800 hPa	788.73	9055.1	0.783	18.5	8366.2	0.783	18.5
700 hPa	690.15	7558.9	0.618	31.9	6959.5	0.618	32.2
600 hPa	589.42	6122.6	0.497	44.9	5590.2	0.497	45.6
500 hPa	490.69	4678.5	0.408	57.9	4173.8	0.408	59.3

Table 5.1: Maximum possible gross and net power for different pressure levels.

The power losses are primarily attributed to the decreasing total pressure and the consequent decrease in oxygen partial pressure. The decreasing total pressure particularly affects the diffusion rate of the reactant gases, resulting in a decrease in the available reactants at the catalyst layer [12]. The decrease in oxygen partial pressure results in a reduction in the oxygen supply, as there are fewer oxygen molecules available for the electrochemical reactions of the fuel cell.

Another non-negligible portion of the losses is due to the membrane humidity. As shown in Figure 5.5, the relative humidity at the cathode outlet and, thus, the membrane humidity decreases under low-pressure conditions. At a current density of 0.4 A/cm², the relative humidity at the cathode outlet drops from nearly 85 % to about 47.5 % between 1000 hPa and 500 hPa. The decrease in relative humidity can be attributed to the constant saturation partial pressure, as the stack temperature remains at default values across all pressure levels. However, the water vapor partial pressure decreases together with the ambient pressure, leading to a lower relative

humidity and causing a drying effect. A shortage in membrane humidity (drying-out) results in reduced proton conductivity and lower cell performance [18 p. 92]. Since the relative humidity dropped below 50 % at 500 hPa, further pressure reduction was avoided to prevent permanent membrane damage. The relatively high humidity values observed at 900 hPa in the range above 0.6 A/cm^2 are likely due to droplet formation on the rH sensor.

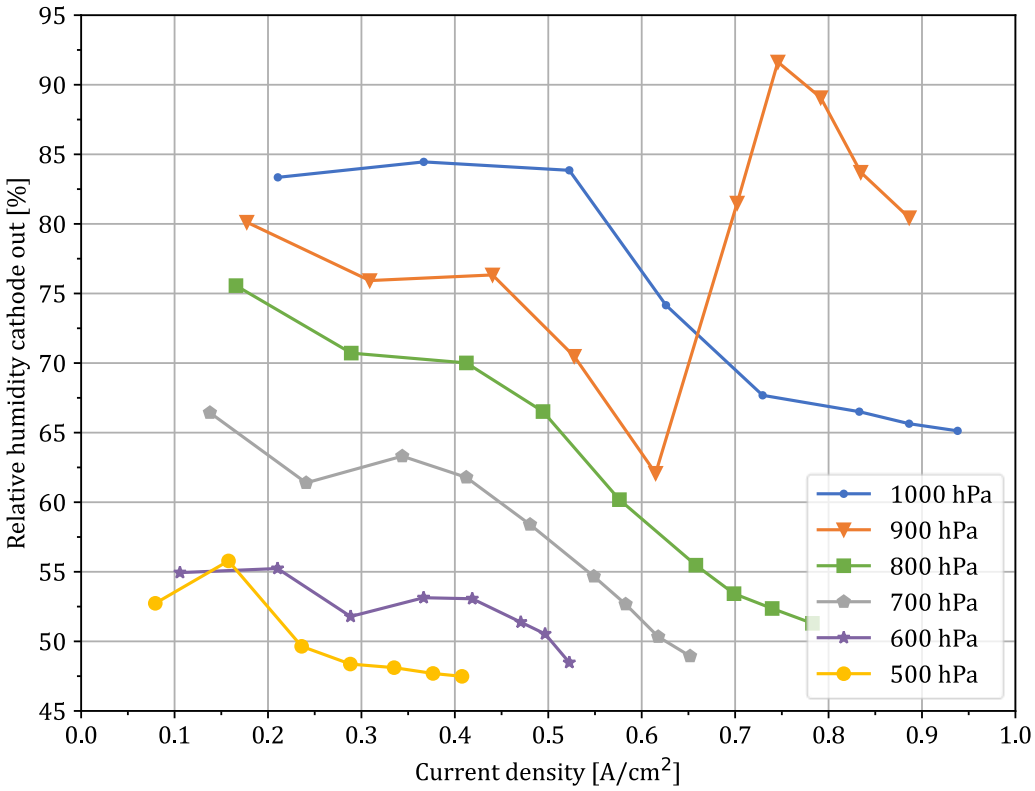

Figure 5.5: Comparison of cathode outlet humidities for different pressure conditions.

In the comparison of percentage deviations of gross and net power in Table 5.1, it is noticeable that the net power deviation becomes slightly larger towards lower pressures. This can be attributed to an increased power demand for the BoP components under low-pressure conditions.

As shown in Figure 5.6a, the power demand of the air blower increases significantly for a fixed current density at reduced pressure. At 500 hPa and a current density of 0.4 A/cm^2, the blower consumes approximately 2.9 times more power compared to the same operating point at 1000 hPa. The blower is regulated based on the stoichiometry value, which requires a specific mass flow rate. Consequently, at higher altitudes where the air density is lower, the blower needs to maintain a higher volumetric flow rate to achieve the same mass flow rate as at sea level. This higher flow rate means that the blower has to exert more work to move the same air mass, resulting in higher power consumption. Furthermore, the blower is not designed for operation under high-altitude conditions, causing a significant decrease in its efficiency.

Another reason for the increased power consumption of the air blower is the mass flow meter used on the cathode side, i.e., a hot wire anemometer device. This device, widely used in the automotive industry, operates based on the cooling effect caused by the gas flow on a thin heated wire [46 p. 373]. The heat loss is directly proportional to the air mass flow. When using a hot wire mass flow sensor under conditions of reduced air density, such as at high altitudes, the measurement accuracy is affected. This is because the cooling effect on the wire decreases as the air density decreases, leading to lower signal output as feedback signal. Consequently, the air blower generates an overestimated true mass flow, leading to additional power consumption. To

compensate for this effect, it may be necessary to adjust the sensor calibration or use correction factors based on the air density. Furthermore, an alternative sensor based on a different measurement principle could be utilized. This was identified through a slightly elevated pressure difference between the cathode inlet and the chamber pressure at lower pressure levels. At 500 hPa and 0.4 A/cm^2, the pressure difference amounts to approximately 20 hPa compared to 1000 hPa. The increased true mass flow results in higher friction losses across the fuel cell, leading to an increase in the pressure differential.

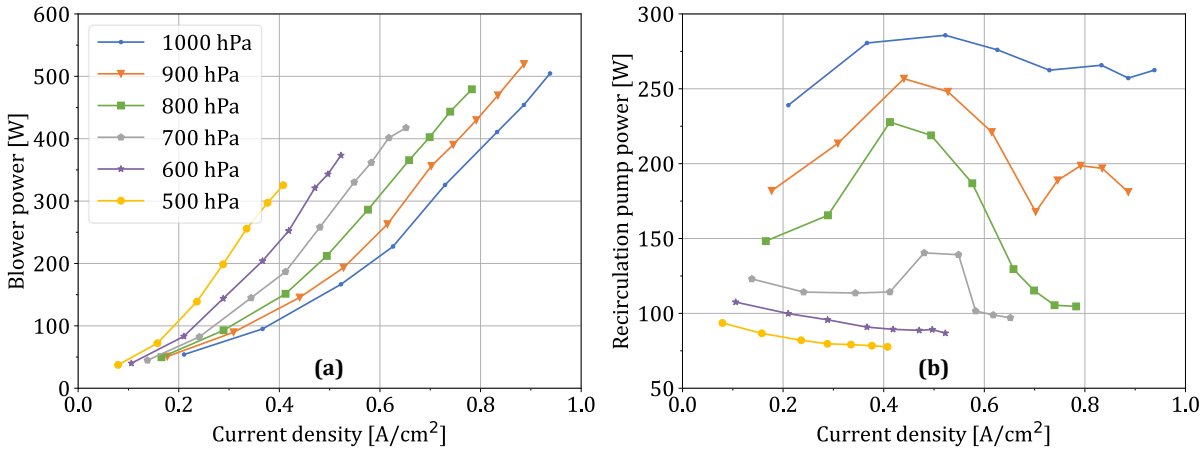

Figure 5.6: Power consumption of the air blower (a) and the recirculation pump (b) versus the current density under different low-pressure conditions.

The power consumption of the recirculation pump is presented in Figure 5.6b. Interestingly, the power demand decreases significantly as the pressure decreases. This is attributed to the control at a constant rotational speed, which requires less power under high-altitude conditions with lower air density. Additionally, the moisture content on the anode side, as well as the hydrogen content affect the density and thus the power demand of the recirculation pump. When comparing the cathode outlet humidities shown in Figure 5.5 with the power curves in Figure 5.6b, it is particularly evident for the curves from 800 hPa to 1000 hPa that the decline in power curves in the higher current density range shows a similar pattern. A lower humidity content results in a higher hydrogen content and, therefore, a lower density, leading to reduced power requirements. However, since the hydrogen content was not measured during this test campaign, the behavior of the recirculation pump power cannot be fully explained.

However, it is indisputable that controlling at a constant rotational speed under low pressure leads to a reduced anode-side mass recirculation. This could also be another factor contributing to the inferior performance of the fuel cell under low pressure, as it may lead to local fuel starvation. Additionally, it has a negative impact on homogeneous anode humidification. To avoid this, a mass flow-controlled regulation would need to be implemented for the recirculation pump of fuel cell system for aviation application. However, this would significantly increase the power demand, similar to the air blower under low pressure. Further investigations are necessary to determine whether these resulting negative effects on net power can be compensated by higher fuel cell performance.

When considering the system efficiency related to the lower heating value $\eta_{Net,LHV}$ it became evident that the mass flow meter (MFM) for the hydrogen supply provided nonsensical values. This was obvious as the fuel utilization coefficient η_{fuel} assumed values exceeding 100 % across the entire range of current density. However, since hydrogen consumption cannot surpass the amount supplied, the MFM measurements must be erroneous. It is presumed that this is due to an incorrect calibration of the MFM. Unfortunately, this error could not be rectified within the scope

of this thesis. Nevertheless, to investigate the effects of low pressures on system efficiency, the current-dependent behavior of the fuel utilization coefficient was adjusted. Since 95 % is a good estimate for η_{fuel} [18 p. 36], the difference between the average value of the measured fuel utilization coefficient across all pressure levels ($\eta_{fuel} = 101.65$ %) was calculated and subtracted from each individual measurement value. By applying this correction, the system efficiency was calculated using Equation (2.16). Figure 5.7 illustrates the relationship between system efficiency, based on the lower heating value, and the net power output. Generally, as the net power output approaches the maximum achievable power for a given pressure level, the system efficiency decreases disproportionately. Surprisingly, for the pressure levels of 700 hPa to 1000 hPa, the PEMFC system exhibits a similar efficiency trend up to approximately 6000 W net power. This is attributed to the previously mentioned atypical nonlinear trend of the polarization curves for the pressure levels of 800 – 1000 hPa. However, this pattern is not reproduced at the two lower pressure levels, 500 hPa and 600 hPa, where the system efficiency decreases significantly already at low net power values. For instance, at a net output of 4000 W, an absolute drop in efficiency of 10.4 % between 1000 hPa and 500 hPa was determined. This corresponds to a relative decrease of over 21 %. Overall, these findings demonstrate that system efficiency is also strongly affected by low-pressure conditions, which will have a significant impact on factors such as required tank size or the aircraft's range.

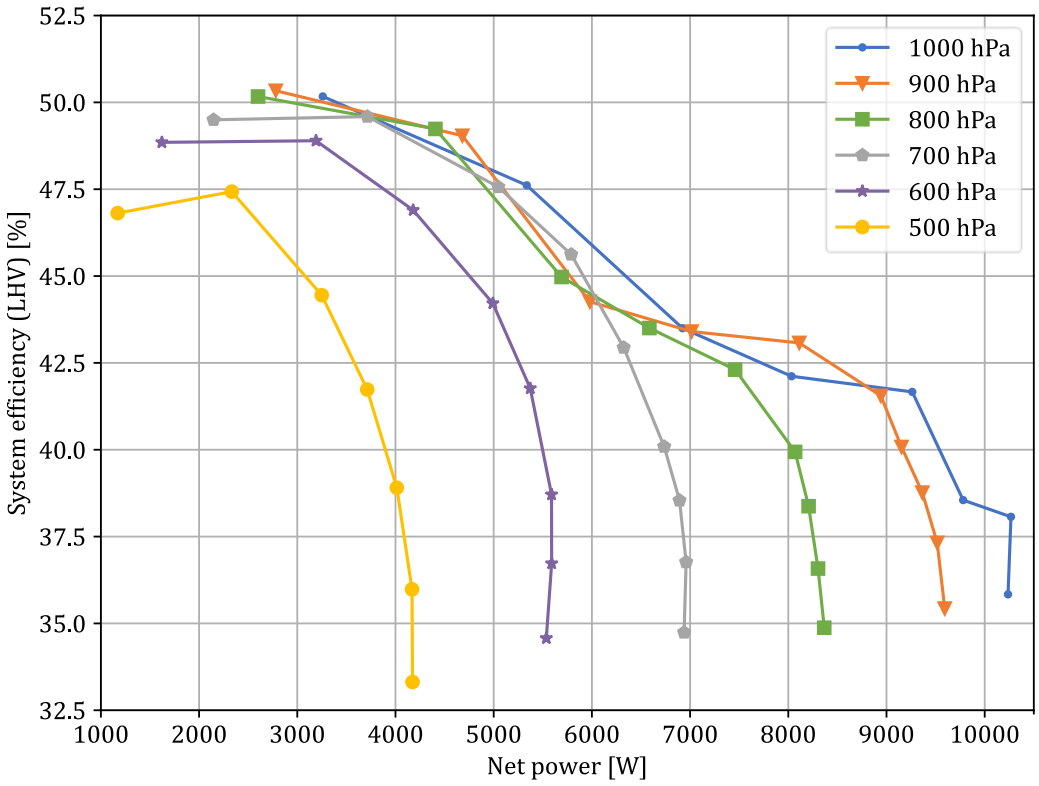

Figure 5.7: System efficiency referring to the LHV in relation to the net power under different low-pressure conditions.

As evident in Figure 5.4a, the polarization curves for 800 hPa and 900 hPa also exhibit an unusual nonlinear trend in the region of predominantly ohmic losses. As mentioned earlier for the polarization curve at 1000 hPa (see Section 5.1.1), this suggests suboptimal operating conditions in this current density range. During the post-processing phase, it was observed that the average cell voltage response for certain current setpoints did not exhibit a steady state even after a 15-minute dwell time. Figure 5.8 shows an example of the voltage response during the acquisition of the polarization curve at 1000 hPa. The red lines, represent the regression lines through the

corresponding red measurement points that were used for averaging within the period of data acquisition. As depicted in Figure 5.8, the measurement points at 18000 s and 19000 s do not demonstrate steady states, which is reflected in the large slope values of -44.1 and 16.8 µV/s, respectively. Therefore, a steady-state criterion was subsequently introduced. If the slope of the regression line is below 10 µV/s, the measurement point is considered to be steady. If it exceeds the threshold, the data point will be discarded.

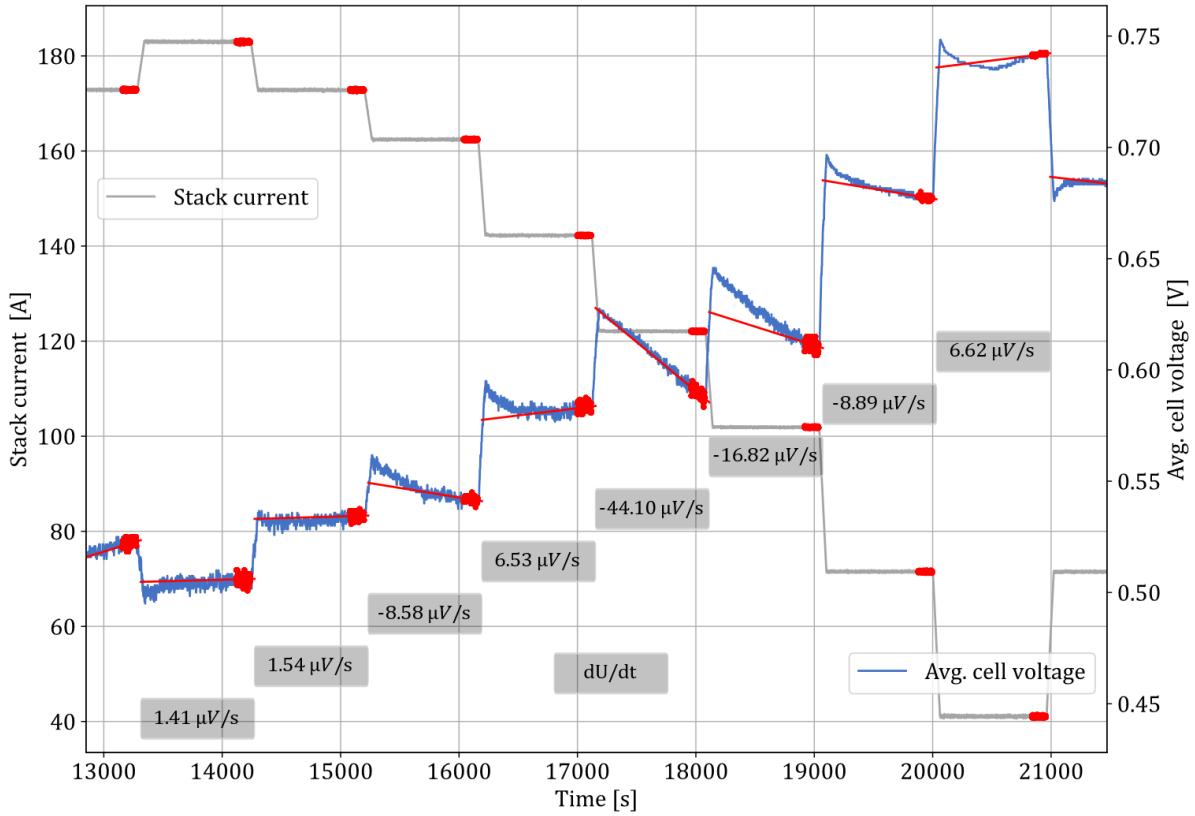

Figure 5.8: Voltage response for current setpoints of polarization curve at 1000 hPa.

It is noteworthy that the points that do not meet the steady-state criterion are primarily causing the deviations from the linear trend in the region of predominantly ohmic losses of the polarization curve. This observation provides additional evidence that these measurement points do not correspond to optimal operating conditions.

Since a steady state was not achieved for some measurement points even after a dwell time of 15 minutes, real-time monitoring of average cell voltage rate of change would be beneficial for the parameter study. Additionally, it was evident that more favorable operating conditions led to a considerably faster attainment of a steady state.

5.1.3. Low-Pressure Effects on Voltage Losses

To quantify the effects of different kinds of voltage losses under low-pressure conditions, a curve fitting analysis was conducted using a simplified empirical fuel cell polarization curve model [Equation (5.1)]. The shape of the polarization curves in Figure 5.9 indicates that the fuel cell was operating in the transition region between the middle- and high-current regimes, where ohmic losses and concentration losses are dominant.

The empirical model equation is based on the well-known equation for calculating the cell voltage [18 p. 57], but neglects activation losses, as well as internal currents and crossover losses:

$$U_{cell} = E_{fit} - \Delta U_{ohm} - \Delta U_{conc} = E_{fit} - R_{fit} i - B_{fit} \ln\left(\frac{i_{L,fit}}{i_{L,fit} - i}\right), \qquad (5.1)$$

where E_{fit}: is the fitting parameter for the y-intercept,
R_{fit}: is the fitting parameter for the ohmic resistance,
B_{fit}: is the fitting parameter for mass-transfere loss,
$i_{L,fit}$: is the fitting parameter for the limiting current density.

Due to the limited number of data points remaining after applying the steady-state criterion ($dU/dt \leq 10$ µV/s), it is not feasible to fit a more accurate model, such as the widely used one by Kim et al. [47], to the available data. Moreover, measurements were not conducted at very low current densities (close to OCV), where the effect of hydrogen crossover and internal current losses becomes prominent [15 p. 54].

However, as the primary aim is to observe trends, the simplified empirical model can be applied, specifically to represent the range of moderate to high current densities in a fuel cell polarization curve.

Figure 5.9 illustrates the fitted polarization curves represented as dot-dashed lines for all six pressure levels. The associated fitting parameters are listed in Table 5.2. Despite the introduction of the steady-state criterion, the data points for 800 hPa and 1000 hPa still have one point respectively with a significant deviation from the linear trend in the ohmic range (between 0.35 – 0.45 A/cm^2). Since the model assumes the typical linear trend in this region the curve fitting results did not yield consistent trends for these two fitted polarization curves in comparison to the other curves. Therefore, both curves and coefficients are not further considered. However, for the sake of completeness, they can still be found in Figure 5.9 and Table 5.2.

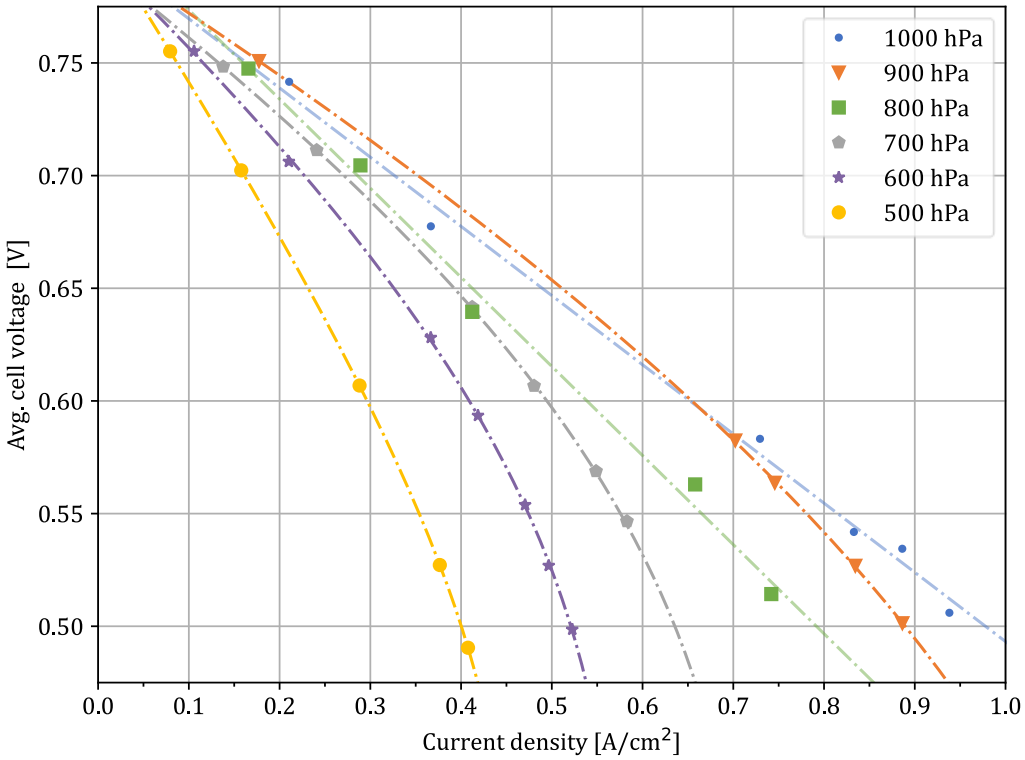

Figure 5.9: Comparison of fitted polarization curves.

The first coefficient, E_{fit}, does not show any noticeable trend across the various pressure levels, as seen in Table 5.2. It is important to emphasize that E_{fit} is only a fitting parameter and does not correspond to the open-circuit voltage (OCV) or the reversible cell potential of the fuel cell. Hence, it is not directly linked to any specific physico-chemical properties.

When examining the remaining coefficients, trends can be observed for the four pressure levels. To highlight these trends, conditional formatting was used. The ohmic resistance of 900 hPa remains in a reasonable range, between 0.1 and 0.2 Ω cm^2 [15 p. 55]. The lower the pressure, the greater the R_{fit} coefficient becomes. At 500 hPa, the coefficient for ohmic resistances increases by a factor of 3.3 compared to 900 hPa. Since the acquisition of polarization curves was performed with the same temperature control, R_{fit} in the intermediate region of the current density is primarily dependent on membrane resistance and pressure.

Values above 0.2 Ω cm^2 suggest significant dehydration of the membrane [15 p. 55], as already identified in Section 5.1.2. However, a comprehensive differentiation between the influence of pressure and membrane humidity on the ohmic losses cannot be resolved at the current stage.

As expected, the limiting current density coefficient decreases with decreasing pressure. The fitting coefficient $i_{L,fit}$ for 500 hPa is only about 40 % of the value at 900 hPa. This can be attributed to the lower partial pressure of oxygen. During operation, the partial pressure of oxygen decreases in the electrode region as a portion of the oxygen is consumed there. However, if the oxygen concentration is already reduced due to the lower pressure prevailing at higher altitudes, the condition arises at lower current densities where the decrease in concentration equals the supply rate. Due to the smaller coefficients $i_{L,fit}$ at low-pressure operation, the value of the natural logarithm [cf. Equation (5.1)] becomes large even at lower current densities, resulting in a decrease in the fitting coefficient B_{fit} with decreasing pressure. Overall, the influence of concentration losses significantly increases under low-pressure conditions. For example, calculating the concentration losses at 500 hPa for a current density of 0.4 A/cm^2 yields a voltage loss of 0.208 V. At 900 hPa, the value for the same current density is only 0.109 V.

	500 hPa	600 hPa	700 hPa	800 hPa	900 hPa	1000 hPa
E_{fit} $[V]$	0.807	0.798	0.794	0.813	0.799	0.800
R_{fit} $[\Omega\ cm^2]$	0.540	0.275	0.209	0.396	0.165	0.307
B_{fit} $[V]$	0.105	0.166	0.189	4.79E-10	0.283	8.12E-10
$i_{L,fit}$ $[A/cm^2]$	0.464	0.590	0.739	3.000	1.254	2.741

Table 5.2: Values of the fitting parameters for the simplified polarization curve model according to Equation (5.1).

Overall, phase one demonstrated that the operation of the PEMFC system with standard control parameters is limited at high altitudes due to issues related to self-humidification, i.e., water management.

5.2. Pilot Experiments Results

The pilot experiments enabled a more refined delimitation of the temperature parameter space. Figure 5.10 presents the measured values of the net power output obtained during the pilot experiments plotted against the relative cathode outlet humidity calculated according to Equation (2.22). Figure 5.10a illustrates the data for 1000 hPa, while Figure 5.10b represents the data for 500 hPa.

The calculated relative humidity values (rH_{out}), particularly for higher rH_{out} values, exhibit a certain offset compared to the actual measured values for the relative humidity. However, since Equation (2.22) is used to determine the temperature values for the parameter space, these were

employed for constraining the experimental space and are therefore plotted in Figure 5.10. In general, the highest net power outputs are observed for parameter combinations with rH_{out} values ranging from 48 – 95 %. This is evident from the fact that the measured net power maxima for each current level lie within the aforementioned calculated cathode outlet rH_{out} values, as depicted in Figure 5.10a and b. However, for maximum stack currents, outlet rH_{out} values above 80 % could not be achieved due to flooding. Therefore, the minimum temperature corresponding to 80 % rH_{out} values is to be calculated for maximum stack currents. The resulting limitations are schematically depicted by the gray shaded areas in Figure 5.10a and b.

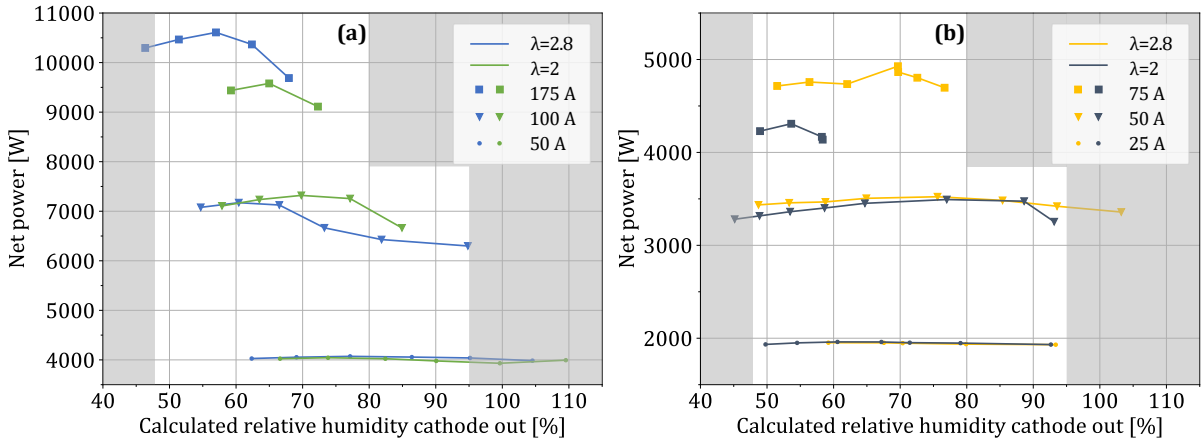

Figure 5.10: Net power versus calculated relative humidity at the cathode outlet for 1000 hPa (a) and 500 hPa (b).

Based on the pilot experiments, first preliminary findings regarding the influence of stack temperature and cathode stoichiometry on the net power output, as well as the humidity management of the fuel cell were derived. A detailed discussion of these findings can be found in the next section.

5.3. Results of the Parameter Study

The following section presents and discusses the results of the parameter study. First, in Section 5.3.1, the results of the regression analysis and the associated model quality are presented. Subsequently, Section 5.3.2 focuses on the effects of operating parameters on PEMFC system performance. This includes an examination of the influence of stack temperature and cathode stoichiometry on the net power output at different current densities for both 1000 hPa and 500 hPa. Additionally, the influence of the pressure is studied in detail. Finally, in Section 5.4 the results of the polarization curves obtained with optimized control parameters for 500 hPa and 1000 hPa are presented for the purpose of validating the model equation.

5.3.1. Regression Results

After verifying compliance with the criteria outlined in Section 4.3.3, Table 4.5, a total of 274 points were available for the regression of the model coefficients [Equation (4.1)]. Among these points were 7 replicate measurements of the reference point. Sequential backward selection was employed for the net power as response variable, resulting in a total of nine iterations, i.e., nine coefficients ($p^3, pIT\lambda, \lambda^4, T^4, \lambda^3, IT, p^2\lambda,\ p^4, I^4$) were eliminated until the predefined threshold of 0.2 for the p-value was surpassed. This denotes that the effects do not have significance for the model.

The largest remaining p-value is 0.161 and corresponds to the nonlinear interaction between the pressure and the temperature (p^2T). The graphical assessment of the regression model did not

reveal any evidence of overfitting (see Section 5.3.2), hence further sequential backward selection was not necessary.

Utilizing the analysis of variance in the Python package 'statsmodels' (see Section 4.3.5), global measures were employed to assess model fit. The adjusted coefficient of determination R^2, yielding a value of 0.994, substantiates the excellent compatibility of the model with the measured data. The F-statistic, evaluating the impact of an independent variable on a dependent variable, exhibits a value of 1404, indicating the statistical significance of the overall model [28 p. 103]. Moreover, the associated probability of $8.08 \cdot 10^{-255}$ (<0.05) further corroborates this conclusion. In addition, the standard errors assumed that the covariance matrix of the errors was correctly specified.

The regression coefficients for the 30 remaining numerical values are listed in Table 5.3. The coefficients that were eliminated through sequential backward selection can be determined by examining the coefficients omitted in Table 5.3. A detailed summary of the results generated by 'statsmodels' for both the complete and the reduced model can be found in Appendix D.

Coefficient	Effect	Value
β_0	Intercept	6610.049
β_1	p	512.226
β_2	I	3056.556
β_3	T	495.090
β_4	λ_c	164.951
β_5	p^2	-1091.292
β_6	I^2	-1229.539
β_7	T^2	-2493.237
β_8	${\lambda_c}^2$	-156.750
β_{10}	I^3	278.437
β_{11}	T^3	778.855
β_{17}	pI	937.503
β_{18}	pT	2802.079
β_{19}	$p\lambda_c$	297.478
β_{21}	$I\lambda_c$	144.174

Coefficient	Effect	Value
β_{22}	$T\lambda_c$	-661.701
β_{23}	pIT	2516.839
β_{24}	$pI\lambda_c$	162.001
β_{25}	$pT\lambda_c$	-544.481
β_{26}	$IT\lambda_c$	-327.749
β_{28}	pI^2	482.784
β_{29}	pT^2	-1218.430
β_{31}	IT^2	-1931.795
β_{32}	$I{\lambda_c}^2$	-136.048
β_{33}	$T{\lambda_c}^2$	167.248
β_{34}	$p^2\lambda_c$	127.086
β_{35}	p^2T	389.545
β_{36}	p^2I	-1058.458
β_{37}	I^2T	-584.091
β_{38}	$T^2\lambda_c$	482.039

Table 5.3: Numerical regression coefficients for the net power as response variable.

The values listed in Table 5.4 were obtained during the acquisition of the reference point (0-point). With a standard deviation of the net power output of 32.2 W, which corresponds to a percentage deviation of less than 0.5 %, the reproducibility of the measurement data recorded in the seven test blocks is ensured. Furthermore, the data show no declining power trend, indicating no signs of degradation throughout the measurement campaign.

Test block	Avg. cell voltage[V]	Cathode outlet rH [%]	Net power [W]
1	0,597	70,5	6801.3
2	0,597	69,5	6795.0
3	0,601	71,8	6846.7
4	0,601	68,0	6875.5
5	0,601	68,3	6878.9
6	0,597	67,8	6830.5
7	0,594	68,1	6793.2

Table 5.4: Results of reference point measurements at $p = 750$ hPa, $I = 100$ A, $T = 55$ °C, $\lambda_c = 2.4$.

5.3.2. Effect of the Operating Parameters on the PEMFC Performance

For the graphical assessment of the regression model, as well as for the identification of the effects of operating parameters on the PEMFC system performance, various figures are presented below. Some diagrams display measurement points and their corresponding model curves, while others solely present the regression model for improved clarity. As a 5-dimensional parameter space is being represented, comprising pressure, stack current, temperature, cathode stoichiometry, and the resulting net power, it is necessary to hold certain dimensions constant for graphical evaluation.

Effect of stack temperature and cathode stoichiometry at 1000 hPa:

Figure 5.11a shows the net power output of three current levels plotted versus the stack temperature at 979 hPa with a stochiometric ratio of 1.98. The selected current levels correspond to lower, middle, and upper settings within the parameter range allowed by the prevailing pressure. Similarly, Figure 5.11b displays the net power output for the same three current levels as a function of stack temperature, but with a stoichiometric ratio of 2.74 under the same pressure conditions. The deviations of the measured data from the prescribed input variables arose from the experimental setup. To ensure a close alignment between the regression curves and the measured data points, the relevant input parameters for the model equation were determined based on the averaged values of the corresponding data points.

In general, the regression curves of Figure 5.11a and b exhibit a good fit to the measured data, as visually assessed. Due to the imposed maximum temperature of 70 °C, the smaller investigated temperature range of only 10 °C in Figure 5.11a compared to about 14 °C in Figure 5.11b is noticeable. The difference in absolute temperatures between the two plots is attributable to the variation in stoichiometric ratio causing a temperature shift to account for similar cathode outlet humidities [according to Equation (2.22)]. Additionally, it is noticeable that the influence of stack temperature becomes more significant at higher current densities. This is evident on the one hand by the curvature of the regression curves, but also by the deviations of net power values from the measurements within each current level. In Figure 5.11a, the standard deviation of the measured values is about 41 W for a current density of 0.26 A/cm^2, whereas it is already 265 W for 0.52 A/cm^2 and 540 W for 0.91 A/cm^2. This trend also applies to the measured values shown in Figure 5.11b, which correspond to a higher stoichiometry.

It is also noticeable that the maximum achievable net power outputs are higher for a stoichiometry of 2.74 compared to the lower stoichiometry of 1.98. For the higher current density of 0.91 A/cm^2, the regression curve yields a maximum net power value of 9696 W for $\lambda_c = 1.98$ and 10031 W for $\lambda_c = 2.74$, resulting in a 3.5 % increase. However, this stoichiometry effect is less significant for lower current densities. At 0.26 A/cm^2, the model's maximum net power is 4087 W for $\lambda_c = 1.98$ and 4107 W for $\lambda_c = 2.74$. This corresponds to a negligible increase of less than 0.5 %.

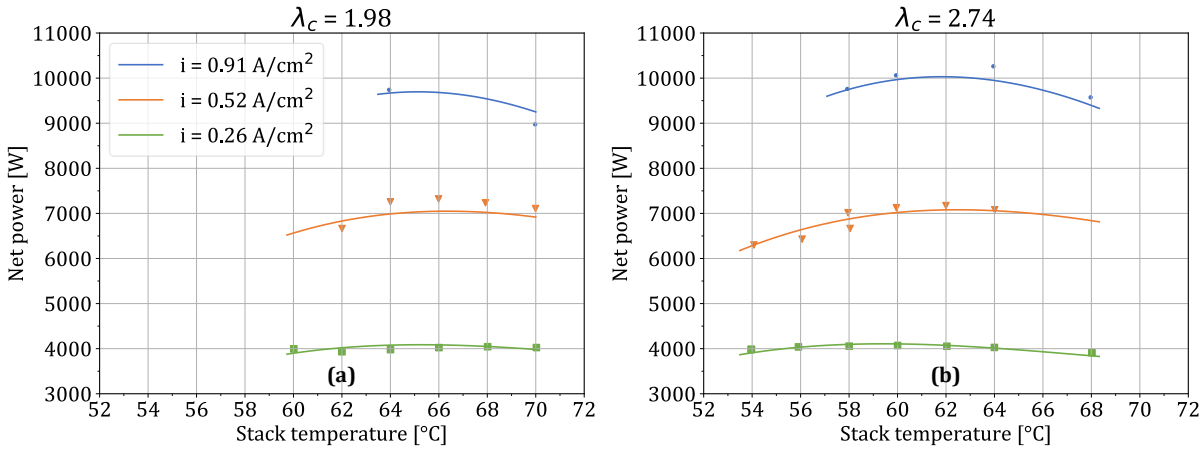

Figure 5.11: Net power output of three current levels versus stack temperature at 979 hPa with $\lambda_c = 1.98$ (a) $\lambda_c = 2.74$ (b).

In order to gain a better understanding of the correlation between stack temperature and cathode stoichiometry, contour plots were generated. They play a very important role in the study of the response surface, as they enable the characterization of surface shapes. Consequently, a three-dimensional space can be examined. Furthermore, it is possible to locate optima with reasonable precision.

Figure 5.12 displays contour plots for the three previously introduced current density levels: 0.26 A/cm², 0.52 A/cm², and 0.91 A/cm², valid for a pressure of 979 hPa. These plots enable the characterization of the interaction between cathode stoichiometry and stack temperature on the net power output. The colored areas show the range of validity of the regression model, while the areas where only isolines are shown serve the purpose of enhancing clarity and ease of interpretation. Figure 5.12c demonstrates a reduced temperature range due to the maximum current density level of 0.91 A/cm², which was determined with a maximum cathode outlet humidity of 80 % instead of 95 %. To provide further clarity, the range applicable to the other plots has been deposited as a gray scale. For all contour plots shown in Figure 5.12, the levels of the color bars are equivalent ($\Delta P_{net} = 80$ W), improving the comparability across the plots.

Upon reviewing the contour plots, it is obvious that between Figure 5.12a and b, as the current density increases, the number of color gradations increases or the distance between adjacent isolines decreases. This confirms the previous statement that the effect of the operating parameters stack temperature and cathode stoichiometry on the PEMFC performance increases with increasing current density. It is also noteworthy that these two plots primarily feature almost vertical isolines, indicating that the influence of stack temperature is significantly higher than that of stoichiometry. This also applies to Figure 5.12c, although the influence of stoichiometry is higher, as indicated by the ellipsis around the maximum.

For the lowest investigated current density of 0.26 A/cm², Figure 5.12a shows an optima region at the edge of the parameter space at the maximum investigated stoichiometric rate of 2.8. This can be justified by the negligible impact of the parasitic power demand for the air blower at low current densities, where a lower required airflow is present. This suggests considerable potential for further optimization, which could be explored by exceeding the stoichiometry limit of 2.8. In addition, it corresponds at least for the stoichiometric ratio to the default value of the manufacturer (cf. Table 3.2).

Moreover, it is noticeable in Figure 5.12a that there is a second region at a low stoichiometry with an elevated predicted net power output. This suggests that there may also be an increase in net power at low current densities when the stoichiometry is decreased ($\lambda_c \approx 2$). The membrane

humidification should be similar for both regions, as the positions of the increased predicted net power outputs, in relation to the temperature range, are similar for both $\lambda_c = 2$ and $\lambda_c = 2.8$, indicating comparable cathode outlet humidities. It is plausible that this might be attributed to the rising temperature, which positively affects the exchange current density i_0 and the ionic conductivity of the membrane, thus enhancing mass transport [15 p. 59]. Plus, the power demand of the air blower decreases with lower stoichiometry. However, a conclusive explanation for this phenomenon is still pending.

For the medium current density of 0.52 A/cm² examined here, Figure 5.12b reveals a minimal influence of the stoichiometry. If the stack temperature is around 65 °C, the net power would remain nearly unchanged across the entire range of stoichiometry investigated, from 2 to 2.8, with a deviation of less than 80 W from the maximum net power. Conversely, the temperature influence is more significant. Nevertheless, there is a relatively broad plateau (approximately 3 °C) where the net power output of the PEMFC system is expected to exhibit minimal changes.

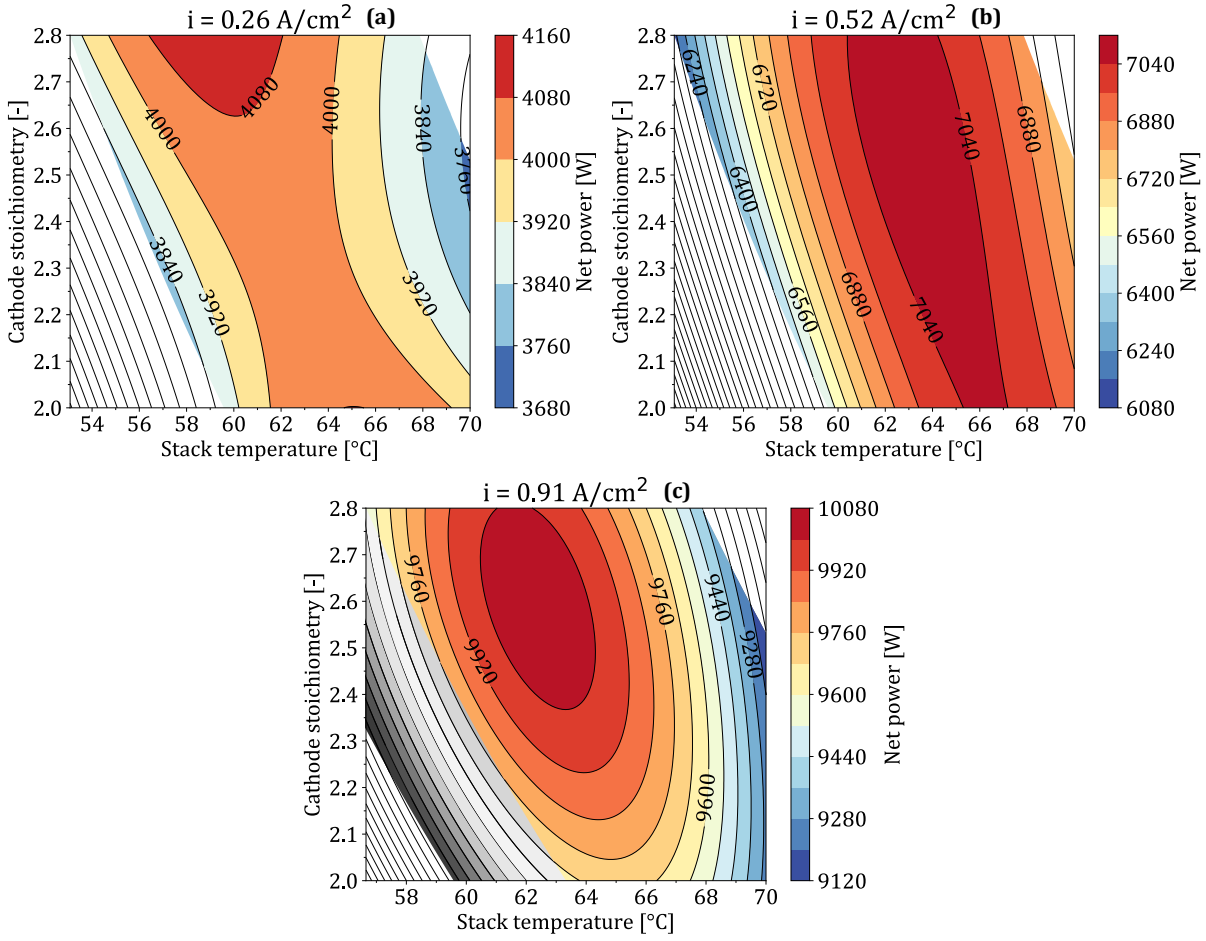

Figure 5.12: Interaction of cathode stoichiometry and stack temperature and their effect on the net power output for a current density of 0.26 A/cm² (a), 0.52 A/cm² (b) and 0.91 A/cm² (c) at 979 hPa.

For the maximum current density of 0.91 A/cm², Figure 5.12c illustrates a range where a performance maximum is predicted. This range encompasses a stack temperature between 61 °C and 64 °C and a stoichiometry between 2.4 and 2.8. As mentioned previously, the control of stoichiometry becomes substantially more important compared to lower current densities. This can be primarily attributed to the complex relationship involving concentration losses, membrane humidification, and air blower power consumption. The stoichiometric ratio must be sufficiently high to ensure an adequate supply of oxygen molecules to the three-phase boundary. However, if

the stoichiometry is too high, the power consumption of the air blower becomes dominant. Furthermore, the stack temperature must be adjusted in relation to the cathode stoichiometry to attain optimal membrane humidity for the operating condition.

In general, it can be concluded at this point, for a pressure of 979 hPa, that the current density has a significant impact on the control variables of stack temperature and cathode stoichiometry. Thus, water management becomes more crucial at higher current densities. In Section 5.3.3, Figure 5.17 presents the resulting optima as a function of current density for both parameters.

Effect of stack temperature and cathode stoichiometry at 500 hPa:

Figure 5.13 illustrates the net power output of three current levels as a function of stack temperature at the lowest investigated pressure level of 491 hPa, with a stochiometric ratio of $\lambda_c = 1.98$ in Figure 5.13a and $\lambda_c = 2.74$ in Figure 5.13b. The three selected current levels correspond to the lower, middle, and upper levels relative to the prevailing ambient pressure.

For the lower current densities of 0.13 A/cm^2 and 0.26 A/cm^2, the regression curves in Figure 5.13a and b exhibit a good fit to the measured data based on visual assessment. However, for the current density of 0.39 A/cm^2, the increased deviation of the model curve in Figure 5.13c indicates the limitations of the regression model. Nevertheless, the parameter combination present in that region represents the 'corner' of the experimental space, whereby this combination is most unfavorable. This is also evident from the restrictions encountered during the testing procedure. Only steady-state conditions could be recorded for a stack temperature of $T \geq 54$ °C, instead of the originally desired range beginning at 50 °C. However, as the objective of this study is to identify the optimal parameter combinations, which are typically not located at the edges of the experimental design space, the deviation of the model curve at this point can be tolerated.

As detected at 979 hPa, the influence of stack temperature is also more significant at higher current density levels under low-pressure conditions at 491 hPa. In Figure 5.13b, for a current density of 0.13 A/cm^2, the standard deviation of the measured values is approximately 12 W, whereas it increases to 52 W for 0.26 A/cm^2 and 85 W for 0.39 A/cm^2.

The maximum measured net power outputs exhibit a significant difference between low and high stoichiometry levels. At a stoichiometric rate of $\lambda_c = 2.74$, the FC system's performance is 14.4 % higher than at $\lambda_c = 1.98$ under low-pressure conditions. Thus, the influence of stoichiometry is significantly higher at altitude than at sea level. There, the difference between the maximum values of both stoichiometries was only 3.5 % (see Figure 5.11). However, at lower current densities, the influence is similarly negligible at 491 hPa, with a power increase of the measuring points of < 0.5 % in comparison between $\lambda_c = 1.98$ and $\lambda_c = 2.74$.

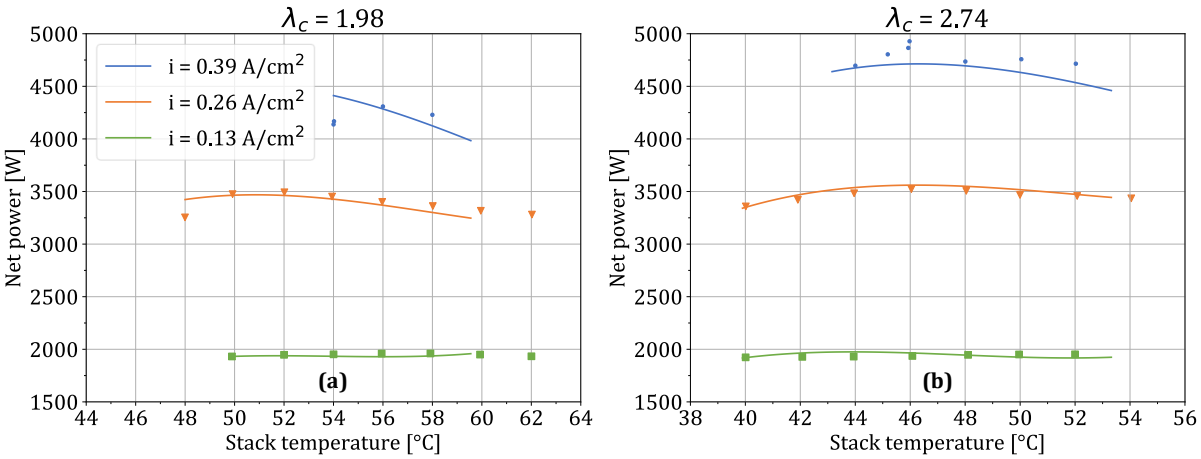

Figure 5.13: Net power output of three current levels versus stack temperature at 491 hPa with $\lambda_c = 1.98$ (a) $\lambda_c = 2.74$ (b).

To investigate the correlation between stack temperature and cathode stoichiometry at 491 hPa, contour plots are displayed in Figure 5.14 for the three current density levels of 0.13 A/cm², 0.26 A/cm², and 0.36 A/cm². The levels of the color bars and isolines are again kept constant, but the graduation with $\Delta P_{net} = 40$ W is only half the size compared to Figure 5.12 for 979 hPa.

When reviewing the contour plots, the concurrent increase in the number of color gradations that accompanies the increase in current density becomes apparent. This indicates that even under low-pressure conditions, the effect of the operating parameters stack temperature and cathode stoichiometry on the PEMFC performance becomes more pronounced with increasing current density. In contrast to the contour plots shown in Figure 5.12, those generated for 491 hPa exhibit an enhanced influence of cathode stoichiometry across all current density levels. This is evident from the presence of oval isolines surrounding all maximum regions. Thus, it can be concluded that control of cathode stoichiometry is more crucial under low-pressure conditions. This is certainly attributable to the higher power consumption of the air blowers under high-altitude conditions (cf. Figure 5.6a), as well as the lower oxygen partial pressure. This leads to a delicate balance between the reduction of concentration losses and the excessive power demand of the air blower. Consequently, optimal membrane humidification must primarily be controlled by adjusting the stack temperature.

It is also conspicuous that all optima are located within a similar stoichiometry range between 2.4 and 2.6. This is probably due to the efficiency of the air blower. However, to verify this claim, the blower would need to be fully characterized under low-pressure conditions.

For the lowest investigated current density of 0.13 A/cm² (see Figure 5.14a), it is particularly notable that an increase in net power output is expected at moderate stoichiometry settings of $\lambda_c \approx 2.4$ and high temperatures of $T \approx 55$ °C. This phenomenon was also observed during the testing procedure. One possible explanation could be that the power gain from the increasing temperature (which has a positive effect on exchange current density i_0, the conductivity of the membrane, etc. [15 p. 59]) outweighs the power losses resulting from the drier membrane and thus poorer proton conductivity. Additionally, the lower relative humidity results in a lower density in the anode circuit, leading to a reduced consumption of the recirculation pump (cf. Section 5.1.2 and Figure 5.2b). However, a final explanation of this phenomenon is still pending and is the subject of future research.

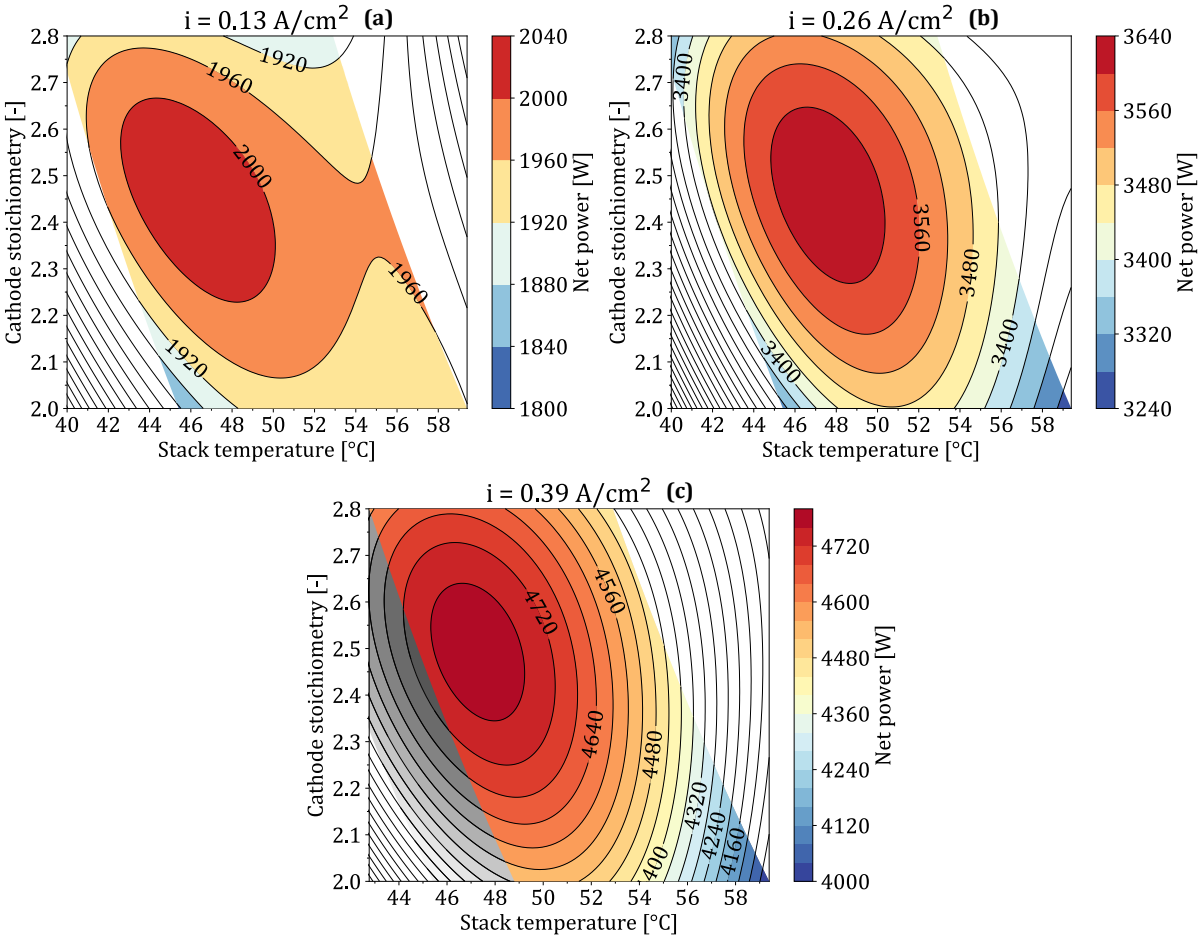

Figure 5.14: Interaction of cathode stoichiometry and stack temperature and their effect on the net power output for a current density of 0.13 A/cm² (a), 0.26 A/cm² (b) and 0.39 A/cm² (c) at 491 hPa.

Overall, for 491 hPa, the maximum net power output optima lie within the validity ranges of the regression model. This indicates that the parameter space has been well-constrained in the pre-experimental planning phase. The resulting optima as a function of current density for both influencing parameters can be found in Section 5.3.3, Figure 5.17.

Effect of pressure:

Since only the upper (1000 hPa) and lower pressure levels (500 hPa) of the investigation range have been considered so far, the effect of pressure across the entire low-pressure range is now being investigated. Figure 5.15 presents the net power output as a function of stack temperature for all six investigated pressure levels, at a current density of 0.26 A/cm² and a stoichiometry of $\lambda_c = 2.74$. The choice for this current density level is justified by the fact that it was investigated across all pressure levels, providing both measured data points and corresponding model curves. Additionally, the maximum predicted net power, determined through the optimization of the model equation with a current density of 0.26 A/cm² and a stoichiometry of $\lambda_c = 2.74$, is plotted as a red dashed line.

Incorporating the measurement points obtained during the pretests into the regression model reveals that the majority of data points are concentrated at pressures of 500 hPa and 1000 hPa, as shown in Figure 5.15. This is further amplified by the nature of the employed D-optimal design since it requires the boundary values of the parameter space in order to maximize the determinat of the information matrix.

When analyzing the model curves in Figure 5.15, it becomes apparent that the influence of temperature seems to be uniform across all pressure levels, but with a shifted temperature range. Calculating the difference between the maximum and minimum predicted net power values within the model's validity range, relative to the respective maximum achievable net power, yields values ranging from 6 % to 6.7 % for all six pressures. This finding confirms the aforementioned statement.

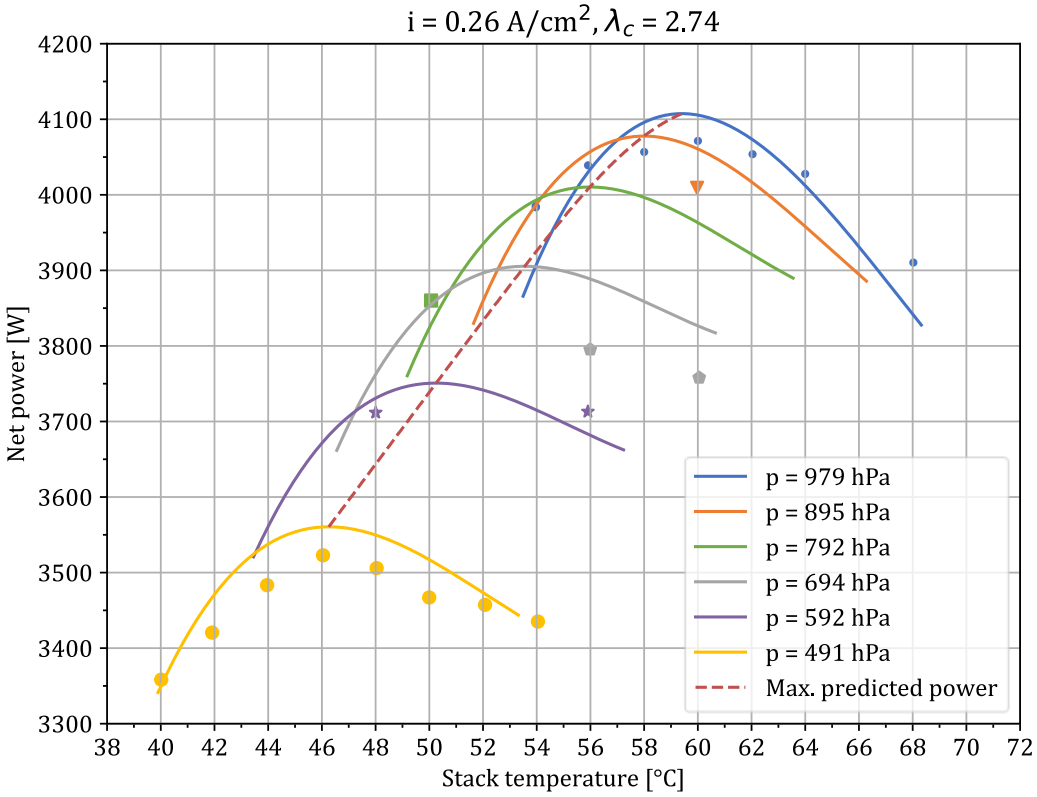

Figure 5.15: Net power output versus stack temperature for all six pressure levels with a current density of 0.26 A/cm² and cathode stoichiometry of 2.74.

Obviously, as the pressure decreases, the optimal temperature decreases to maintain a similar outlet humidity across all pressure levels. However, the absolute difference between the optimal temperatures increases at lower pressure levels. For example, between 979 hPa and 895 hPa, the difference is only 1.4 °C, whereas between 792 hPa and 694 hPa, it rises to 2.42 °C, and between 592 hPa and 491 hPa, it reaches 4.02 °C. This behavior can be explained by considering the saturation vapor pressure curve and Equation (2.22), assuming that the model optima result in the same optimal relative humidity at the cathode outlet. If the relative humidity is constant, the saturation vapor pressure must decrease proportionally to the ambient pressure. As the vapor pressure curve exhibits a lesser decrease for lower temperatures, this necessitates a greater temperature reduction to achieve the same ambient pressure to saturated vapor pressure ratio.

The effect of pressure on the maximum predicted net power increases with decreasing pressure, given a constant current density of 0.26 A/cm² and stoichiometry of 2.74, as shown in Figure 5.15. The difference between 979 hPa and 895 hPa is approximately 30 W, between 792 hPa and 694 hPa it rises to 103 W, and between 592 hPa and 491 hPa, it reaches 190 W. However, this also depends on how far the present operating parameters deviate from the optimum ones. Thus, the plot featuring a stoichiometry of 2.39, shown in Figure 5.16, displays a significantly different trajectory of the red dashed line representing the maximum predicted net power. Comparing the maximum net power outputs of the six pressure levels between Figure 5.16 and Figure 5.15

reveals that the performance is significantly poorer at higher pressures, while better at lower pressures at $\lambda_c = 2.39$. For instance, the value of the maximum predicted net power for 979 hPa with a stoichiometry of 2.74 is 68 W lower than that with a lower stoichiometry of 2.39. At 792 hPa, the net power outputs for both stoichiometries are approximately the same, with a difference of only 4 W. Conversely, at 491 hPa, the net power in Figure 5.16 with a stoichiometry of 2.39 is 65 W higher than that in Figure 5.15. This indicates a reduction in the optimal stoichiometry ratio under low-pressure conditions.

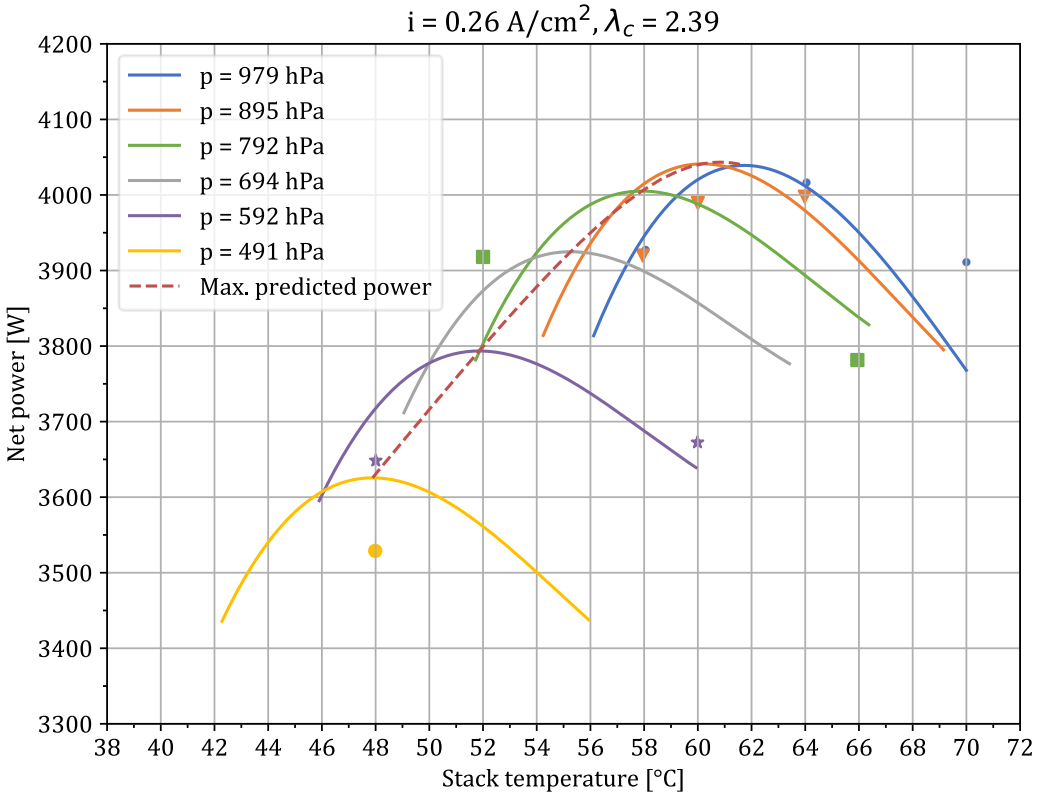

Figure 5.16: Net power output versus stack temperature for all six pressure levels with a current density of 0.26 A/cm² and cathode stoichiometry of 2.39.

5.3.3. Optimized Control Parameters

By employing a highly refined discretization of the parameters stack temperature, current density, and cathode stoichiometry, the optimal parameters for the respective pressure levels were determined using a 'brute-force' approach. This involved conducting a maximum value search based on the model equation. Figure 5.17 illustrates the optimized stack temperature and cathode stoichiometry parameters for 1000 hPa (dotted) and 500 hPa (dashed) as function of the current density. The default parameters are shown as solid lines. As can be seen, the optimized cathode stoichiometry curve for 1000 hPa is similar to the standard curve. The main difference lies in the subsequent decrease of stoichiometry from $\lambda_c = 2.8$ to approximately $\lambda_c \approx 2.6$, occurring at a higher current density of 0.4 A/cm² instead of 0.3 A/cm². This observation implies that a lower relative cathode outlet humidity is more favorable at sea-level conditions.

The optimized temperatures for a pressure of 1000 hPa, ranging from 57.2 °C to 63.3 °C, are significantly higher than the standard temperatures by up to approximately 8 °C difference at 0.5 A/cm². The kink observed in the temperature trend at 0.4 A/cm² in the dottet curve can be attributed to the corresponding decline in cathode stoichiometry. To maintain a similar outlet humidity level, a temperature increase is required as the stoichiometry decreases.

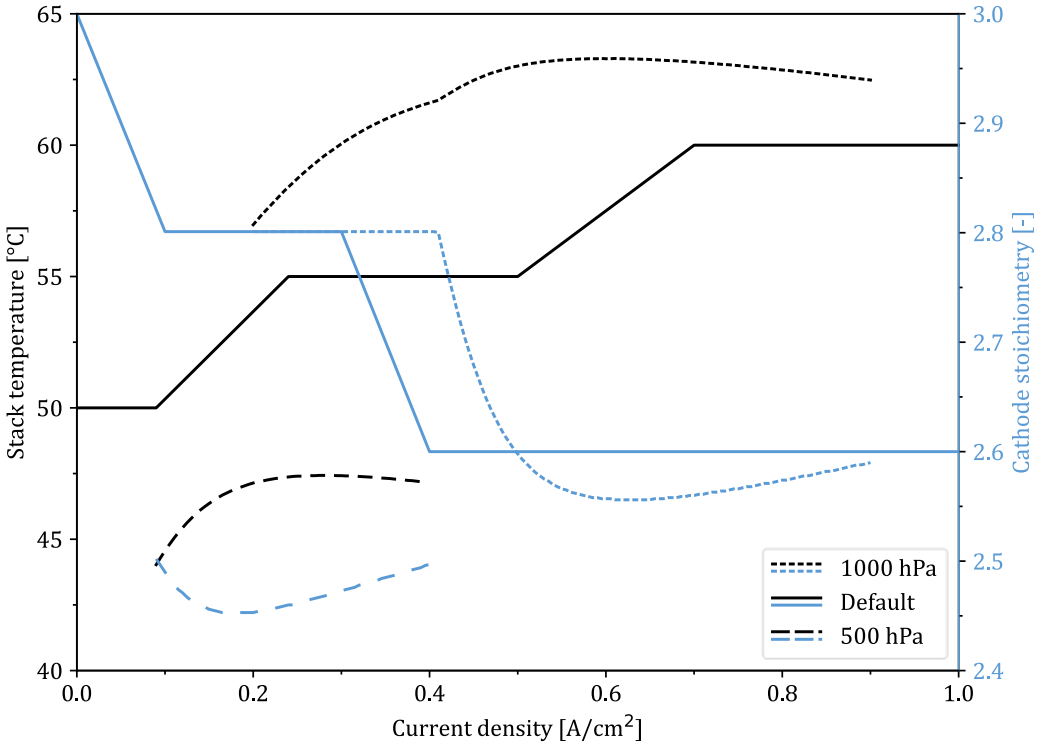

Figure 5.17: Stack temperature (solid) and cathode stoichiometry (dotted) control parameters versus current density.

The optimized stoichiometry values at 500 hPa deviate from the default manufacturer values, exhibiting lower levels. This can be attributed to the higher parasitic power demand of the air blower under low-pressure conditions, as well as increased drying effects at higher stoichiometries. The optimized values range from 2.45 to 2.50, demonstrating a relatively homogeneous distribution across the applicable current density range of the model. As expected, in order to achieve a higher relative cathode outlet humidity, the temperatures are significantly lower.

5.4. Polarization Curves with Optimized Parameters

To validate the determined optimal control parameters and to compare the net power outputs obtained with the default parameters, polarization curves were recorded. Due to the power distribution controller of the fuel cell accepting only discrete values at intervals of up one decimal place of the cathode stoichiometry, the values provided in Table 5.5 and Table 5.6 were employed for capturing the polarization curves at 1000 hPa and 500 hPa, respectively. These values consider not only the discretization possibility but also the remaining offset of the cathode stoichiometry of $\lambda_{c,off} = 0.036$ introduced in Section 5.1.1. When examining the contour plots for the maximum current density at 1000 hPa (cf. Figure 5.12c) and 500 hPa (cf. Figure 5.14c), it can be observed that the deviation from the predicted maximum net power is only marginal.

Figure 5.18 depicts the comparison of the polarization curves and the system net power outputs, obtained with default and optimized temperatures and stoichiometry values at 1000 hPa. The solid and dashed lines represent the results obtained with standard and optimized parameters, respectively. Since the model equation is valid only up to a current density of 0.897 A/cm² (175 A) at 1000 hPa, no corresponding value for the maximum measurement of the curves with default parameters is included.

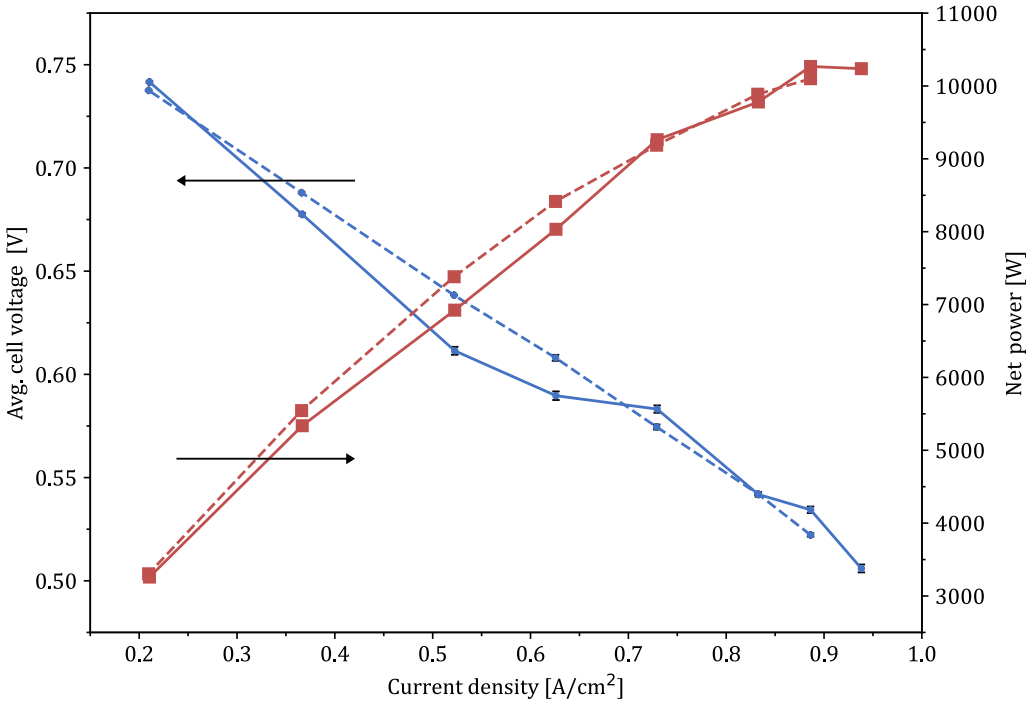

Figure 5.18: Comparison of the polarization curve (dots) and the net power output (squares) measured with default (solid lines) and with optimized parameters (dashed lines) at 1000 hPa.

Current density [A/cm²]	Temperature [°C]	ΔT default [°C]	Stoichiometry [-]	$\Delta\lambda_c$ default [-]
0.205	57.4	+3.4	2.76	+0.10
0.359	61.2	+6.2		+0.22
0.513	63.2	+8.0	2.56	+0.10
0.615	63.3	+5.3		
0.718	63.1	+3.1		
0.821	62.9	+2.9		
0.872	62.7	+2.7		

Table 5.5: Optimal control parameters for polarization curve at 1000 hPa.

By comparing the two polarization curves, it is evident that the curve obtained with optimized parameters (dashed line) exhibits a typical linear trend in the region of predominantly ohmic losses. Consequently, there is a consistent improvement in net power for the measurement values with a current density < 0.7 A/cm². At a current density of 0.522 A/cm², the maximum measured difference is observed, indicating a moderate net power gain of 6.6 %. For the maximum measured value at a current density of 0.886 A/cm², a net power loss of < 1 % was measured. It can be assumed that this loss falls within the range of test variability. Since fuel cell systems are usually operated in moderate current density ranges due to the decline in efficiency at high current densities, the net power gain achieved in that range is quite remarkable. Additionally, the presence of a linear trend in the region of predominantly ohmic losses can validate the hypothesis that the default control parameters are not optimal for the measurement points in the range of 0.5 A/cm² to 0.7 A/cm².

The polarization curves and net power outputs at 500 hPa are compared in Figure 5.19, considering both default and optimized temperature and stoichiometry values. The solid and dashed lines further correspond to the curves obtained with default and optimized parameters, respectively. The data points presented as individual markers were acquired during the parameter study involving manual optimization of stack temperature and cathode stoichiometry

values, as they lie beyond the valid range of the model equation. These data points should be interpreted as an indication of further potential for optimization.

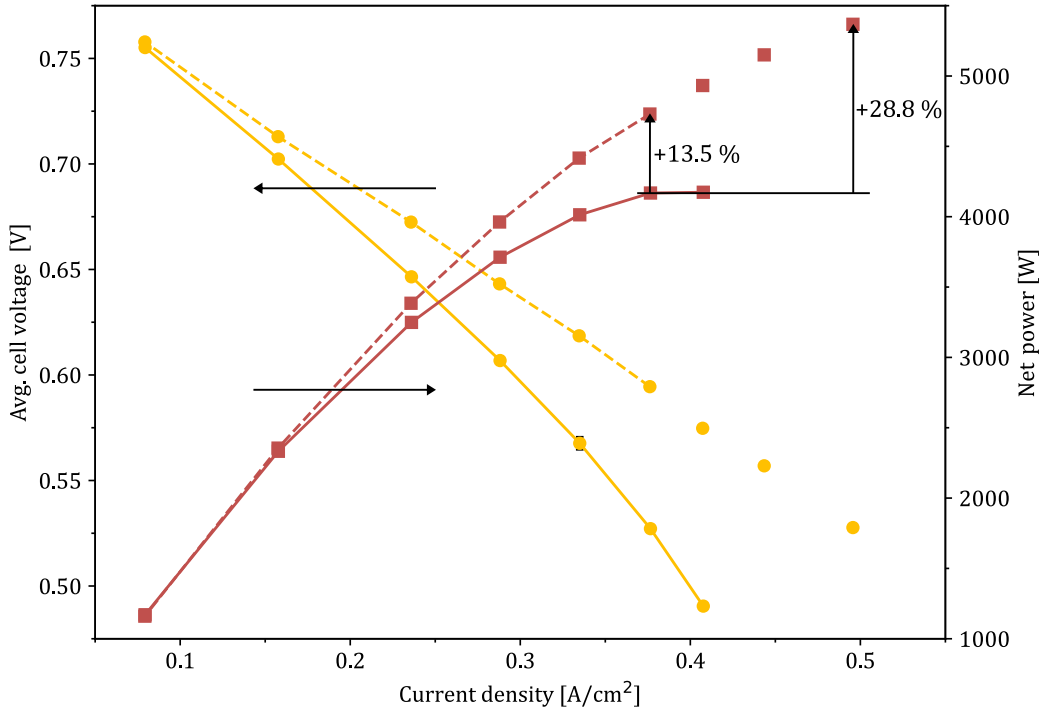

Figure 5.19: Comparison of the polarization curve (dots) and the net power output (squares) measured with default (solid lines) and with optimized parameters (dashed lines) at 500 hPa.

Current density [A/cm²]	Temperature [°C]	ΔT default [°C]	Stoichiometry [-]	$\Delta\lambda_c$ default [-]
0.077	42.8	-7.2	2.56	-0.26
0.154	46.4	-5.6	2.46	-0.20
0.231	47.3	-4.0		
0.282	47.4	-7.6		
0.328				-0.14
0.370				-0.06

Table 5.6: Optimal control parameters for the polarization curve at 500 hPa.

A comparison of the polarization curves reveals that the curve obtained with optimized parameters (dashed line) is significantly higher than that obtained with default parameters. At the final measurement point, acquired using the optimal control parameters determined from the model equation (at 0.376 A/cm²), the average cell voltage remains well above the minimum tolerable threshold of 0.5 V, i.e., 0.59 V. Moreover, the polarization curve exhibits a highly linear trend, showing no signs of approaching the limiting current density, indicating that no dominant mass-transport losses are imminent. This trend is continued by the measurement points obtained with the manually optimized parameters.

When comparing the net power outputs of the curves obtained with optimized and default parameters, a significant net power enhancement of 561 W, corresponding to 13.5 %, is evident at 0.376 A/cm². Considering the results obtained with manually optimized parameters, a future power increase of 28.8 % or beyond can be anticipated.

The optimization of the control parameters also led to significant improvements in the system efficiency, based on the lower heating value $\eta_{Net,LHV}$. Figure 5.20 shows the system efficiencies

measured with default and with optimized parameters as a function of the net power at 500 hPa and 1000 hPa. As described in Section 5.1.2, these were calculated using the corrected fuel utilization coefficient and Equation (2.16). It is evident that the system efficiency curve recorded with optimized control parameters at 1000 hPa is considerably higher than the one measured with default parameters up to about 9000 W net power. At around 7000 W net power, the system efficiency gain is about 3.6 % in absolute terms. At a pressure level of 500 hPa, the system efficiency gain is even more pronounced. At 4000 W, an absolute increase of 5.8 % was achieved, corresponding to a relative increase of 14.9 %.

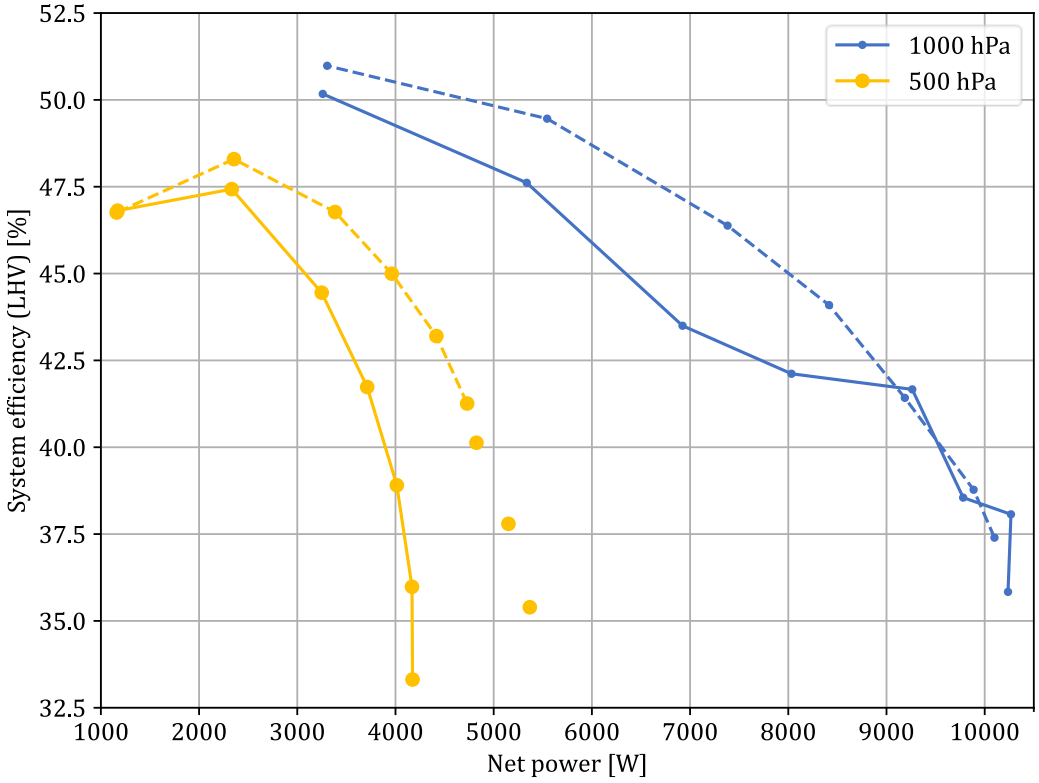

Figure 5.20: System efficiency referring to the LHV in relation to the net power with default (solid lines) and with optimized (dashed lines) parameters at 500 hPa and 1000 hPa.

Upon comparing the recorded profiles for 1000 hPa and 500 hPa with optimized control parameters (dashed lines) at an altitude of about 5700 m (according to the ISA [39]) a relative efficiency loss of only 11.2 % has to be expected, without taking into account the temperature influences prevailing at that altitude. With the default control parameters, this loss was nearly twice as high at 21 % (cf. Section 5.1.2).

Figure 5.21 depicts a comparison of the relative humidity at the cathode outlet, measured with default and optimized stack temperature and cathode stoichiometry parameters at 500 hPa and 1000 hPa. Additionally, the measurements obtained with manually optimized parameters are represented as individual data points. As expected, the cathode outlet humidities of the measurements with optimized control parameters at 500 hPa are significantly higher compared to those obtained with default values. Therefore, the performance and efficiency improvement can be attributed to a moister membrane and thus enhanced proton conductivity. Interestingly, the results obtained with optimized parameters align at both pressure levels.

These findings indicate the presence of a pressure-independent optimal outlet humidity that depends only on the current density. The profile of the optimal outlet humidity starts at around 70 % for low current densities and decreases to 55 % for high current densities. Based on these

findings, it may be conceivable to utilize an adapted fuel cell controller that regulates based on the cathode outlet humidity.

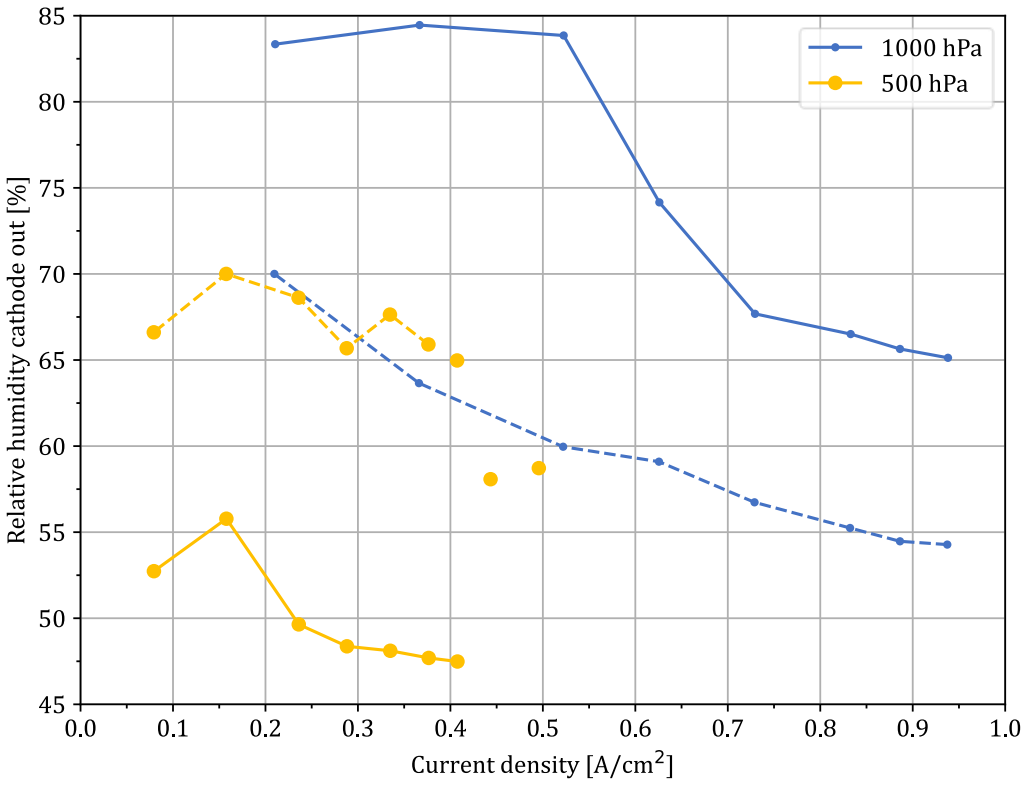

Figure 5.21: Relative humidity at the cathode outlet measured with default (solid lines) and with optimized (dashed lines) parameters at 500 hPa and 1000 hPa.

6. Conclusion and Outlook

Within the scope of this research, a proton-exchange membrane fuel cell system based on a Hydrogenics HyPM® HD 10-120 stack was tested under low-pressure conditions to investigate its performance. The experimental analysis was conducted in the test facility developed at the German Aerospace Center, the Altitude Test Chamber for Low Pressure Analysis of FC Systems.

To quantify the performance losses associated with low pressure, the first phase involved recording polarization curves at six distinct pressure levels ranging from 1000 hPa to 500 hPa. Throughout the investigation, the default control parameters for cathode stoichiometry and stack temperature, as recommended by the manufacturer, were applied. At 500 hPa, corresponding to an altitude of approximately 5700 m according to the ISA [39], the measurements indicated net power losses of up to 59 % and system efficiency losses of 21 % compared to 1000 hPa. These losses were primarily attributed to two factors. Firstly, the reduced total pressure and the consequent decrease in oxygen partial pressure. Secondly, operating under low-pressure conditions resulted in a lower water vapor partial pressure, leading to membrane drying. This reduces the proton conductivity and thus contributed significantly to the performance losses.

The operation under altitude conditions also impacted the BoP components. Due to the lower density at decreasing ambient pressure, an increased power demand for the air blower was observed to maintain the required mass flow. In addition, the hot wire mass flow sensor used for cathode stoichiometry control proved to be not suitable for regulating a PEMFC system in an aviation environment, at least without compensation. Conversely, the constant-speed controlled anode recirculation pump experienced a lower power demand due to the reduced density, however, it also resulted in a lower mass flow. This probably had a negative impact on the performance of the PEMFC system as it compromised the homogeneous humidification and led to premature local fuel starvation on the anode side. Therefore, it was recommended that future operations of fuel cells under altitude conditions should regulate the recirculation pump based on the mass flow.

Additionally, by fitting a simplified empirical fuel cell polarization curve model to the measurement data, trends of certain voltage losses were identified. An increase in ohmic losses, attributed to a larger internal resistance under low-pressure conditions, was observed. The regression analysis of the data points also revealed a decrease in limiting current density with decreasing pressure, as well as a greater concentration polarization under low-pressure conditions.

The polarization curves obtained at different pressure levels demonstrated that operating the self-humidifying PEMFC system with standard control parameters is limited at high altitudes due to issues with water management.

In general, specific temperature ranges were identified where the FC system exhibited steady operational behavior. These ranges shifted towards lower temperatures under reduced ambient pressures and also showed a certain stoichiometry dependence. This can be attributed to maintaining an optimal stack humidity. Results revealed that the stack temperature has a more significant influence on water management and, consequently, net power output than stoichiometry. Furthermore, these effects are dependent on the current density, with deviations from optimal operating parameters associated with greater power losses at higher current densities. Therefore, precise temperature regulation is particularly important, especially at high current densities.

The findings also indicate that in low-pressure conditions, the effect of stack temperature on the net power output remains consistently significant. Conversely, the influence of stoichiometry

demonstrates pressure dependency, primarily due to the increased parasitic power demand of the air blower and the decreased oxygen partial pressure. This emphasizes that exact control of cathode stoichiometry at high altitudes is even more crucial.

In conclusion, the optimal operating conditions resulting from the model equation were presented. Furthermore, a comparison was made between the polarization curves obtained using default control parameters and those obtained with the optimal control parameter. At 1000 hPa, a moderate net power gain of up to 6.6 % was achieved across the medium current density range. Applying the optimized parameters at an ambient pressure of 500 hPa led to a 13.5 % increase of the maximum net power compared to the results obtained with standard control parameters. Preliminary results with manually optimized parameters which extend beyond the validity range of the model equation, indicated that the net power output can be increased by 29 % or even more with further analysis. The system efficiency also demonstrated substantial enhancement possibilities for both 1000 hPa and 500 hPa. Ultimately, the relative efficiency loss was diminished from 21 % to approximately 11 % between sea level and an altitude of 5700 m.

When considering the relative humidity at the cathode outlet, it was observed that the results with optimized temperature and stoichiometry parameters aligned within the range of 55 % to 70 % both at 1000 hPa and 500 hPa. Furthermore, the optimal cathode exhaust humidity shifted to lower values as the current densities increased. This suggests that the relative humidity at the cathode outlet can serve as a pressure-independent control variable.

In summary, the investigation has revealed significant potential for optimizing the operation of PEM fuel cells under high-altitude conditions. By determining the optima of the developed model equation, the objective of this research, i.e., the creation of a map with optimal operating conditions, has been achieved. Additionally, the regression model has characterized the net power output behavior of the PEMFC system across the entire validity range of the model. An extension could potentially lead to significantly higher performance of the FC system in the future, as the current validity range is limited to the current density levels with maximum net power output under default control parameters. Additionally, it would be advantageous to perform investigations with further reduced pressures corresponding to the cruising altitudes of regional aircraft, using the optimized parameters as a starting point. Furthermore, experimental investigations on the impact of the prevailing low temperature on the PEMFC system would be of interest.

The measured data obtained in the scope of this research exhibit potential for future analyses. If it is possible to adjust erroneous measurements from the hydrogen mass flow meters, it would be possible to determine the correct fuel utilization coefficient, enabling a comprehensive investigation of system efficiency. With respect to system efficiency, it will be interesting to vary the factors declared held-constant factors in this study, such as the anode purge rate and anode stoichiometry. Thus, system efficiency could be optimized as a response variable. Considering the application in aircraft, it would be possible to select different optimal parameter configurations for various flight phases. While maximum net power is required during takeoff and climb, the fuel cell should be operated with parameter configurations in cruise that align with optimal efficiency.

The present investigation demonstrates that model-based experimental design is a powerful tool for fuel cell characterization. By employing this experimental design methodology, efforts, costs, and time were kept within reasonable limits. Among the optimal experimental design criteria, the D-optimal criterion was selected due to its availability and popularity. Nevertheless, for future studies, it would be preferable to select I-optimal or V-optimal experimental designs, as they focus their attention on the middle prediction quality in the experimental space [27 p. 56]. Under appropriate parameter space constraints, the optima are expected to be found in that area.

However, this would require the use of commercial software such as JMP, Minitab, or Visual-XSel. Moreover, the utilization of specialized software would save time during the analysis process through a wide range of statistical tests, model optimization techniques, and simplified visualization capabilities, potentially leading to novel findings. In future investigations, it may also be beneficial to employ a semi-empirical mathematical model as a basis for model-based experimental design. This approach would allow for a more in-depth characterization of, for example, thermal or electrochemical properties.

The research indicates that there is a high potential for optimization solely through stack temperature and cathode stoichiometry control, without significant additional power demand for BoP components. This implies that this finding might also be applicable to pressurized fuel cell systems. Consequently, systems could operate with lower pressurization under high-altitude conditions, contrary to the current trend in the industry. As a result, lighter and smaller compressors could be employed, which would be advantageous for aircraft design.

In conclusion, based on the performance improvements achieved in this study, there is still significant potential to be exploited. Therefore, the approach of utilizing polymer electrolyte membrane fuel cell-based powertrains for regional aircraft proves to be highly promising. However, there remains a considerable need for further research and development efforts to achieve complete decarbonization of the aviation sector.

References

[1] AIR TRANSPORT ACTION GROUP (ATAG). *Commitment to Fly Net Zero 2050* [online]. 2021 [accessed. 2023-04-30]. Available at: https://aviationbenefits.org/media/167501/atag-net-zero-2050-declaration.pdf

[2] EC-EUROPEAN COMMISSION. Communication from the Commission to the European Parliament, the European Council, the Council, the European Economic and Social Committee and the Committee of the Regions – The European Green Deal. *Document 52019DC0640*. 2019, **640**.

[3] INTERNATIONAL CIVIL AIR TRANSPORT ORGANISATION (ICAO). Consolidated statement of continuing ICAO policies and practices related to environmental protection – Carbon Offsetting and Reduction Scheme for International Aviation (CORSIA). *Resolution A41-22*. 2022.

[4] PRESS OFFICE - GENERAL SECRETARIAT OF THE COUNCIL. *Council and Parliament agree to decarbonise the aviation sector* [online]. 25. April 2023 [accessed. 2023-04-30]. Available at: https://www.consilium.europa.eu/en/press/press-releases/2023/04/25/council-and-parliament-agree-to-decarbonise-the-aviation-sector/

[5] RAO, A., F. YIN and H. WERIJ. Energy Transition in Aviation: The Role of Cryogenic Fuels. *Aerospace*. 2020, **7**(12), 181. ISSN 2226-4310. Available at: doi:10.3390/aerospace7120181

[6] PRAPOTNIK BRDNIK, A., R. KAMNIK, M. MARKSEL and S. BOŽIČNIK. Market and Technological Perspectives for the New Generation of Regional Passenger Aircraft. *Energies*. 2019, **12**(10), 1864. ISSN 1996-1073. Available at: doi:10.3390/en12101864

[7] MCKINSEY & COMPANY. *Hydrogen-powered aviation: A fact-based study of hydrogen technology, economics, and climate impact by 2050* [online]. LU: Publications Office of the European Union, 2020 [accessed. 2023-05-02]. Available at: https://data.europa.eu/doi/10.2843/766989

[8] BAROUTAJI, A., T. WILBERFORCE, M. RAMADAN and A. OLABI. Comprehensive investigation on hydrogen and fuel cell technology in the aviation and aerospace sectors. *Renewable and Sustainable Energy Reviews*. 2019, **106**, 31–40. ISSN 13640321. Available at: doi:10.1016/j.rser.2019.02.022

[9] COLPAN, C. and A. KOVAČ, eds. *Fuel Cell and Hydrogen Technologies in Aviation* [online]. Cham: Springer International Publishing, 2022 [accessed. 2023-05-01]. Sustainable Aviation. ISBN 978-3-030-99017-6. Available at: doi:10.1007/978-3-030-99018-3

[10] AIRBUS PRESS RELEASE. *Airbus reveals hydrogen-powered zero-emission engine* [online]. 30. November 2022 [accessed. 2023-09-05]. Available at: https://www.airbus.com/en/newsroom/press-releases/2022-11-airbus-reveals-hydrogen-powered-zero-emission-engine

[11] CHANG, V. and John GALLMAN. Altitude Testing of Fuel Cell Systems for Aircraft Applications. *SAE Transactions*. 2004, **113**, 1943–1957. Available at: doi:10.4271/2004-01-3200

[12] PRATT, J., J. BROUWER and G. SAMUELSEN. Performance of Proton Exchange Membrane Fuel Cell at High-Altitude Conditions. *Journal of Propulsion and Power*. 2007, **23**(2), 437–444. ISSN 0748-4658, 1533-3876. Available at: doi:10.2514/1.20535

[13] HORDÉ, T., P. ACHARD and R. METKEMEIJER. PEMFC application for aviation: Experimental and numerical study of sensitivity to altitude. *International Journal of Hydrogen Energy*. 2012, **37**(14), 10818–10829. ISSN 03603199. Available at: doi:10.1016/j.ijhydene.2012.04.085

[14] WERNER, C., F. GORES, L. BUSEMEYER, J. KALLO, S. HEITMANN and M. GRIEBENOW. Characteristics of PEMFC operation in ambient- and low-pressure environment considering the fuel cell humidification. *CEAS Aeronautical Journal*. 2015, **6**(2), 229–243. ISSN 1869-5582, 1869-5590. Available at: doi:10.1007/s13272-014-0142-z

[15] BARBIR, F. *PEM Fuel Cells: Theory and Practice*. 2nd edition. Amsterdam; Boston; Heidelberg; London; New York; Oxford; Paris; San Diego; San Francisco; Singapore; Sydney; Tokyo: Elsevier Academic Press, 2013. ISBN 978-0-12-387710-9.

[16] SCHRÖTER, J., T. GRAF, D. FRANK, C. BAUER, J. KALLO and C. WILLICH. Influence of pressure losses on compressor performance in a pressurized fuel cell air supply system for airplane applications. *International Journal of Hydrogen Energy*. 2021, **46**(40), 21151–21159. ISSN 0360-3199. Available at: doi:10.1016/j.ijhydene.2021.03.218

[17] WERNER, C., G. PREISS, F. GORES, M. GRIEBENOW and S. HEITMANN. A comparison of low-pressure and supercharged operation of polymer electrolyte membrane fuel cell systems for aircraft applications. *Progress in Aerospace Sciences*. 2016, **85**, 51–64. ISSN 0376-0421. Available at: doi:10.1016/j.paerosci.2016.07.005

[18] DICKS, A. and D. RAND. *Fuel Cell Systems Explained*. 3rd edition. Hoboken, NJ, USA: John Wiley & Sons Ltd., 2018. ISBN 978-1-118-61352-8.

[19] WERNER, C., L. BUSEMEYER and J. KALLO. The impact of operating parameters and system architecture on the water management of a multifunctional PEMFC system. *International Journal of Hydrogen Energy*. 2015, **40**(35), 11595–11603. ISSN 0360-3199. Available at: doi:10.1016/j.ijhydene.2015.02.012

[20] WERNER, C., F. GORES, J. KALLO, S. HEITMANN and M. GRIEBENOW. Merkmale des PEMFC-Betriebes bei Umgebungs- und Unterdruckbedingungen. In: *62. Deutscher Luft- und Raumfahrtkongress 2013* [online]. 2013 [accessed. 2023-04-25]. Available at: https://elib.dlr.de/84939/

[21] WERNER, C., G. PREISS, F. GORES, M. GRIEBENOW and S. HEITMANN. Pressure-Dependent Operation of Polymer Electrolyte Membrane Fuel Cells; Exemplified by Aircraft Applications. In: Detlef SCHULZ, ed. *NEIS Conference 2016* [online]. Wiesbaden: Springer Vieweg, 2017, p. 163–168 [accessed. 2023-03-14]. Available at: doi:https://doi.org/10.1007/978-3-658-15029-7_25

[22] SONG, W., H. CHEN, H. GUO, F. YE and J. LI. Research progress of proton exchange membrane fuel cells utilizing in high altitude environments. *International Journal of Hydrogen Energy*. 2022, **47**(59), 24945–24962. ISSN 0360-3199. Available at: doi:10.1016/j.ijhydene.2022.05.238

[23] KURZWEIL, P. *Brennstoffzellentechnik: Grundlagen, Materialien, Anwendungen, Gaserzeugung*. 3rd ed. Wiesbaden: Springer Vieweg, 2016. ISBN 978-3-658-14934-5. Available at: doi:10.1007/978-3-658-14935-2

[24] ZHANG, J., H. ZHANG, J. WU and J. ZHANG. *PEM Fuel Cell Testing and Diagnosis*. Amsterdam ; Boston: Elsevier, 2013. ISBN 978-0-444-53688-4.

[25] KAUR, G., ed. *PEM Fuel Cells: Fundamentals, Advanced Technologies, and Practical Application*. Amsterdam Kidlington Cambridge, MA: Elsevier, 2021. ISBN 978-0-12-823708-3.

[26] DEAN, A., D. VOSS and D. DRAGULJIĆ. *Design and Analysis of Experiments*. 2nd edition. New York: Springer International Publishing AG, 2017. ISBN 978-3-319-52248-7.

[27] SIEBERTZ, K., D. BEBBER and T. HOCHKIRCHEN. *Statistische Versuchsplanung: Design of Experiments (DoE)*. 2. Auflage. Berlin, Heidelberg: Springer Vieweg, 2017. VDI-Buch. ISBN 978-3-662-55742-6. Available at: doi:10.1007/978-3-662-55743-3

[28] MONTGOMERY, D. *Design and Analysis of Experiments*. 8. ed, international student version. Hoboken, NJ: Wiley, 2013. ISBN 978-1-118-09793-9.

[29] KLEPPMANN, W. *Versuchsplanung: Produkte und Prozesse optimieren* [online]. 10th ed. München: Carl Hanser Verlag GmbH & Co. KG, 2020 [accessed. 2023-04-07]. ISBN 978-3-446-46146-8. Available at: doi:10.3139/9783446463974

[30] STAECK, R. *Optimierung des Wasserhaushalts eines PEM-Brennstoffzellenaggregats*. 1. Auflage. Göttingen: Cuvillier, 2014. ISBN 978-3-95404-756-7.

[31] BECKER, F. *Manuscript of the lecture: PEM – Brennstoffzellensysteme: 1. Grundlagen*. Manuscript. Hamburg, 2021.

[32] VDI E. V., ed. *VDI Heat Atlas*. 2nd edition. Berlin ; New York: Springer, 2010. VDI-Buch. ISBN 978-3-540-77876-9.

[33] LINSTROM, P. and W. MALLARD, eds. *NIST Chemistry WebBook, NIST Standard Reference Database 69* [online]. Gaithersburg MD, 20899 (US): National Institute of Standards and Technology, 1997 [accessed. 2023-04-02]. Available at: doi:10.18434/T4D303

[34] DAI, W., H. WANG, X. YUAN, J. MARTIN, D. YANG, J. QIAO and J. MA. A review on water balance in the membrane electrode assembly of proton exchange membrane fuel cells. *International Journal of Hydrogen Energy*. 2009, **34**(23), 9461–9478. ISSN 03603199. Available at: doi:10.1016/j.ijhydene.2009.09.017

[35] *IAPWS Industrial Formulation 1997 for the Thermodynamic Properties of Water and Steam*. B.m.: International Association for the Properties of Water and Steam (IAPWS). 2007. Available at: http://www.iapws.org/relguide/IF97-Rev.html

[36] WAHDAME, B., D. CANDUSSO, X. FRANCOIS, F. HAREL, J. KAUFFMANN and G. COQUERY. Design of experiment techniques for fuel cell characterisation and development. *International Journal of Hydrogen Energy*. 2008, **34**(2), 967–980. ISSN 03603199. Available at: doi:10.1016/j.ijhydene.2008.10.066

[37] MEILER, M., D. ANDRE, Á. PÉREZ, O. SCHMID and E. P. HOFER. Nonlinear D-optimal design of experiments for polymer–electrolyte–membrane fuel cells. *Journal of Power Sources*. 2009, **190**(1), Selected Papers presented at the 11th ULM ElectroChemical Days, 48–55. ISSN 0378-7753. Available at: doi:10.1016/j.jpowsour.2008.08.068

[38] CRGRAPH. *D-Optimaler Versuchsplan* [online]. [accessed. 2022-12-12]. Available at: https://crgraph.de/downloads/docs/versuchsmethoden/Versuchsplanung.pdf

[39] INTERNATIONAL CIVIL AVIATION ORGANISATION (ICAO). *Manual of the ICAO Standard Atmosphere - extended to 80 kilometres (262500 feet)* [online]. 1993 [accessed. 2023-05-09]. Available at: https://store.icao.int/en/manual-of-the-icao-standard-atmosphere-extended-to-80-kilometres-262500-feet-doc-7488

[40] *HyPm® HD 10-120 Product Manual*. B.m.: Hydrogenics Corporation. 2018

[41] EUROPEAN COMMISSION, JOINT RESEARCH CENTRE (JRC). *PEFC Power Stack Performance Testing Procedure. Measuring Voltage and Power as Function of Current Density. Polarisation Curve Test Method.* [online]. Luxembourg: Publications Office, 2010 [accessed. 2023-04-18]. Available at: https://data.europa.eu/doi/10.2790/18880

[42] EUROPEAN COMMISSION, JOINT RESEARCH CENTRE (JRC) and ARGONNE NATIONAL LABORATORY (ANL). *Fuel Cell Testing Protocols: An International Perspective* [online]. Luxembourg: Publications Office, 2013 [accessed. 2023-04-18]. Available at: https://data.europa.eu/doi/10.2790/86676

[43] TRUONG, C., L. OUDRE and N. VAYATIS. Selective review of offline change point detection methods. *Signal Processing*. 2020, **167**, 107299. ISSN 01651684. Available at: doi:10.1016/j.sigpro.2019.107299

[44] THE MATHWORKS INC. *MATLAB Help Center - candexch* [online]. [accessed. 2023-04-24]. Available at: https://de.mathworks.com/help/stats/candexch.html

[45] SEABOLD, S. and J. PERKTOLD. Statsmodels: Econometric and Statistical Modeling with Python. In: *Python in Science Conference* [online]. 2010, p. 92–96 [accessed. 2023-05-16]. Available at: doi:10.25080/Majora-92bf1922-011

[46] MARTYR, A. and M. PLINT. *Engine Testing: The Design, Building, Modification and Use of Powertrain Test Facilities*. Fourth edition. Oxford ; Waltham, MA: Butterworth-Heinemann, 2012. ISBN 978-0-08-096949-7.

[47] KIM, J., S. LEE, S. SRINIVASAN and C. CHAMBERLIN. Modeling of Proton Exchange Membrane Fuel Cell Performance with an Empirical Equation. *Journal of The Electrochemical Society*. 1995, **142**(8), 2670. ISSN 1945-7111. Available at: doi:10.1149/1.2050072

Appendix A Process Engineering Setup

Appendix A.1 P&IDs

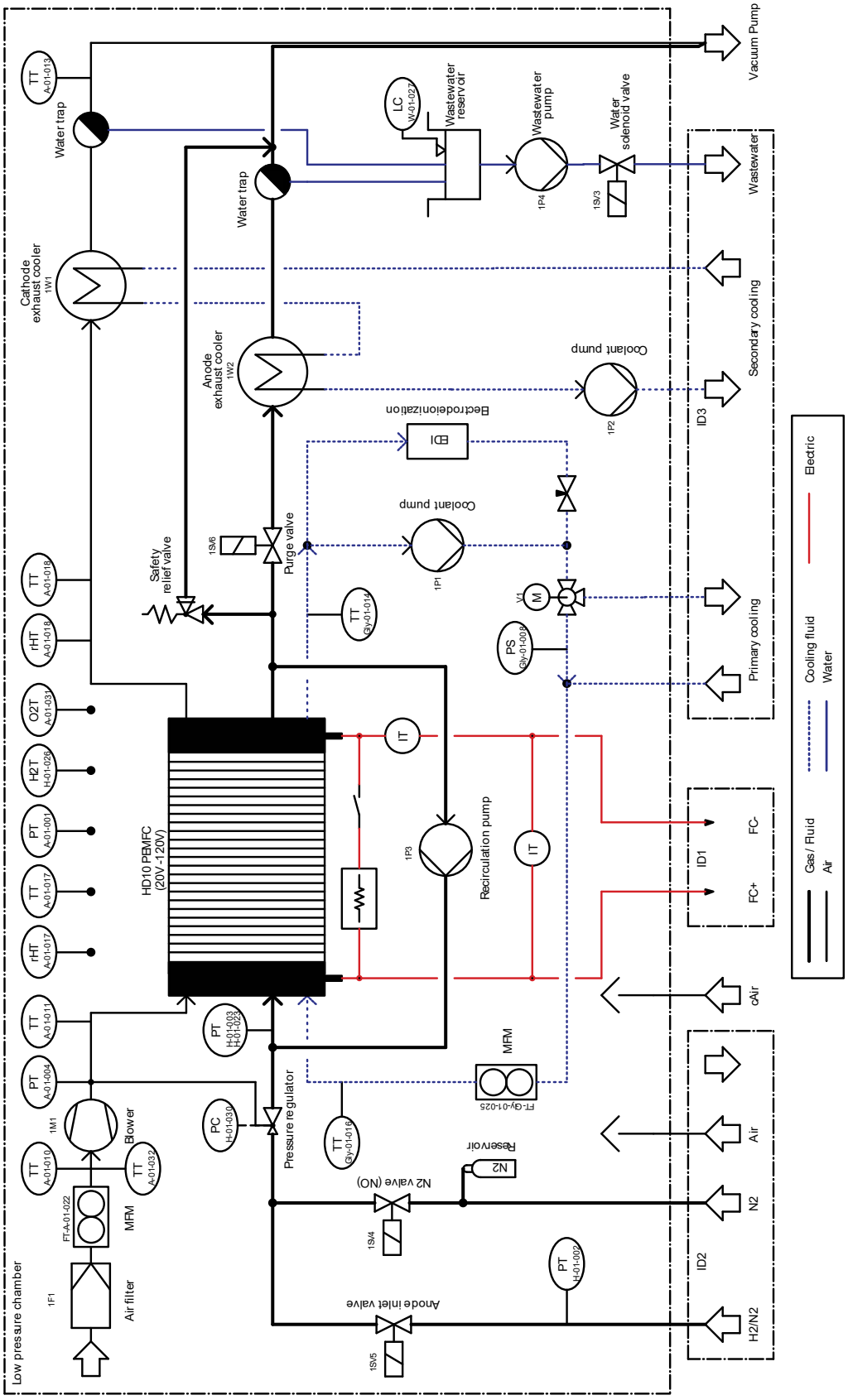

Figure A.1: P&ID of ATLAS.

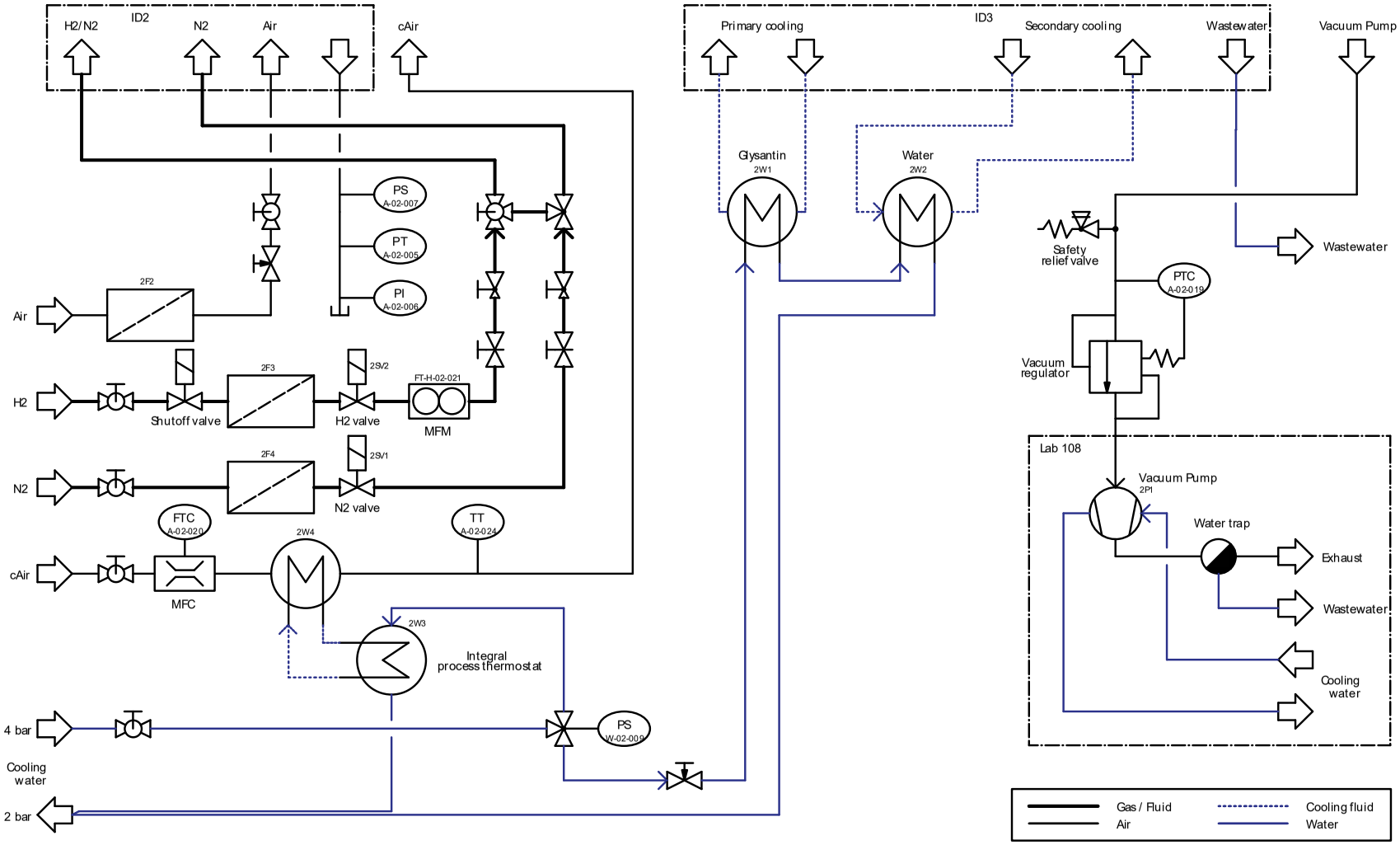

Figure A.2: P&ID of external components of ATLAS.

P&ID Code	Measured value [unit]	Type	Manufacturer	Measuring range	Measuring error
PT-H-01-001	Chamber pressure [hPa]	DRTR-ED-20MA-A2B	B+B Thermo-Technik GmbH	0 - 2 bar	± 0.4 % FS (full scale)
PT-H-01-002	Pressure H_2 supply [hPa]	DRTR-ED-20MA-A10B	B+B Thermo-Technik GmbH	0 - 10 bar	± 0.4 % FS
PT-H-01-003	Pressure anode [hPa]	DRTR-ED-20MA-A2B	B+B Thermo-Technik GmbH	0 - 2 bar	± 0.4 % FS
PT-A-01-004	Pressure cathode in [hPa]	DRTR-ED-20MA-A2B	B+B Thermo-Technik GmbH	0 - 2 bar	± 0.4 % FS
PT-A-02-005	Chamber pressure [hPa]	DRTR-ED-20MA-A5B	B+B Thermo-Technik GmbH	0 - 5 bar	± 0.4 % FS
TT-A-01-010	Temp. air blower in [°C]	Thermocouple Type K	ES Electronic Sensor GmbH	- 50…+200 °C	± 1.5 °C
TT-A-01-011	Temp. cathode in [°C]	Thermocouple Type K	ES Electronic Sensor GmbH	- 50…+200 °C	± 1.5 °C
TT-A-01-012	Resistor temp. [°C]	Thermocouple Type K	ES Electronic Sensor GmbH	- 50…+200 °C	± 1.5 °C
TT-A-01-013	Temp. intercooler out [°C]	Thermocouple Type K	ES Electronic Sensor GmbH	- 50…+200 °C	± 1.5 °C
TT-Gly-01-014	Coolant temp. stack out [°C]	PT1000 (DIN A)	Otom Group GmbH	-60…+180°C	± (0.15 + 0.002·MV) °C
TT-Gly-01-016	Coolant temp. stack In [°C]	PT1000 (DIN B)	Huba Control AG	-40…+125 °C	± 0.3 K
TT-A-01-017	Chamber temp. [°C]	KS-CAN-03	ZILA GmbH	-40…+80 °C	± 0.5 K (5…40 °C)
rHT-A-01-017	Relative humidity chamber [%]			0 - 100 % rH	± 2 % (10…90 % rH)
TT-A-01-018	Temp. cathode out [°C]	EE33-MFT J2022HV01/AB6-T12	E+E Eletronik Ges.m.b.H	-40…120 °C	± 0.2 °C
rHT-A-01-018	Relative humidity cathode out [%]			0 - 100 % rH	± (1.3 + 0.3 %·MV) %
PTC-A-02-019	Chamber pressure regulator [bar]	RPD200	Drumag GmbH	0 - 1 abs.	< 0.2 % FS
FTC-A-02-020	Chamber air flow [ln/min]	MFC D-6381-DR/003AI	Bronkhorst GmbH	100 - 5000 ln/min	± 1.0 % RD plus ± 0.5 % FS
FT-H-02-021	Hydrogen volume flow [ln/min]	EL-FLOW Select F-112AC	Bronkhorst GmbH	1.4 - 200 ln/min	± 0.5 % RD plus ± 0.1 % FS
FT-A-01-022	Cathode air flow in [l/min]	AFH10-02	ZCN	–	–
PT-H-01-023	Pressure anode internal [hPa]	AST4000	American Sensor Technologies	14.7 to 25 PSI	± 0.5 % FS
FT-Gly-01-025	Coolant flow [l/min]	Typ 210 DN20	Huba Control AG	5.0 - 85 l/min	< 1 % FS
H2T-H-01-026	H_2 content [ppm]	PowerKnowz_TM	Neodym Technologies Inc.	0 - 20000 ppm H_2	± 800 ppm
IT-01-028	Current air blower [A]	DK 20 C420 U	LEM International SA	5 - 20 A	± 1 % FS
IT-01-029	Current recirculation pump [A]	DK 20 C420 U	LEM International SA	5 - 20 A	± 1 % FS
O2T-A-01-031	O_2 content [Vol%]	MF010-O-LC	J. Dittrich Elektronic GmbH	0.1 - 25 Vol%	± 2 % FS
TT-A-01-032	Temp. air blower in [°C]	PT1000 (DIN B)	Otom Group GmbH	-60…+180°C	± (0.3 + 0.005·MV) °C

Table A.1: Sensor list.

Appendix B Parameter Constraints

Appendix B.1 Pressure - Current Constraints

Minimum current restriction is based on the minimum possible blower air flow and maximum current restriction is based on the threshold for the minimum average cell voltage of 0.5 V.

Pressure [hPa]	Minimum current[A]	Maximum current [A]
500	12	75
600	18	100
700	24	125
800	28	150
900	32	170
1000	40	180

Table B.1: Pressure – current constraints due to the minimum possible blower air flow and threshold for the minimum average cell voltage of 0.5 V.

Appendix B.2 Temperature – Stoichiometry Constraints

All temperature values shown with conditional formatting in Tables B.1 - B.3 have the unit °C.

		Cathode stoichiometry λ_c [–]				
		2	2.2	2.4	2.6	2.8
Pressure [hPa]	500	45.78	44.09	42.56	41.16	39.86
	600	49.39	47.66	46.09	44.65	43.32
	700	52.52	50.75	49.14	47.67	46.32
	800	55.28	53.48	51.84	50.35	48.96
	900	57.77	55.94	54.27	52.74	51.34
	1000	60.03	58.17	56.47	54.93	53.50

Table B.2: Lower temperature – stoichiometry constraints calculated with relative humidity at cathode outlet of 95 %.

		Cathode stoichiometry λ_c [–]				
		2	2.2	2.4	2.6	2.8
Pressure [hPa]	500	49.18	47.45	45.89	44.45	43.12
	600	52.88	51.11	49.50	48.02	46.66
	700	56.09	54.28	52.63	51.12	49.73
	800	58.92	57.08	55.40	53.86	52.44
	900	61.47	59.59	57.88	56.32	54.88
	1000	63.79	61.88	60.14	58.56	57.09

Table B.3: Lower temperature – stoichiometry constraints for maximum current densities calculated with relative humidity at cathode outlet of 80 %.

Pressure [hPa]	Cathode stoichiometry λ_c [–]				
	2	2.2	2.4	2.6	2.8
500	59.80	57.94	56.25	54.71	53.28
600	63.79	61.88	60.14	58.56	57.09
700	67.25	65.29	63.52	61.89	60.39
800	70.00	68.31	66.50	64.84	63.32
900	70.00	70.00	69.19	67.50	65.94
1000	70.00	70.00	70.00	69.91	68.33

Table B.4: Upper temperature – stoichiometry constraints calculated with relative humidity at cathode outlet of 48 %.

Appendix B.3 Constraints Arising in the Course of the Tests

Test block	Pressure [hPa]	Stack current [A]	Cathode stoichiometry [–]	Stack temperature [°C]
1	500	25	2.0	≤50
		50	2.0	≤48
		75	2.0	≤54
		65	2.0	≤50
2	600	75	2.2	≤52
			2.8	≤48
		100	2.0	≥60
3	800	100	2.8	≤52
		125	2.0	≤58
			2.4	≤54
		150	2.0	≥64
			2.2	≥64
			2.6	≤56
			2.8	≤56
4	900	100	2.8	≤54
		150	2.0	≤60
		165	2.2	≥68
5	700	125	2.8	≤52
			2.0	≥62
7	1000	165	2.4	≥60
			2.8	≥58

Table B.5: Constraints arising in the course of the tests.

Appendix C Experimental Plan

Pressure [hPa]	Stack current [A]	Cathode stoichiometry [–]	Stack temperature [°C]
500	25	2.0	50
			58
		2.2	46
		2.4	44
			56
		2.6	42
			48
		2.8	50
			52
	50	2.0	58
		2.4	48
		2.6	48
		2.8	52
	65	2.0	50
		2.6	42
	75	2.0	58
		2.2	48
			56
		2.4	46
			56
		2.6	48
		2.8	50
			52

Table C.1: Experimental plan - test block 1, performed on 20.02.2023 with a pressure of 500 hPa.

Pressure [hPa]	Stack current [A]	Cathode stoichiometry [–]	Stack temperature [°C]
600	25	2.0	50
		2.2	48
		2.4	60
		2.6	58
		2.8	44
	50	2.0	56
			62
		2.2	48
		2.4	48
			60
		2.6	58
		2.8	48
			56
	65	2.2	56
	75	2.2	52
		2.8	48
	100	2.0	54
			60
		2.4	60

		2.6	58
		2.8	48

Table C.2: Experimental plan - test block 2, performed on 28.02.2023 with a pressure of 600 hPa.

Pressure [hPa]	Stack current [A]	Cathode stoichiometry [–]	Stack temperature [°C]
800	50	2.0	56
			70
		2.4	52
			66
		2.8	50
	100	2.0	66
			70
		2.2	54
			68
		2.4	66
		2.8	54
			56
			58
	125	2.0	58
			60
		2.4	54
			56
	150	2.0	60
			64
		2.2	64
		2.4	66
		2.6	56
			64
		2.8	56
			58

Table C.3: Experimental plan - test block 3, performed on 02.03.2023 with a pressure of 800 hPa.

Pressure [hPa]	Stack current [A]	Cathode stoichiometry [–]	Stack temperature [°C]
900	50	2.0	58
			66
		2.2	56
			70
		2.4	58
			60
			64
		2.6	66
		2.8	60
	100	2.0	66
			70
		2.2	56
			70
		2.6	56
			66

		2.8	54
			56
	125	2.0	66
		2.6	66
	150	2.0	60
			62
		2.2	56
			60
	165	2.0	66
		2.2	68
		2.4	58
		2.6	66
		2.8	56
			60
			62

Table C.4: Experimental plan - test block 4, performed on 27.03.2023 with a pressure of 900 hPa.

Pressure [hPa]	Stack current [A]	Cathode stoichiometry [–]	Stack temperature [°C]
700	25	2.4	50
			58
			62
		2.6	48
			56
		2.8	54
			60
	50	2.0	58
			66
		2.2	56
		2.8	56
			60
	65	2.2	62
	75	2.2	60
			62
	100	2.6	48
			52
			56
	125	2.0	62
		2.8	52
			56
			60

Table C.5: Experimental plan - test block 5, performed on 28.03.2023 with a pressure of 700 hPa.

Pressure [hPa]	Stack current [A]	Cathode stoichiometry [–]	Stack temperature [°C]
1000	50	2.0	62
			70
		2.2	60
			64
		2.4	58

			64
			70
		2.6	60
			62
		2.8	54
			60
			68
	65	2.2	64
		2.8	62
			64
	75	2.0	62
			70
		2.2	60
			64
			70
		2.4	58
			70
		2.6	56
			66
		2.8	68
	100	2.6	56
		2.8	54
			58

Table C.6: Experimental plan - test block 6, performed on 29.03.2023 with a pressure of 1000 hPa.

Pressure [hPa]	Stack current [A]	Cathode stoichiometry [–]	Stack temperature [°C]
1000	125	2.8	58
	150	2.0	70
		2.2	66
			70
		2.4	70
		2.6	60
		2.8	60
			62
			68
	165	2.0	62
		2.4	60
			66
		2.6	66
		2.8	58
			64
			68
	175	2.0	64
			70
		2.2	62
			70
		2.4	62

			66
			70
		2.6	60
			64
		2.8	58
			60
			64
			68

Table C.7: Experimental plan - test block 7, performed on 30.03.2023 with a pressure of 1000 hPa.

Appendix D Regression Model Results

Appendix D.1 Results of the Full Regression Model

Dep. Variable:	y			R-squared:		0.995
Model:	OLS			Adj. R-squared:		0.994
Method:	Least Squares			F-statistic:		1123
No. Observations:	274			Prob (F-statistic):		2.00E-244
Df Residuals:	235			Log-Likelihood:		-1800.5
Df Model:	38			AIC:		3679
Covariance Type:	nonrobust			BIC:		3820
	coef	std err	t	P>|t|	[0.025	0.975]
Intercept	6613.581	42.967	153.922	0	6528.931	6698.23
p	527.7149	86.556	6.097	0	357.19	698.239
I	3042.047	86.052	35.351	0	2872.514	3211.579
T	482.7278	142.859	3.379	0.001	201.28	764.176
λ	153.8846	72.154	2.133	0.034	11.733	296.036
p:I	908.4651	182.129	4.988	0	549.652	1267.279
p:T	2838.603	358.646	7.915	0	2132.031	3545.175
p:λ	326.6818	89.584	3.647	0	150.192	503.172
I:T	132.0521	220.072	0.6	0.549	-301.513	565.618
I:λ	169.0835	60.711	2.785	0.006	49.475	288.692
T:λ	-769.692	217.725	-3.535	0	-1198.63	-340.75
np.power(p, 2)	-1254.11	177.671	-7.059	0	-1604.14	-904.075
np.power(I, 2)	-1068.34	205.564	-5.197	0	-1473.33	-663.357
np.power(T, 2)	-2568.24	481.142	-5.338	0	-3516.14	-1620.34
np.power(λ, 2)	-206.055	187.783	-1.097	0.274	-576.008	163.898
p:I:T	2551.716	347.81	7.337	0	1866.492	3236.94
p:I:λ	177.8592	94.04	1.891	0.06	-7.41	363.128
p:T:λ	-703.959	430.326	-1.636	0.103	-1551.75	143.831
I:T:λ	-402.916	184.42	-2.185	0.03	-766.243	-39.588
p:I:T:λ	13.6443	134.009	0.102	0.919	-250.367	277.656
p:np.power(I, 2)	429.4164	209.349	2.051	0.041	16.975	841.857
p:np.power(T, 2)	-1379.91	842.8	-1.637	0.103	-3040.32	280.504
p:np.power(λ, 2)	-68.8477	88.805	-0.775	0.439	-243.804	106.109
I:np.power(T, 2)	-2084.26	354.464	-5.88	0	-2782.6	-1385.93
I:np.power(λ, 2)	-130.785	63.078	-2.073	0.039	-255.057	-6.514
T:np.power(λ, 2)	277.6226	172.579	1.609	0.109	-62.377	617.622
np.power(p, 2):λ	160.3224	122.476	1.309	0.192	-80.968	401.613
np.power(p, 2):T	458.0936	426.65	1.074	0.284	-382.455	1298.642
np.power(p, 2):I	-1022.94	172.686	-5.924	0	-1363.15	-682.733
np.power(I, 2):T	-532.945	183.552	-2.904	0.004	-894.563	-171.328
np.power(T, 2):λ	682.9048	469.122	1.456	0.147	-241.316	1607.126
np.power(p, 3)	7.0305	113.894	0.062	0.951	-217.354	231.415
np.power(I, 3)	272.4548	144.872	1.881	0.061	-12.96	557.869
np.power(T, 3)	967.7957	616.03	1.571	0.118	-245.852	2181.444
np.power(λ, 3)	33.0466	76.837	0.43	0.668	-118.33	184.423
np.power(p, 4)	159.5953	143.651	1.111	0.268	-123.413	442.604
np.power(I, 4)	-180.476	132.56	-1.361	0.175	-441.633	80.682
np.power(T, 4)	-76.7209	183.432	-0.418	0.676	-438.102	284.66
np.power(λ, 4)	24.2031	180.465	0.134	0.893	-331.332	379.738
Omnibus:	94.346			Durbin-Watson:		1.699
Prob(Omnibus):	0			Jarque-Bera (JB):		520.139
Skew:	-1.277			Prob(JB):		1.13E-113
Kurtosis:	9.248			Cond. No.		215

Table D.1: Python results of the full regression model.

Appendix D.2 Results of the Reduced Regression Model

Dep. Variable:	y		R-squared:		0.994
Model:	OLS		Adj. R-squared:		0.994
Method:	Least Squares		F-statistic:		1499
No. Observations:	274		Prob (F-statistic):		1.60E-257
Df Residuals:	244		Log-Likelihood:		-1803
Df Model:	29		AIC:		3666
Covariance Type:	nonrobust		BIC:		3774

	coef	std err	t	P>|t|	[0.025	0.975]
Intercept	6610.049	35.099	188.325	0	6540.913	6679.185
p	512.2256	61.709	8.301	0	390.675	633.776
I	3056.556	79.517	38.439	0	2899.928	3213.184
T	495.0897	118.296	4.185	0	262.078	728.101
λ	164.9506	41.212	4.003	0	83.775	246.126
p:I	937.5027	167.859	5.585	0	606.865	1268.141
p:T	2802.079	286.134	9.793	0	2238.472	3365.687
p:λ	297.4785	71.998	4.132	0	155.662	439.295
I:λ	144.1737	50.106	2.877	0.004	45.478	242.869
T:λ	-661.701	160.66	-4.119	0	-978.158	-345.243
np.power(p, 2)	-1091.29	96.731	-11.282	0	-1281.83	-900.757
np.power(I, 2)	-1229.54	124.734	-9.857	0	-1475.23	-983.845
np.power(T, 2)	-2493.24	294.771	-8.458	0	-3073.86	-1912.62
np.power(λ, 2)	-156.75	45.42	-3.451	0.001	-246.216	-67.285
p:I:T	2516.839	327.442	7.686	0	1871.866	3161.813
p:I:λ	162.0014	88.457	1.831	0.068	-12.235	336.238
p:T:λ	-544.481	262.519	-2.074	0.039	-1061.57	-27.388
I:T:λ	-327.749	143.215	-2.289	0.023	-609.845	-45.653
p:np.power(I, 2)	482.7843	193.498	2.495	0.013	101.644	863.924
p:np.power(T, 2)	-1218.43	588.955	-2.069	0.04	-2378.52	-58.345
I:np.power(T, 2)	-1931.8	233.262	-8.282	0	-2391.26	-1472.33
I:np.power(λ, 2)	-136.048	58.901	-2.31	0.022	-252.067	-20.028
T:np.power(λ, 2)	167.2484	96.784	1.728	0.085	-23.39	357.886
np.power(p, 2):λ	127.0856	78.682	1.615	0.108	-27.897	282.068
np.power(p, 2):T	389.5453	271.28	1.436	0.152	-144.803	923.894
np.power(p, 2):I	-1058.46	148.108	-7.147	0	-1350.19	-766.724
np.power(I, 2):T	-584.091	145.47	-4.015	0	-870.628	-297.553
np.power(T, 2):λ	482.0388	325.153	1.482	0.139	-158.426	1122.503
np.power(I, 3)	278.4372	138.472	2.011	0.045	5.685	551.189
np.power(T, 3)	778.8551	466.421	1.67	0.096	-139.87	1697.58

Omnibus:	94.442		Durbin-Watson:	1.67
Prob(Omnibus):	0		Jarque-Bera (JB):	505.514
Skew:	-1.289		Prob(JB):	1.69E-110
Kurtosis:	9.135		Cond. No.	128

Table D.2: Python results of the regression model after sequential backwards selection.

Eidesstattliche Erklärung und Urheberrecht bei studentischen Arbeiten

Hiermit räume ich, Settele, Jonas, Adlerstraße 56, 70199 Stuttgart, der Universität Stuttgart, Institut für Flugzeugbau, ein kostenloses, zeitlich und räumlich unbeschränktes, einfaches Nutzungsrecht an der von mir erstellten Masterarbeit mit dem Titel:

EXPERIMENTAL INVESTIGATION OF A PEMFC SYSTEM OPERATED UNDER LOW PRESSURE CONDITIONS

und den im Rahmen dieser Arbeit entstandenen Arbeitsergebnissen ein. Ich erkläre, die Arbeit selbständig verfasst und bei der Erstellung dieser Arbeit die einschlägigen Bestimmungen, insbesondere zum Urheberrechtsschutz fremder Beiträge, eingehalten zu haben. Soweit meine Arbeit fremde Beiträge (z.B. Bilder, Zeichnungen, Textpassagen) enthält, erkläre ich, dass diese Beiträge als solche gekennzeichnet sind (z.B. Zitat, Quellenangabe) und ich eventuell erforderlich gewordene Zustimmungen der Urheber zur Nutzung dieser Beiträge in meiner Arbeit eingeholt habe. Für den Fall der Verletzung Rechter Dritter durch meine Arbeit, erkläre ich mich bereit, der Universität Stuttgart einen daraus entstehenden Schaden zu ersetzen bzw. die Universität Stuttgart auf deren Aufforderung von eventuellen Ansprüchen Dritter freizustellen.

Das der Universität Stuttgart hiermit eingeräumte Nutzungsrecht erstreckt sich auf sämtliche bekannte Nutzungsarten und umfasst neben dem Recht auf Nutzung der Arbeitsergebnisse in Forschung, Lehre und Studium, insbesondere das Recht der Vervielfältigung und Verbreitung, das Recht zur Bearbeitung und Änderung inklusive Nutzung, Vervielfältigung und Verbreitung der dabei entstehenden Ergebnisse, sowie insbesondere das Recht der öffentlichen Zugänglichmachung im Internet sowie das Recht der Weiterübertragung auf einen Dritten ohne meine erneute Zustimmung.

Mir ist bekannt, dass die Einräumung des Nutzungsrechts der öffentlichen Zugänglichmachung auch beinhaltet, dass mein Name im Zusammenhang mit dem Titel der oben genannten Arbeit auf den Webseiten der Universität Stuttgart genannt werden kann. Mir ist auch bekannt, dass – sofern meine Arbeit selbst nicht im Internet zugänglich gemacht wird – die Einräumung des Nutzungsrechts der öffentlichen Zugänglichmachung auch umfasst, dass die Universität Stuttgart auf ihren Webseiten meinen Namen im Zusammenhang mit dem Titel der oben genannten Arbeit (z.B. in Listen über am Institut abgeschlossene studentische Arbeiten) nennen kann.

Außerdem übertrage ich der Universität Stuttgart das Eigentum an einem von mir der Bibliothek des Instituts für Flugzeugbau kostenlos zur Verfügung gestellten Exemplars meiner oben genannten Arbeit und räume der Universität Stuttgart auch für dieses Exemplar die oben genannten Nutzungsrechte ein.

Stuttgart, 31.05.23, J. Settele

Ort, Datum, Unterschrift